

Stefan Prorok

# Hybrid Silicon-Organic Resonators for Optical Modulation and Filtering



Cuvillier Verlag Göttingen  
Internationaler wissenschaftlicher Fachverlag



## Hybrid Silicon-Organic Resonators for Optical Modulation and Filtering





# Hybrid Silicon-Organic Resonators for Optical Modulation and Filtering

Vom Promotionsausschuss der  
Technischen Universität Hamburg-Harburg  
zur Erlangung des akademischen Grades  
Doktor-Ingenieur (Dr.-Ing.)  
genehmigte Dissertation

von

Dipl.-Ing. Stefan Prorok

aus

Hamburg, Deutschland

2015



## **Bibliografische Information der Deutschen Nationalbibliothek**

Die Deutsche Nationalbibliothek verzeichnet diese Publikation in der Deutschen Nationalbibliografie; detaillierte bibliografische Daten sind im Internet über <http://dnb.d-nb.de> abrufbar.

1. Aufl. - Göttingen: Cuvillier, 2015

Zugl.: (TU) Hamburg-Harburg Univ., Diss., 2015

### **Gutachter:**

Prof. Dr. Manfred Eich (TU Hamburg-Harburg)

Prof. Dr. Ernst Brinkmeyer (TU Hamburg-Harburg)

Prof. Dr.-Ing. Hoc Khiem Trieu (TU Hamburg-Harburg)

Tag der mündlichen Prüfung: 23.02.2015

© CUVILLIER VERLAG, Göttingen 2015

Nonnenstieg 8, 37075 Göttingen

Telefon: 0551-54724-0

Telefax: 0551-54724-21

[www.cuvillier.de](http://www.cuvillier.de)

Alle Rechte vorbehalten. Ohne ausdrückliche Genehmigung des Verlages ist es nicht gestattet, das Buch oder Teile daraus auf fotomechanischem Weg (Fotokopie, Mikrokopie) zu vervielfältigen.

1. Auflage, 2015

Gedruckt auf umweltfreundlichem, säurefreiem Papier aus nachhaltiger Forstwirtschaft

ISBN 978-3-95404-952-3

eISBN 978-3-7369-4952-2



# Contents

<b>1</b>	<b>Introduction</b>	<b>1</b>
<b>2</b>	<b>Basic Concepts and Numerical Methods</b>	<b>4</b>
2.1	State of the Art in Silicon Electro-Optic Modulators . . . . .	4
2.2	Second Order Nonlinear Effects in Organic Materials . . . . .	7
2.2.1	Microscopic Origin of the Electro-Optic Effect . . . . .	7
2.2.2	Macroscopic Electro-Optic Effect . . . . .	13
2.2.3	Polymer Material Properties . . . . .	16
2.3	Photonic Crystals . . . . .	18
2.3.1	Photonic Crystal Slabs . . . . .	20
2.3.2	Lattice Defects in Photonic Crystal Slabs . . . . .	20
2.4	Numerical Methods . . . . .	22
2.4.1	Finite Integration Method . . . . .	22
2.4.2	Finite Difference Method for Curved Coordinate Systems . .	25
<b>3</b>	<b>Trimming of Silicon Ring Resonators</b>	<b>27</b>
3.1	Polymer Bleaching by Ultra Violet Light . . . . .	29
3.2	Trimming of Silicon Ring Resonators by Electron Beam Bleaching .	30
<b>4</b>	<b>Configurable Photonic Crystal Waveguides</b>	<b>36</b>
4.1	Tuning of Photonic Crystal Waveguides . . . . .	38
4.2	Cavity Definition in Photonic Crystal Waveguides . . . . .	40
4.3	Trimming of Photonic Crystal Cavities . . . . .	42



---

<b>5</b>	<b>Photonic Crystal Resonators with High Quality Factors</b>	<b>45</b>
5.1	Quality Factors in Single Defect Heterostructures . . . . .	46
5.2	Multistep Heterostructures with Gaussian Field Envelopes . . . . .	55
5.3	Photonic Crystal Cavities with Raised Cosine Field Envelopes . . .	60
5.3.1	Synthesis of Raised Cosine Functions . . . . .	63
5.3.2	Numerical Validation . . . . .	68
<b>6</b>	<b>Electro-Optic Modulation in Hybrid Silicon-Organic Waveguide Structures</b>	<b>73</b>
6.1	Electro-Optic Phase Modulation in Slotted Waveguides . . . . .	74
6.2	Electro-Optic Amplitude Modulation in Photonic Crystal Cavities .	79
6.3	Electro-Optic Modulation at GHz Frequencies . . . . .	82
<b>7</b>	<b>Electrical and Nonlinear Characterization of Polymer Thin Films on Silicon Substrate</b>	<b>88</b>
7.1	Electro-Optic Characterization of Thin Films on Silicon Substrate .	90
7.2	High Field Poling of Thin Polymer Films of APC-CKL1 . . . . .	99
7.2.1	Conduction Mechanisms in Thin Films of APC-CKL1 . . . . .	99
7.2.2	Interrelation between Electronic Substrate Properties and the Electro-Optic Coefficient . . . . .	103
<b>8</b>	<b>Conclusion and Outlook</b>	<b>110</b>
8.1	Conclusion . . . . .	110
8.2	Outlook . . . . .	114
<b>A</b>	<b>Beam Characterization by the Knife Edge Method</b>	<b>117</b>



# Chapter 1

## Introduction

Nowadays we live in a world where high speed network connection has become both vital and self-evident for us. Most urban areas in the industrialized world offer a dense coverage of Wifi or high-speed mobile service and the majority of households are equipped with broad band internet access. At the same time reliable internet access has become a strategic asset. Companies need it to communicate with customers and suppliers, states utilize it to gather intelligence data and private persons use it to maintain professional and personal networks.

All of this would not have been possible without major breakthroughs in optical communication. Compared to copper based communication optical systems feature larger available bandwidth, negligible cross talk between adjacent fibers and low propagation losses. Due to the expensive equipment optical communication systems were originally only used for long haul communication.

In the last couple of years the trend of *big data* has led to an economic pressure to develop optical communication systems for a rack to rack and chip to chip applications. The reason for this lies in the ongoing concentration of computing power in data centers. In modern data centers 25-35% of the electrical energy is consumed by interconnects between different racks and chips, not for computation [1, 2]. All major suppliers of server hardware (>80% market share [3]) are engaged in research activity in the area of optical transceivers revealing the importance of this problem [4, 5, 6, 7].

Even though optical transceivers, which are integrated on silicon chips, are already commercially available dense integration of optical components on the chip level remains challenging. This holds in particular for the electro-optic modulator that should fulfill the following four requirements:

- Large electrical modulation bandwidth
- Low electrical modulation amplitude
- Tolerance with respect to fabrication imperfections
- Small geometric footprint

In this thesis it will be shown how hybrid silicon-organic electro-optic modulators can be used to meet these requirements. Technological and scientific challenges of this material system will be discussed.

### **Outline of this Thesis**

This thesis focuses on the advancement of polymer infiltrated silicon photonic structures as integrated electro-optic modulators and filters. An emphasis is placed on modulators based on photonic crystal resonators, which have the potential to achieve highest integration densities and low power consumption at the same time. The thesis is structured as follows:

Chapter 2 introduces the physical background of this thesis. Basic concepts of nonlinear organic materials, photonic crystals and the numerical methods employed in this thesis are being presented.

Chapter 3 addresses the trimming of silicon ring resonators. This topic is of high technological relevance since so far random process fluctuations have strongly limited the commercial applicability of silicon ring resonators. It is shown that bleaching of a dye doped polymer cladding can be used to compensate these random process fluctuations and thereby allow a higher integration of ring resonators.

Chapter 4 describes how the bleaching approach can be extended to photonic crystal waveguides. It will be shown that by spatially resolved bleaching photonic

crystal waveguides can be modified in a flexible way. Using this method it is possible to define band edge filters and cavities with high quality factors.

Chapter 5 provides a detailed analysis of different aspects that determine the quality factor in photonic crystal heterostructures. Different approaches are presented, which significantly improve the quality factor in such structures.

Chapter 6 is focused on the experimental realization of integrated silicon electro-optical modulators. Electro-optic phase modulation in slotted waveguides and amplitude modulation in a photonic crystal cavity are demonstrated for low frequencies. Electro-optic modulation with GHz frequency is shown in a photonic crystal waveguide.

In chapter 7 the high field poling process with silicon electrodes is analyzed in order to identify possible reasons for the low electro-optic coefficients in slotted waveguides. The electrical conduction mechanisms in polymer thin films on silicon substrate have been studied and a theoretic model for the current conduction is presented. The results are complemented by electro-optic measurements utilizing a modified Teng-Man method. It is shown that the low poling efficiency on silicon substrates is to a large extent due to the electronic properties of the silicon surface. These properties can be influenced by interface modifications. It is shown that the modification of the silicon interface by a 5 nm thick layer of  $\text{Al}_2\text{O}_3$  leads to a significant improvement of the electro-optic coefficients.

Chapter 8 summarizes the results of this work and gives an outlook on future research.



# Chapter 2

## Basic Concepts and Numerical Methods

This chapter provides an overview on the state of the art in the field of silicon based electro-optical modulators. Furthermore basic theoretical concepts of nonlinear electro-optic polymers and photonic crystals are introduced. The numerical methods that were used in this work are discussed briefly.

### 2.1 State of the Art in Silicon Electro-Optic Modulators

Several different physical effects can be utilized in order to create silicon based electro-optic modulators. Silicon has a reported thermo-optic coefficient of  $1.85 \cdot 10^{-4}/\text{K}$  at room temperature [8]. Hence, moderate temperature changes yield a refractive index change in the order of  $10^{-3}$ , which is sufficient for modulation. However, thermo-optic devices show switching speeds in the order of 10 to 100  $\mu\text{s}$ , which is not suitable for fast electro-optic modulation [9]. Another effect to be mentioned is the Franz Keldysh effect, which describes a change in the absorption spectrum of the material upon applied electric field. In undoped silicon the changes in absorption and refractive index due to the Franz Keldysh effect are below  $0.1/\text{cm}$

and  $10^{-5}$  respectively [10], which is too small for efficient electro-optic modulation.

The most common way to achieve electro-optic modulation in silicon is by means of the plasma dispersion effect of free charge carriers. In semiconductors as silicon the refractive index and absorption can be changed by altering the amount of free charge carriers in the material. Free charge carriers lead to enhanced linear material losses due to free carrier absorption. At the same time free charge carriers reduce the refractive index of silicon [10]. Early works on electro-optic modulators using free carrier absorption have been performed by Treyz et al. in 1991 [11]. The electrical bandwidth of this modulator was limited to 20 MHz.

The first electro-optic modulators using the refractive index change due to the plasma dispersion effect have been realized by Lorenzo et al. in 1987 [12, 13]. However, for a long time the speed of silicon modulators has been limited to electric bandwidths below 1 GHz. In 2004 Liu et al. realized the first GHz electro-optic modulation in a silicon waveguide [14]. The works of Lorenzo and Liu relied on the injection of charge carriers into a weakly doped core region.

Using charge injection in order to change the refractive index of a silicon structure imposes limitations on the modulation frequency. While the depletion of charge carriers is a field assisted process and can be as fast as 7 ps the injection is a diffusion process, which has time constants in the order of nanoseconds [15, 16]. In 2007 the first modulator was realized that relied only on the depletion effect [17]. This modulator featured a modulation band width of 30 GHz. Since then a lot of effort has been done in order to further optimize the modulation band width. Several modulators with modulation speeds up to 50 GHz have been shown in the last couple of years [18, 19, 20].

Despite the progress in the field of silicon modulators a fundamental challenge remains. For modulators with large modulation bandwidth high doping concentrations are required, which increase the insertion loss of the modulators. One way to remedy this problem is to combine silicon waveguides with a second material. In 2005 Baer-Jones et al. introduced the concept of a slotted silicon waveguide that is infiltrated by a nonlinear electro-optic polymer [21]. In their concept the light is confined by two silicon rails, which are separated by a slot of 200 nm or less. A

significant part of the optical power, however, is guided in the low refractive index polymer.

In contrast to silicon nonlinear polymers can exhibit a very large Pockels effect. Due to recent advances in molecular engineering Pockels coefficients of more than 300 pm/V have been achieved [22]. This value is 10 times higher than that of lithium niobate, which is still the standard material for inorganic electro-optic applications [23]. Furthermore, polymers are compatible to standard complementary metal-oxide-semiconductor (CMOS) technology and can be readily integrated into existing fabrication processes for electronic circuits [24]. Witzenz et al. have shown theoretically that EO polymers in slotted waveguides can have a significantly smaller device footprint as compared to modulators using plasma dispersion as modulation effect [25]

So far the most compact electro-optic modulator based on silicon slotted waveguides and electro-optic polymer reached a value of  $V_{\pi}l$  as low as 5 Vmm but the reported device has only a modulation bandwidth of 1 kHz [26]. Slotted waveguide modulators with 3 GHz modulation bandwidth and a  $V_{\pi}l$  of 8 Vmm have been realized by Ding et al. [27]. For comparison, the most compact silicon modulator based on the plasma dispersion effect has a  $V_{\pi}l$  of 0.36 Vmm, which is about 14 times smaller than the best slotted waveguide based modulator [28]. The main reason for the comparatively large value of  $V_{\pi}l$  in slotted waveguides is the small in device electro-optic coefficient of the polymer. This aspect will be covered in detail in the chapters 6 and 7.

In order to further reduce the modulator footprint the interaction between the optical wave and the change in refractive index must be enhanced. One way of achieving this is to let the light propagate through a material or waveguide with slow group velocity. Monat et al. have reported on the enhancement of free carrier absorption and Kerr nonlinearities in silicon slow light waveguides [29]. Lin et al. have used slotted slow light waveguides in order to enhance the electro-optic effect [30]. They have reported on an increase of the electro-optic modulation signal by 23 dB. The resulting modulator exhibited a  $V_{\pi}l$  of 0.56 Vmm. On the other hand, the slow light effect limits the available modulation band width [31]. Li et al.



have systematically studied the bandwidth limitations for silicon photonic crystal waveguides [32]. They found that by engineering the properties of the photonic crystal lattice waveguides with low dispersion and group velocities as low as  $\frac{c}{49}$  can be created, which have optical bandwidths of 9.5 nm.

Another way of increasing the refractive index sensitivity of a modulator is to use resonant structures. Ring resonators with embedded pn-junctions as well as hybrid polymer silicon ring resonators have been used as electro-optic modulators [33, 34]. While the modulation amplitude obtained for resonant structures are comparable to those found in integrated interferometers the device footprint of a resonant modulator can be as small as  $12 \mu m$  [33]. In resonators the required modulation voltage is inversely proportional to the quality factor  $Q$  of the cavity, therefore in principle the required modulation voltage can be arbitrarily low [35]. This property makes optical resonators interesting for densely integrated electro-optic modulators.

## 2.2 Second Order Nonlinear Effects in Organic Materials

In order to understand the physical principles behind the electro-optic effect in nonlinear polymers it is most intuitive to first look at the properties of these materials at the molecular level. The knowledge obtained from the molecular analysis can then be transferred to the macroscopic level where it is possible to operate with effective material parameters.

### 2.2.1 Microscopic Origin of the Electro-Optic Effect

Most state of the art nonlinear polymers are either guest-host systems or copolymers in which chromophore molecules are embedded in an inactive polymer matrix [36, 37, 38]. The chromophore molecules exhibit a donor and an acceptor part. These two parts of the molecule are connected by a conjugated chain of carbon bonds that allows charge carriers to move along the molecule. Due to the

high mobility of charge carriers along the conjugated chain chromophore molecules are highly polarizable. The molecular polarization  $p$  induced by an external electric field  $E_n$  can be written as

$$p = \alpha_{ij}E_i + \beta_{ijk}E_iE_j + \gamma_{ijkl}E_iE_jE_k \dots \quad (2.1)$$

where  $\alpha_{ij}$  describes the linear polarizability of the molecule. The terms  $\beta_{ijk}$  and  $\gamma_{ijkl}$  are tensors, which describe the first and second order hyperpolarizabilities of the molecule that give rise to first and second order non-linear effects. In this thesis the discussion will be limited to the first order hyperpolarizability. Higher order nonlinear effects are not considered.

In order to create materials with a strong first order nonlinearity the chromophore molecules should exhibit a large hyperpolarizability  $\beta$ . Oudar and Chemla have proposed a model that relates  $\beta$  to the charge transfer inside the chromophore molecule with

$$\beta(-\omega_3; \omega_1, \omega_2) = 2 \frac{e^2(\mu_e + \mu_g)\mu_{ge}^2}{\Delta E^2} \cdot \frac{\omega_{ge}^4(3\omega_{ge}^2 + \omega_1\omega_2 - \omega_3^2)}{(\omega_{ge}^2 - \omega_1^2)(\omega_{ge}^2 - \omega_3^2)(\omega_{ge}^2 - \omega_2^2)}. \quad (2.2)$$

$\mu_g$  and  $\mu_e$  denote the dipole moments of the ground state and the excited state.  $\mu_{ge}$  and  $\Delta E$  describe the transition dipole moment and the energy difference between ground state and excited state.  $\omega_{ge}$  is the resonance of the dipole transition [39, 40].  $\omega_1$  and  $\omega_2$  are the frequencies of the external electric fields  $E_n$  and  $\omega_3$  is the frequency of the resulting nonlinear polarization  $p$ .

Equation 2.2 contains two fractions. The first fraction only depends on the dipole moments and the energy difference between ground state and excited state. This part of the hyperpolarizability is frequency independent. The second fraction only depends on the resonance frequency of the dipole transition. This part of the hyperpolarizability is frequency dependent and models the dispersion of the hyperpolarizability. As a certain frequency separation between the dipole resonance and the optical fields is necessary in order to avoid linear losses increasing the frequency independent part of the hyperpolarizability is the cardinal goal in the synthesis of novel nonlinear materials.

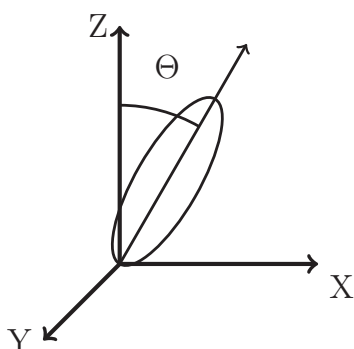


**Figure 2.1:** shows the schematic of a chromophore molecule inside the laboratory coordinate system  $XYZ$ . The molecule is depicted by an ellipsoid and the axis of the conjugated  $\pi$  system is denoted by an arrow.

More recent studies have shown that the bond length alteration (BLA) between single and double carbon bonds is correlated with the hyperpolarizability of chromophore molecules [41]. Quantum mechanical calculations have revealed that many common chromophore molecules had BLAs, which were too large. The BLA is mainly determined by the ground state polarization induced by the donor and acceptor part of the chromophore molecule but also the host material can influence the BLA [42]. The optimization of structure parameters such as the BLA have lead to a significant improvement of the attained hyperpolarizabilities [43]. However, Kuzyk has pointed out that the structure parameter guided approach is a heuristic one and does not necessarily lead to optimal results. Molecules with close to optimal nonlinearities therefore require full quantum mechanical calculations [44].

In general, chromophore molecules can have different dipole transitions in different directions of the molecule. However, since many chromophore molecules for nonlinear applications exhibit a rod-like structure, it is often valid to assume only one dominant dipole moment that is aligned with the conjugated  $\pi$ -system of the chromophore. Under this assumption the hyperpolarizability tensor also has only one dominant component  $\beta_{zzz}$ , which is aligned with the axis of the conjugated  $\pi$ -system. Figure 2.1 shows how the chromophore orientation is defined in the laboratory coordinate system  $XYZ$ .

Provided that then hyperpolarizability can be described sufficiently well by the dominant component  $\beta_{zzz}$  the macroscopic second order susceptibility tensor of the material  $\chi^{(2)}$  contains two independent components, which are given by

$$\chi_{ZZZ}^{(2)} = N f_L(\omega_1) f_L(\omega_2) f_L(\omega_3) \beta_{zzz} \int_V \cos^3(\Theta) f(\Theta) d\Theta \quad (2.3)$$

and

$$\chi_{ZXX}^{(2)} = \frac{1}{2} N f_L(\omega_1) f_L(\omega_2) f_L(\omega_3) \beta_{zzz} \int_V \sin^2(\Theta) \cos(\Theta) f(\Theta) d\Theta \quad (2.4)$$

$f(\Theta)$  is the distribution function of the chromophore molecules.  $N$  and  $f_L$  are the number density and the local field factors for the fields external electric fields  $E_i(\omega_1)$  and  $E_j(\omega_2)$  and the nonlinear polarization  $p$  [45]. For quasi static electric fields the local field factor is given by the Onsager expression

$$f_L(\omega) = \frac{\epsilon(n^2 + 2)}{(n^2 + 2\epsilon)} \quad (2.5)$$

where  $\epsilon$  is the dielectric constant and  $n$  is the refractive index. For optical frequencies the local field factor is better described by the Lorentz field factor

$$f_L(\omega) = \frac{n^2(\omega) + 2}{3} [46]. \quad (2.6)$$

If the chromophore molecules are isotropically oriented the second order susceptibility becomes zero. Thus the material exhibits no first order nonlinearity at the macroscopic scale. In order to obtain a macroscopic first order nonlinearity it is necessary to break the centrosymmetry of the system by aligning the chromophore molecules.

The most common way to achieve an alignment of the chromophore molecules along one direction is to introduce a poling step. Different types of poling are known such as contact poling via electrodes, corona poling where the field is applied by a plasma and laser induced poling [47, 48, 49]. However, all of these methods involve heating the polymer up to the glass transition temperature and applying a strong electric field  $E_p$ . At the glass transition temperature the chromophore molecules become mobile. The torque of the applied electric field acts on the chromophores ground state dipole moment and induces a uniaxial alignment of the

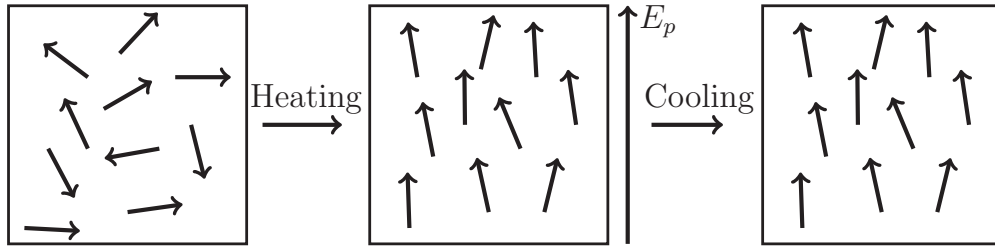


**Figure 2.2:** shows a schematic of the poling process. Chromophore molecules are depicted by small arrows and  $E_p$  indicates the poling field.

molecules along the poling field. Upon cooling down the chromophore molecules become immobile again and maintain their oriented state. A schematic of a poling step is shown in figure 2.2.

Chromophore doped polymer films, which have been poled by electric fields can be well described by means of the oriented gas model [50]. This model assumes dipoles that are oriented in an external electric field. At the same time the dipoles are subject to thermal fluctuations given by the Boltzmann statistic. Dipole-dipole interactions are neglected in this model. With these assumptions the integrals in equation 2.3 and 2.4 can be approximated by Langevin functions  $L$  of order  $n$

$$\int_V \cos^n(\Theta) f(\Theta) d\Theta = L_n\left(\frac{\mu f_L(0) E_p}{kT}\right) \quad (2.7)$$

where  $f_L(0)$  is the local field factor at zero frequency.  $k$  and  $T$  are Boltzmann's constant and the absolute temperature respectively. If the argument of the Langevin function is smaller than one, the  $L_n$  can be well approximated by a first order Taylor series expansion with

$$\int_V \cos(\Theta) f(\Theta) d\Theta = \frac{\mu_g f_L(0) E_p}{3kT} \quad \int_V \cos^3(\Theta) f(\Theta) d\Theta = \frac{\mu_g f_L(0) E_p}{5kT}. \quad (2.8)$$

In this case equations 2.3 and 2.4 can be rewritten as

$$\chi_{ZZZ}^{(2)} = N f(\omega_1) f(\omega_2) f_L(\omega_3) \beta_{zzz} \frac{\mu_g f_L(0) E_p}{5kT} \quad (2.9)$$

and

$$\chi_{ZXX}^{(2)} = N f_L(\omega_1) f_L(\omega_2) f_L(\omega_3) \beta_{zzz} \frac{\mu_g f_L(0) E_p}{15kT}. \quad (2.10)$$

The ratio of  $\chi_{ZZZ}^{(2)}$  and  $\chi_{ZXX}^{(2)}$  for the weakly oriented case is approximately three. However, for well oriented films the ratio can be significantly larger [51]. Equations 2.9 and 2.10 show that besides the hyperpolarizability  $\beta_{zzz}$  the ground state dipole moment  $\mu_g$  is equally important in order to achieve a large macroscopic nonlinearity. Therefore in electro-optics the product  $\beta_{zzz}\mu_g$  is often used as a figure of merit for chromophore molecules. Even though large molecular dipole moments help to orient the molecules in the poling field they also lead to increased interaction between the chromophore molecules and a reduction of the poling efficiency. For chromophore molecules with large dipole moment additional chemical groups are required to shield the dipoles from neighboring molecules and thus allow for larger number densities without detrimental dipole-dipole interactions [52].

One disadvantage of high field poling is the fact that the oriented state is thermodynamically unstable. The decay of the oriented state after poling can be described by Williams-Watt-Kohlrausch stretched exponential functions [53]. Depending on the polymer-chromophore system the relaxation time of the poled state can be modeled by a Williams-Landel-Ferry or Arrhenius behavior [54, 55]. The relaxation time is exponentially dependent on the difference between the operating temperature and the glass transition temperature. Therefore it must be made sure that the operating temperature stays significantly below the glass transition temperature of the polymer.

Suzuki et al. reported relaxation times of about one year for poled films of polymethylmethacrylate (PMMA) doped with 5% DR1 chromophore at room temperature 70 °C below the glass transition temperature [55]. For lifetimes of 10 years the extrapolated operating temperature should not exceed -20 °C or 110°C below the glass transition temperature. Commercial products are usually specified for an operating temperature up to 70 °C [56]. Based on the reported values for chromophore doped PMMA this would mean that transition temperatures of electro-optic polymers should be above 180 °C. Only a few polymers can fulfill this requirement. Furthermore the chromophore molecules must exhibit sufficient thermal stability in order to survive the poling process.

One possible solution to this problem is using cross linking to enhance the thermal stability of the polymer. Kim et al. have realized electro-optic modulators that show no significant change in electro-optic performance after several days at a temperature of 95 °C [57]. However, it has been observed that cross linking leads to a reduction of the electro-optic coefficient due to the reduced mobility of the chromophore molecules in the cross linked matrix during high field poling [58]. Therefore a trade off exists between the thermal stability of the oriented state and the electro-optic effect. Luo et al. reported that this trade off can be circumvented by separating the hardening of the matrix from the poling step [59]. They have performed the poling while the polymer is still in thermoplastic state and the cross linking after the poling using a Diels-Alder cycloaddition. Using this approach they were able to show high electro-optic coefficients, which retained 80 % of the original value after 250 hours of baking at 70 °C.

### 2.2.2 Macroscopic Electro-Optic Effect

Macroscopically nonlinear materials and their interaction with electro-magnetic waves can be understood by extending the common definitions for dielectric materials. In a linear isotropic dielectric the electric flux density  $D$  can be written as

$$D = \epsilon_0 E + P = \epsilon_0(1 + \chi^{(1)})E \quad (2.11)$$

where  $P$  is the polarization density and  $\chi$  is the electric susceptibility of the material. The electric susceptibility is related to the relative permittivity  $\epsilon_r$  of the material by  $\chi^{(1)} = \epsilon_r - 1$ .

Nonlinear optical materials can be modeled by assuming an electric field dependent polarization density  $P$ . In most cases the nonlinearity of the polarization density is weak compared to the linear response of the material. In such a case it is valid to expand  $P$  into a Taylor series of the applied electric fields  $E_i, E_j$  with

$$P(E) = \chi_{ij}^{(1)} E_i + \chi_{ijk}^{(2)} E_i E_j + \dots \quad (2.12)$$

For anisotropic materials  $\chi^{(n)}$  takes the form of a tensor of rank  $n + 1$ . All polarization contributions from  $\chi^{(n)}$  with  $n > 1$  are nonlinearly dependent on the electric field in the material. In the following only nonlinear contributions from the  $\chi^{(2)}$ -tensor will be considered.

For materials with a  $\chi^{(2)}$  nonlinearity two cases of wave mixing can be distinguished. In the degenerate case the electric fields  $E_i$  and  $E_j$  have the same frequency  $\omega_1$ . In this case the nonlinearity of the polarization density leads to the generation of a static polarization and a polarization with  $2\omega_1$ . The polarization density with the newly generated frequency is in turn linked to electric fields via the linear polarizability [60]. Degenerate wave mixing in  $\chi^{(2)}$  media is widely used for laser frequency doubling [61]. It has also been pointed out that the DC component can also be used for detection of amplitude modulated signals [21].

In the non-degenerate case the electric field  $E_i$  and  $E_j$  have different frequencies  $\omega_1$  and  $\omega_2$ . In this case the nonlinear polarization density will lead to a polarization with new frequency components  $\omega_1 + \omega_2$  and  $\omega_1 - \omega_2$ . Of special interest for this work is the non-degenerate case where one of the two electric fields is quasi static while the other oscillates with optical frequencies. In this case equation 2.11 can be rewritten as

$$D(\omega_2) = \epsilon_0(1 + \chi_{ij}^{(1)} + \chi_{ijk}^{(2)}E_i(0))E_j(\omega_2). \quad (2.13)$$

The change in permittivity  $\Delta\epsilon_r$  due to the static electric field  $E_i$  is in this case given by

$$\Delta\epsilon_r(\omega_2) = 2\chi_{ijk}^{(2)}E_i(0) \quad (2.14)$$

where the factor of two comes from the fact that by definition  $\omega_1 = -\omega_1 \approx 0$ . For the case of a uniaxial medium such as a poled polymer film a Cartesian coordinate system can be defined with the Z-axis along the direction of poling. Doing so the permittivity tensor  $\epsilon_r$  is diagonalized. An intuitive representation of the diagonalized permittivity tensor is the optical indicatrix given by

$$\frac{X^2}{\epsilon_{r0}} + \frac{Y^2}{\epsilon_{r0}} + \frac{Z^2}{\epsilon_{re}} = 1 \quad (2.15)$$

where  $\epsilon_{re}$  and  $\epsilon_{r0}$  are the permittivities along and normal to the optical axis. Graphically this means that the electric field  $E_i$  that corresponds to a flux density  $D$  can be found on the surface of an ellipsoid, which is oriented along the coordinate axes and whose radii are  $1/\epsilon_{ri}$ .

The electro-optic coefficient is defined as a perturbation of the optical indicatrix. For  $E_i(0)$  parallel to the Z-axis the optical indicatrix is given by

$$X^2\left(\frac{1}{\epsilon_{r0}} + r_{13}E_i(0)\right) + Y^2\left(\frac{1}{\epsilon_{r0}} + r_{13}E_i(0)\right) + Z^2\left(\frac{1}{\epsilon_{re}} + r_{33}E_i(0)\right) = 1 \quad (2.16)$$

with  $r_{13}$  and  $r_{33}$  are the electro-optic coefficients for electromagnetic waves polarized normal and parallel to the Z-axis. By introducing equation 2.14 into the indicatrix the electro-optic coefficients can be expressed as a function of the second order susceptibility  $\chi^{(2)}$

$$r_{13} = -\frac{2\chi_{ZXX}^{(2)}}{\epsilon_{r0}^2} \quad r_{33} = -\frac{2\chi_{ZZZ}^{(2)}}{\epsilon_{re}^2}. \quad (2.17)$$

In optics it is often more convenient to operate with the refractive index  $n$  given by  $\epsilon_r^2$  instead of the permittivity. For a small change in permittivity the nonlinear refractive index change  $\Delta n$  can be approximated by

$$\Delta n = \frac{\Delta\epsilon_r}{2n}. \quad (2.18)$$

Substituting 2.14 for the nonlinear permittivity change and replacing the susceptibility  $\chi^{(2)}$  by the electro-optic coefficients given in equation 2.17 Pockels formula for electro-optic materials is obtained with

$$\Delta n_0 = -\frac{1}{2}n_0^3 r_{13} E_i(0) \quad (2.19)$$

and

$$\Delta n_e = -\frac{1}{2}n_e^3 r_{33} E_i(0) \quad [62]. \quad (2.20)$$

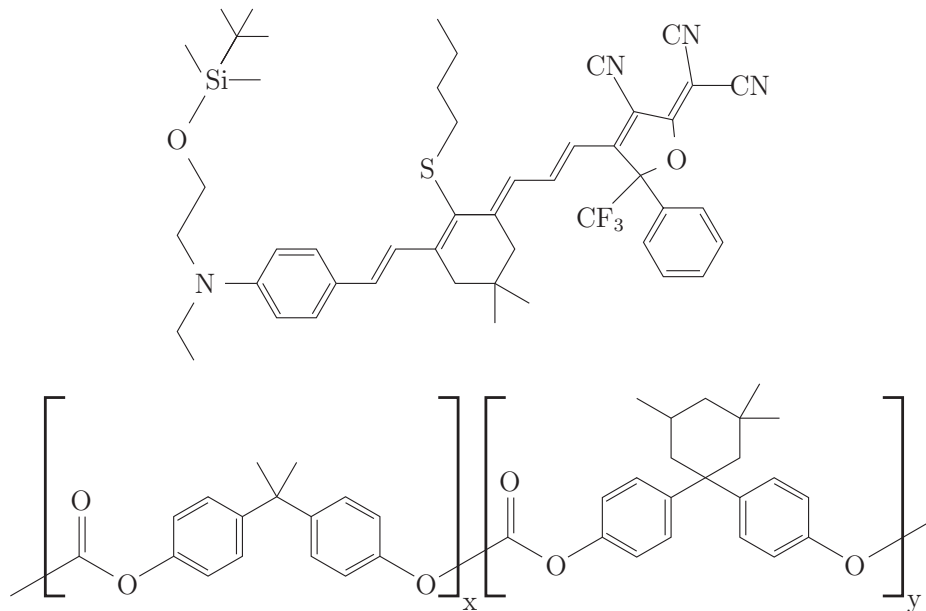


**Figure 2.3:** shows the chemical structure of the CKL1 chromophore (top) and of amorphous polycarbonate (bottom).

### 2.2.3 Polymer Material Properties

The polymer used throughout this thesis is a blend of 25 % wt CKL1 chromophore and amorphous polycarbonate (APC). The chemical structure of the constituents are given in figure 2.3. This material has a reported thin film electro-optic coefficient  $r_{33}$  of 132 and 112 pm/V at a chromophore loading of 32 % and 30 % wt. respectively [63, 64]. The refractive index and glass transition temperature are reported to be 1.64 at 1,310 nm wavelength and 135 °C. As in this thesis a lower chromophore loading is used, the refractive index of the polymer is only 1.63. Based on the reported values the expected electro-optic coefficient for 25 % wt. chromophore loading would be 103 and 93 pm/V. Also the glass transition temperature is increased to a value of about 145 °C. Figure 2.4 shows electro-optic measurements of thin films on indium tin oxide (ITO) coated glass substrates. From the linear fit a electro-optic coefficient of 88 pm/V was obtained for a poling field of 100 V/ $\mu\text{m}$ , which is in good agreement with the reported numbers from literature.

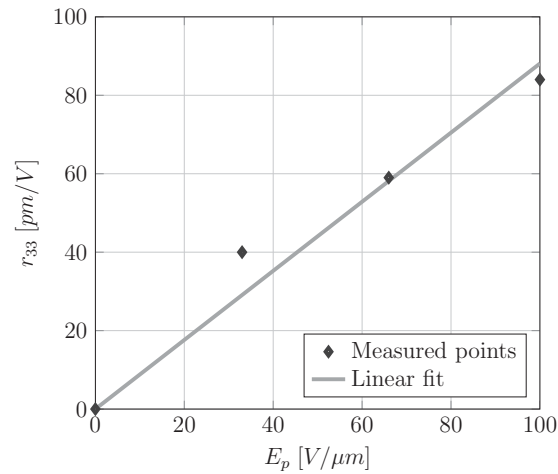


**Figure 2.4:** shows the electro-optic coefficients in thin films of amorphous polycarbonate blended with 25 % wt. CKL1 chromophore on ITO coated glass substrates for different poling fields. The samples had a film thickness of 800 nm. The samples were characterized by the Teng-Man method [65]. The measured points have been interpolated by a linear fit.

It has been shown that the electro-optic coefficient can be significantly increased by coating the ITO layer with an intermediate buffer layer. Huang et al. have shown that the electro-optic coefficient can be increased to a value of 156 pm/V using an intermediate layer of  $TiO_2$  [64].

Several works have been published using CKL1 doped APC as cladding for silicon slotted waveguide structures [66, 67, 30, 68]. The reported electro-optic coefficients in slotted waveguides of 75 to 150 nm width are ranging from 9 to 12 pm/V or a factor of 10 smaller than the thin film values.

Wang et al. have reported 59 pm/V for a slotted slow light waveguide with 320 nm slot width, which is the highest electro-optic coefficient reported for polymer infiltrated silicon slot waveguides [68]. However, due to the changed aspect ratio of the structure stray fields have stronger influence as compared to smaller slot widths. It can thus be expected that the electro-optic coefficient has a spatial dependence. Since Wang et al. do not comment on these aspects it is likely they were not taken into account and therefore the reported electro-optic coefficient of 59 pm/V is overestimated.

A detailed discussion of the low electro-optic coefficients in silicon waveguides is provided in chapters 6 and 7.

### **Polymer Deposition and Poling**

The polymer deposition has been carried out in the same way for all experiments presented in this work. First the polymer blend is dissolved in cyclopentanone. The concentration of the solution is varied according to the requirements of the experiment. The solution is kept at room temperature for twelve hours. Afterwards the solution is filtered through a 0.2  $\mu\text{m}$  polytetrafluoroethylene membrane. The solution is applied to the sample either via drop casting or via spin coating. After deposition the samples are baked in an evacuated oven for twelve hours at 90 °C in order to remove residual solvents.

For the poling procedure the samples are placed on a controlled hotplate. The slope of the heating ramp is 10 °C/minute in all experiments. The poling is carried out in inert atmosphere. The samples are kept at the final temperature for a defined dwell time and afterwards cooled down to room temperature. The poling field  $E_p$  remains in place during the whole temperature cycle. The poling field is defined by  $E_p = V/d_{poly}$  where  $d_{poly}$  and  $V$  are the film thickness and the applied voltage respectively.

## **2.3 Photonic Crystals**

Photonic crystals are composite materials, which exhibit a periodic variation of the refractive index in one, two or three dimensions. The simplest form of a photonic crystal is a periodic stack of alternating layers with high and low refractive index. These one-dimensional photonic crystals have been investigated by Lord Rayleigh already in 1887 [69]. The notion of periodic refractive index structures as crystals has been introduced by John and Yablonovitch [70, 71]. They pointed out the analogy between forbidden energy states in semiconductor crystals and the inhibition of wave propagation in media with periodic refractive index. Frequency intervals in which no propagating wave is allowed are consequently called photonic band gaps.



In order to understand some of the basic properties of photonic crystals it is helpful to start from Maxwell's equations

$$\nabla \cdot B = 0 \qquad \nabla \times H - \frac{\delta}{\delta t} D = J \qquad (2.21)$$

$$\nabla \cdot D = \rho \qquad \nabla \times E - \frac{\delta}{\delta t} B = 0 \qquad (2.22)$$

Under the assumption that all constituent materials of the photonic crystals are non-magnetic and have an isotropic and purely real permittivity  $\epsilon_r \epsilon_0$  the electric field  $E$  and electric displacement  $D$  as well as magnetic field  $H$  and the magnetic flux density  $B$  are given by

$$D = \epsilon_r \epsilon_0 E \qquad B = \mu_0 H \qquad (2.23)$$

where  $\epsilon_r$  and  $\epsilon_0$  are the relative permittivity of the dielectric and the vacuum permittivity respectively.  $\mu_0$  is the vacuum permeability. Assuming further that the electric fields are harmonic in time with frequency  $\omega$  Maxwell's equations can be written as an eigenvalue problem for the magnetic field with

$$\nabla \times \left( \frac{1}{\epsilon_0 \epsilon_r} \nabla \times H \right) = \omega^2 \mu_0 H. \qquad (2.24)$$

Equation 2.24 is called the master equation [72]. For media with spatially periodic refractive index the field distributions  $H$  that solve the master equation are subject to Bloch's theorem. For this reason field distributions in such media are called Bloch waves. Bloch waves obey the following general form:

$$H(r) \propto e^{jk_b r} u(r) \qquad (2.25)$$

where  $r$  and  $k_b$  are the coordinate vector and the Bloch wave number respectively.  $u(r)$  is a function, which has the same periodicity as the refractive index distribution. Like for electrons in a semiconductor lattice Bloch waves in photonic crystals form a band structure in the dispersion diagram. The band structure exhibits a periodicity of  $\frac{2\pi}{a}$  for the Bloch wave number where  $a$  is the spatial period of the refractive index distribution [72].

Within the band structure frequency intervals may exist where no real valued wave number exist. These frequency intervals are called photonic band gaps (PBG). For frequencies inside the PBG electromagnetic waves decay exponentially as they penetrate the photonic crystal.

### 2.3.1 Photonic Crystal Slabs

One class of photonic crystals that has attracted a large amount of attention in the last years is the photonic crystal slab. A photonic crystal slab consists of a dielectric slab, which is patterned with a regular lattice of holes. As these structures are planar they can be fabricated using established methods from semiconductor processing such as UV- or electron beam lithography. The photonic crystal parameters such as lattice type, refractive index contrast and filling fraction offer a large degree of freedom in engineering the Bloch waves inside the slab. Possible applications are grating couplers, omni-directional reflectors and self collimated beam propagation [73, 74, 75].

For many applications it is desired that the Bloch waves are vertically confined to the photonic crystal slab. In order to be confined Bloch waves need to fulfill the total internal reflection criterion given by

$$\left(\frac{\omega n}{c}\right)^2 - k_b^2 < 0 \quad (2.26)$$

where  $n$  is the cladding refractive index. Bloch modes with combinations of  $\omega$  and  $k_b$  that violate the total internal reflection can radiate energy into the mode continuum of the cladding [76]. In the dispersion diagram condition 2.26 can be represented by a cone with a radius proportional to the angular frequency  $\omega$ . This cone is called the light cone.

### 2.3.2 Lattice Defects in Photonic Crystal Slabs

Apart from the technological advantages the most important feature of photonic crystal slabs is the simple fabrication of lattice defects. Two different types of lattice perturbations can be distinguished: Line defects and point defects.

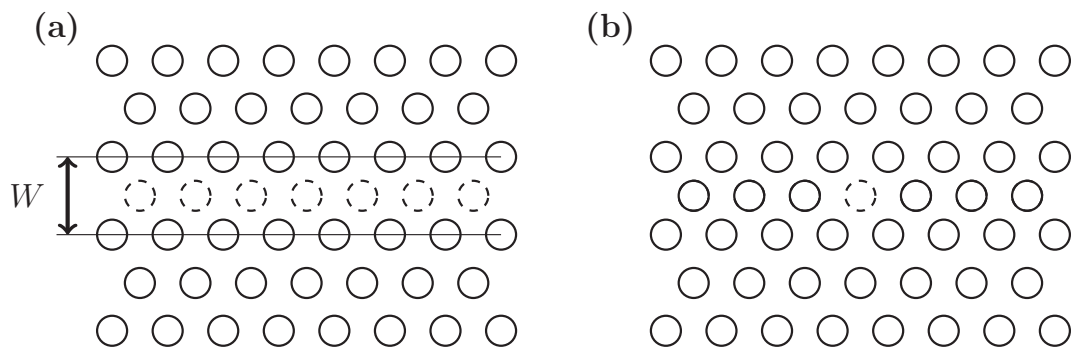


**Figure 2.5:** (a) shows the schematic of a line defect waveguide. The width of the defect is denoted by  $W$ . (b) shows the schematic of a point defect cavity where one hole has been omitted.

In a line defect the periodicity of the photonic crystal is broken along one lattice direction. Such a lattice modification can be realized by the omission or the shift of a row of holes. A schematic of a photonic crystal waveguide is shown in figure 2.5a. As a consequence of the lattice perturbation localized modes are created in the vicinity of the line defect. By proper choice of the defect width  $W$  it is possible to obtain propagating defect modes that are laterally confined by the PBG of the photonic crystal and normally confined by total internal reflection. Line defects, which exhibit propagating modes are called photonic crystal defect waveguides.

Photonic crystal defect waveguides have been extensively studied with respect to their dispersion properties. It has been shown that with these structures very low group velocities can be realized [32]. Also waveguides with engineered low group velocity dispersion have been proposed [77].

In the case of point defects the periodicity of the lattice is broken in both lattice directions. Such point defects can be realized by the omission of a single hole. Figure 2.5b shows a schematic of a point defect. As for line defects point defects with eigenfrequencies inside the photonic band gap form localized modes that are laterally confined by the photonic band gap. As propagation in the slab plane is inhibited these defects can form optical cavities with sharp resonances [78].

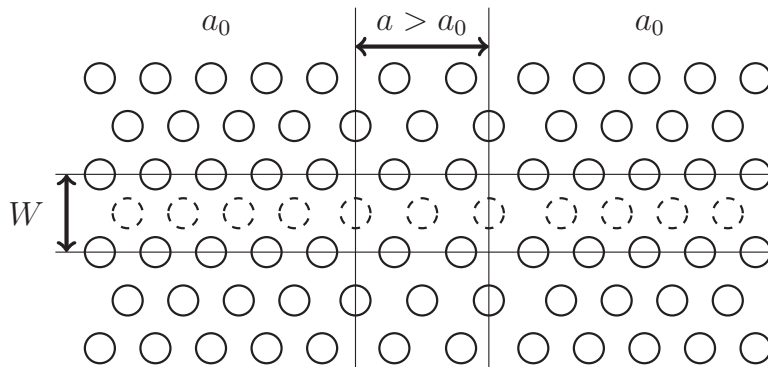


**Figure 2.6:** shows the schematic of a photonic crystal heterostructure.

A special type of point defect is the photonic crystal heterostructure, which has been invented by Song et al. [79]. A schematic of a heterostructure cavity is shown in figure 2.6. It consists of a line defect waveguide with lattice constant  $a_0$ . Along the direction of the defect waveguide a section with slightly larger lattice constant  $a$  is introduced. For this modified defect waveguide a finite frequency interval exists where the Bloch wave number is purely real for the lattice constant  $a$  and complex for lattice constant  $a_0$ . This frequency interval is called mode gap. Thus, within the mode gap optical waves are confined to the region of larger lattice constant, which gives rise to optical resonances. With this type of cavity optical resonances with a quality factor of  $3 \cdot 10^6$  have been realized [80]. At the same time these structures offer strong optical confinement in the order of a cubic wavelength. A detailed discussion of photonic crystal heterostructure resonators is given in chapter 5.

## 2.4 Numerical Methods

### 2.4.1 Finite Integration Method

In this thesis the commercially available software package CST studio suite © was used for the electro-magnetic simulation of photonic crystal structures and optical waveguides. The software uses the finite integration method developed by Weiland [81].

In this method the simulation volume is discretized into cells. The software offers tetra- or hexahedral meshes, however, the method itself is not restricted to these types of meshes [82]. In order to explain this numerical method Faraday's law of induction is considered. In the integral form it can be written as

$$\oint_{\delta A} E(\vec{r}, t) d\vec{s} = - \iint_A \frac{\delta}{\delta t} B(\vec{r}, t) d\vec{A}. \quad (2.27)$$

Secondly the simulation volume is assumed to be discretized by a Cartesian grid  $G$ . In this case the continuous electric and magnetic fluxes can be replaced by discrete voltages along the cell edges and discrete magnetic fluxes through the cell faces. Figure 2.7 shows a grid cell with discretized voltages  $e_i$  and magnetic fluxes  $b_i$ .  $e$  and  $b$  are given by

$$e_i = \int_{r_j}^{r_i} E(\vec{r}, t) d\vec{s} \quad (2.28)$$

and

$$b_i = \iint_{A_i} B(\vec{r}, t) d\vec{A} \quad (2.29)$$

where  $r_i$  and  $r_j$  are the end points of a cell edge and  $A_i$  is a cell face. With the given definitions in equations 2.28 and 2.29 Faraday's law can be rewritten in a discrete form with

$$e_i + e_j - e_k - e_l = - \frac{d}{dt} b_i. \quad (2.30)$$

Using the same definitions Gauss's Law for magnetism can be written with

$$\sum_{i=1}^N b_i = 0 \quad (2.31)$$

where the indices one to  $N$  describe the edge faces of the cell. The equations 2.30 and 2.31 can be represented in a matrix form as

$$C e = - \frac{d}{dt} b \quad S b = 0 \quad (2.32)$$

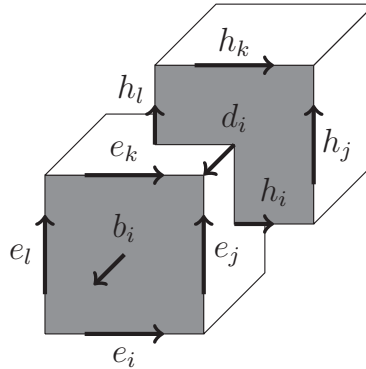


**Figure 2.7:** shows a schematic of a simulation cell and the corresponding dual cell.

where the matrices  $C$  and  $S$  determine the coordination of faces and edges with respect to each other. The entries of  $S$  and  $C$  are therefore either 1,  $-1$  or 0. In order to discretize the remaining two Maxwell's equations a dual grid  $\tilde{G}$  is defined in which the cells are centered around the nodes of the original grid  $G$ . Using the same approach as before the discrete formulation of Gauss's law and Ampere's law can be written as

$$\tilde{C}h = \frac{d}{dt}d + j \qquad \tilde{S}d = q \qquad (2.33)$$

where  $d$  and  $h$  are the electric flux and integrated magnetic field.  $j$  and  $q$  describe the current through the faces of the dual grid.  $\tilde{C}$  and  $\tilde{S}$  are coordination matrices for the dual grid. Equations 2.32 and 2.33 are called Maxwell's grid equations [83]. In addition to Maxwell's equations also the materials in the simulation domain are represented in a matrix form with

$$d = M_\epsilon e \qquad j = M_\kappa e \qquad b = M_\mu h \qquad (2.34)$$

For time domain simulations Maxwell's grid equations can be solve in a leap frogging scheme where electric fields and magnetic fluxes are calculated in an alternate fashion. The time derivatives are approximated by a difference quotient with a constant time step  $\Delta t$ . From equations 2.33 and 2.34 the electric field at the time  $T + \Delta t/2$  is given by

$$e^{T+\Delta t/2} = e^{T-\Delta t/2} + \Delta t M_\epsilon^{-1} (\tilde{C} M_\mu^{-1} b^T - j) \quad (2.35)$$

In a second step the magnetic field at time  $T + \Delta t$  can be calculated by

$$b^{T+\Delta t} = b^T - \Delta t C e^{T+\Delta t/2}. \quad (2.36)$$

The finite integration algorithm can also be used in frequency domain. Since electric and magnetic field can be considered time harmonic functions  $e^{-j\omega t}$  the electric field can be written as an eigenvalue problem with discrete eigenvalues for the frequency  $\omega$

$$\tilde{C} M_\mu^{-1} C e = \omega^2 M_\epsilon e, \quad (2.37)$$

which is the discrete representation of the wave equation [84]. Alternatively the problem can be solved for a given  $\omega$  if excitation sources are present.

## 2.4.2 Finite Difference Method for Curved Coordinate Systems

Even though most electro-magnetic problems can be treated using the finite integration method some special cases require dedicated numerical methods. One example for such a problem is the calculation of eigenmodes in curved waveguides. For eigenmode calculations with the finite integration method only material losses are taken into account while radiation losses cannot be treated. Precise knowledge of radiation losses is particularly important for ring resonators where the coupling condition depends crucially on the propagation losses [85]. Krause has shown that using the finite difference method combined with perfectly matched boundary conditions radiation losses in curved waveguide systems can be calculated [86].

The coordinate system for this case is defined such that the waveguide is curved along the  $\phi$  direction with a radius  $R$ . The vertical and radial direction are denoted by  $z$  and  $\rho$  respectively. Due to the translational symmetry in  $\phi$  direction the electric field  $e$  and the magnetic field  $h$  of the mode can be written as

$$\{e, h\}(\phi, \rho, z) = \{e_0, h_0\}^{-j\beta R\phi} \quad (2.38)$$

with  $\beta$  the complex propagation constant and  $\{e_0, h_0\}$  the wave amplitudes. Substituting equation 2.38 into the Helmholtz equation yields two differential equations

$$(1 + c\rho)^2 Lh^\rho + c(1 + c\rho)(3h_\rho^\rho + 2h_z^z) + c^2 h^\rho = \beta^2 h_\rho \quad (2.39)$$

$$(1 + c\rho)^2 Lh^z + c(1 + c\rho)h_\rho^z = \beta^2 h^z \quad (2.40)$$

where subscripts denote a derivative with respect to the specified axis and superscripts indicate the field component.  $c = 1/R$  is the curvature of the waveguide and  $L$  is the Helmholtz operator given by

$$L = \frac{\delta^2}{\delta\rho^2} + \frac{\delta^2}{\delta z^2} + k^2 n^2 \quad (2.41)$$

with  $k$  and  $n$  the free space wave number and the refractive index respectively. Replacing the derivatives with difference quotients in equations 2.39 and 2.40 an eigenvalue problem is obtained, which can be solved for the propagation constant  $\beta$  and the field components  $h^\rho$  and  $h^z$ .

Like for the finite integration method radiation losses are eliminated if perfect electric or magnetic boundary conditions are used. However, by performing a complex valued coordinate transformation in a finite layer close to the simulation boundary perfectly matched layers (PML) can be created [87]. The PML layers remove any residual reflections from the simulation boundary and thereby make it possible to calculate the radiative losses of the waveguide.



## Chapter 3

# Trimming of Silicon Ring Resonators

This chapter discusses the possibility of highly accurate trimming of silicon ring resonators by bleaching of a chromophore doped polymer cladding. Experimental results as well as parts of the text have been published in [88].

In the last couple of years silicon high Q-factor ring resonators have been studied for a variety of different applications. It has been shown that these structures can be used as highly selective filter elements, as small footprint EO-modulators and even as lasing structures [89, 90, 91]. Yet some major obstacles have averted the large scale use of these structures in commercially available products. One of these obstacles is the fact that due to fabrication tolerances the resonances of such resonators are randomly shifted in wavelength.

Zortman et al. have shown that for state of the art lithography the resonance wavelength for disc resonators on a single wafer varies by 2 nm depending on the position of the resonator on the wafer [92]. The channel spacing in a modern wavelength division multiplexing (WDM) system is 0.8 nm [93]. It is obvious that in order to use silicon ring resonators in a commercial product a trimming procedure is needed in order to correct for these random shifts.

It has been shown that the thermo-optic effect can be used to compensate for temperature and fabrication induced resonance shifts [94]. However, this trimming strategy becomes increasingly challenging when the distance between the resonators becomes small. Furthermore the power consumption of the heaters and the control circuitry add an additional power penalty to the system. Therefore it makes sense to compensate for random shifts with a passive post fabrication trimming while keeping all resonators on one chip at a constant temperature. Canciamilla et al. have recently shown that ring resonators made from chalcogenide glass can be trimmed by illumination of visible light [95]. Photosensitive polymer claddings also have been proposed to achieve ring resonator trimming [96]. Although the presented trimming strategies are likely to work for silicon ring resonators the trimming is not stable in ambient light or temperature.

In this chapter it will be shown that efficient post fabrication trimming can be achieved by bleaching of a chromophore doped polymer cladding. Since chromophore molecules with conjugated  $\pi$ -bonds are highly polarizable a host polymer doped with chromophores can have a significantly higher refractive index than the undoped host polymer. Several groups have reported that the polarizability of the chromophores can be reduced by cracking the  $\pi$ -bonds in the conjugated system. This bleaching process leads to a reduction of the refractive index of the polymer blend. Bleaching can be realized by illumination with ultra violet light (UV light) or with an accelerated electron beam. Refractive index changes due to bleaching of up to  $6.2 \cdot 10^{-2}$  have been reported [97, 98]. Grillet et al. give a comprehensive overview on the different effects that can be used to trim the refractive index [99]. It can be seen that among all listed effects bleaching shows the strongest refractive index change allowing for the largest trimming range.

Bleaching is a permanent process. For Polymethylmethacrylate doped with disperse red 1 chromophore (PMMA-DR1) Vydra et al. have shown that the refractive index of a bleached polymer film stays stable even after 24 hours in an oven at 160 °C, 40 °C above the glass transition temperature of the polymer blend [100]. Chromophore doped polymers can also act as highly effective electro-optic materials [42]. Chromophore molecules with broken  $\pi$ -bonds however do not

contribute to the electro-optic effect anymore. Nevertheless as long as the trimming does not take place in the modulation region bleaching does not constrain the functionality of the device. It is therefore conceivable that the chromophore doped polymer cladding might both serve as an active electro-optic material [101, 102] and, at a different location, as trimming material.

### 3.1 Polymer Bleaching by Ultra Violet Light

In order to investigate if APC-CKL1 can be bleached by UV light polymer thin films were produced. The polymer blend has been dissolved in cyclopentanone and was spin coated on glass substrates. The samples had a film thickness between 1.5 and 1.6  $\mu\text{m}$ .

After baking the thin films have been exposed to UV radiation from a mercury-vapor lamp. The exposure times ranged from 15 minutes to six hours. After the illumination the absorption spectra of the samples were measured by means of a Perkin Elmer Lambda series spectrometer. Figure 3.1a shows the absorption of the chromophore for different exposure times including a reference spectrum of an unexposed film. It can be seen that the characteristic absorption peak of the chromophore decreases due to the splitting of the  $\pi$ -bonds. Since the host polymer does not contribute any considerable absorption in this wavelength region the absorption of the blended polymer is proportional to the amount of intact chromophore molecules in the film. The fraction of intact chromophore molecules is therefore given by the ratio of the material absorption before and after bleaching.

For each exposure time the refractive index is measured with a Metricon prism coupler. As the exposure time is increased the measured refractive index drops due to the reduced polarizability of the broken chromophore molecules. Figure 3.1b shows the magnitude of the refractive index change as a function of the intact chromophores obtained from the transmission spectra. The measured values can be well fit with a line, which means that the concentration of intact chromophore molecules and refractive index change are proportional to each other. If the fitted line is extrapolated to the point where all  $\pi$ -bonds are split a maximum refractive

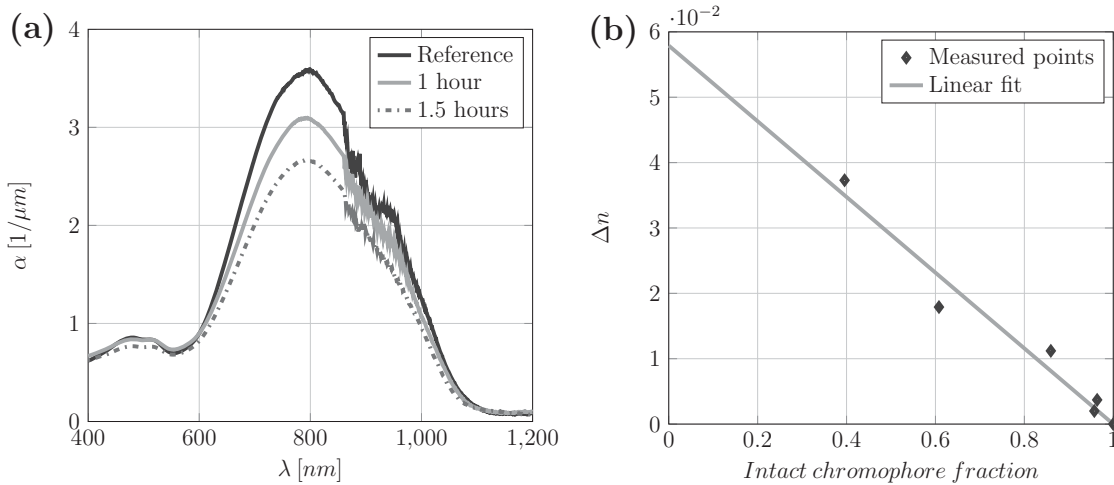


**Figure 3.1:** (a) shows the absorption spectra of polymer thin films after different UV exposure times. The jump in the spectra is a result of the lamp change in the spectrometer. (b) shows the refractive index reduction as a function of the concentration of intact chromophore molecules compared to the unbleached film.

index change of  $5.9 \cdot 10^{-2}$  is obtained. This value is similar to the values previously reported for bleached thin films of PMMA-DR1 [97].

The presented results confirm that the refractive index of APC-CKL1 can be adjusted by means of UV bleaching. The measurements indicate a simple linear dependence between the concentration of intact chromophore molecules and the refractive index of the polymer. UV bleaching of APC-CKL1 coated ring resonators could therefore be used as a trimming method. However, for the UV source used in this experiment exposure times of more than two hours were necessary to break half of the  $\pi$ -bonds.

### 3.2 Trimming of Silicon Ring Resonators by Electron Beam Bleaching

In this section post fabrication trimming of silicon ring resonators by means of electron beam bleaching will be shown. The advantage of electron beam bleaching

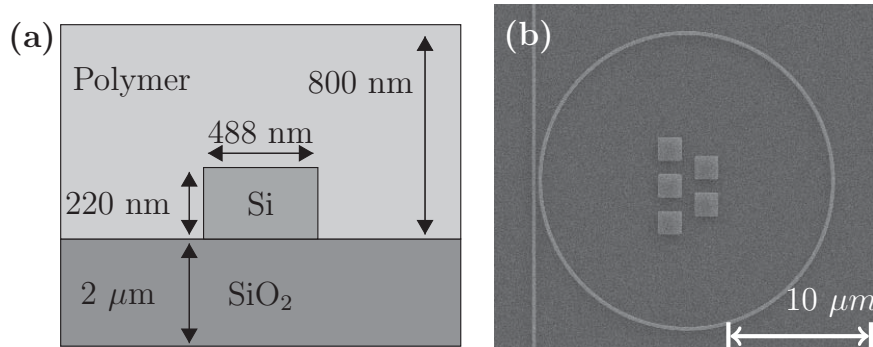


**Figure 3.2:** (a) depicts a schematic cross section of the fabricated ring resonator waveguide geometry including dimensions. (b) shows a SEM image of a ring resonator with radius of  $10 \mu\text{m}$

lies in the fact that no lithography masks are needed. For this experiment silicon ring resonators have been fabricated on a silicon on insulator (SOI) wafer using mass compatible deep UV lithography. Ring resonators with  $10 \mu\text{m}$  and  $20 \mu\text{m}$  radius were produced. Figure 3.2 shows a schematic side view of the resonator waveguide together with a scanning electron microscope (SEM) image of a fabricated structure. The ring resonators were coated with an  $800 \text{ nm}$  thick film of APC-CKL1 followed by a baking step.

All experiments have been performed using a Zeiss Supra electron beam microscope together with a Raith Elphy Plus electron beam lithography unit. An acceleration voltage of  $10 \text{ kV}$  and an aperture of  $10 \mu\text{m}$  was used for all experiments.

In order to show that precise trimming is possible it is necessary to perform a gauging experiment to determine the sensitivity and the maximum refractive index shift of the polymer blend. The gauging experiments have been performed illuminating several ring resonators with different doses of electrons. Transmission spectra of the ring resonators were taken before and after the bleaching in order to determine the shift of the resonance wavelength. For the same modal order of the resonator before and after bleaching the accumulated phase  $\phi = \beta L$  in one round trip must stay the same. Since the physical length of the ring  $L = 2\pi r$  is not altered by the bleaching process it follows that the propagation constants before

bleaching  $\beta_0$  and after bleaching  $\beta_{bleach}$  must be equal at resonance. Assuming that the bleaching of the cladding introduces only a small change in the resonance wavelength the propagation constant after bleaching can be approximated by a first order Taylor series expansion in cladding refractive index and wavelength

$$\beta_{bleach} = \beta_0 + \frac{\partial\beta}{\partial\lambda}\Delta\lambda + \frac{\partial\beta}{\partial n}\Delta n \quad (3.1)$$

where the first partial derivative can be calculated from the dispersion relation of the waveguide. The second partial derivative is a measure for the sensitivity towards refractive index changes in the cladding. Both values were determined from simulations with a free eigenmode solver, which features the calculation of eigenmodes in curved waveguide systems [86]. Cladding refractive index sensitivities  $\frac{\partial\beta}{\partial n}$  of  $7.58 \cdot 10^5/m$  and  $2.56 \cdot 10^6/m$  were obtained for the transverse electric (TE) and transverse magnetic (TM) polarized waveguide mode respectively. The derivatives towards  $\lambda$  were found to be  $-1.05 \cdot 10^{13}/m^2$  and  $-0.94 \cdot 10^{13}/m^2$  for TE and TM polarization. Since  $\beta_{bleach}$  and  $\beta_0$  are equal at resonance the propagation constant  $\beta_0$  in equation 3.1 cancels out. The refractive index change in the polymer  $\Delta n$  can be directly computed from the partial derivatives and the measured wavelength shift. It was found experimentally that the maximal refractive index change  $\Delta n_{max}$  is  $6.0 \cdot 10^{-2}$ , which matches well with the values obtained from UV bleaching before.

For modeling the bleaching process, which is described by the refractive index as a function of the electron exposure dose  $d$ , the measured data suggested that a single exponential fit is appropriate. By fitting the measured data with the model function the following expression for the refractive index change is obtained:

$$\Delta n(d) = \Delta n_{max}(1 - e^{-(d/\gamma)}) \quad (3.2)$$

with a decay constant  $\gamma$  of  $499 \mu\text{As}/\text{cm}^2$ . Figure 3.3 shows the measured values as well as the fit of the model function. With the partial derivatives given before and the maximum refractive index change a maximum resonance shift of 4.3 nm is expected for TE polarization. For TM polarization we experimentally confirmed a maximum resonance shift of 16.4 nm.

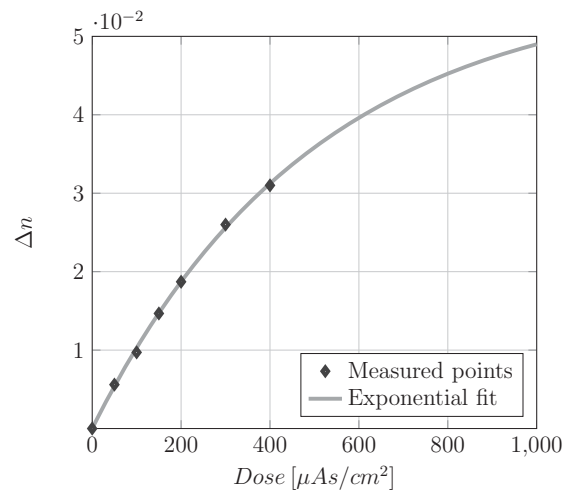


**Figure 3.3:** shows the calculated values for the refractive index change in the cladding versus the electron dose. The values have been fitted with the exponential model function.

With the gauging curve it is possible to precisely tune the resonance wavelength of a ring resonator to a given wavelength. In order to demonstrate this five ring resonators with slightly different resonance wavelengths were fabricated, which are coupled to a single bus waveguide. The resonance was varied by increasing the resonator radius of  $10 \mu\text{m}$  in  $10 \text{ nm}$  steps.

Before bleaching the resonances of the ring resonators were determined from the transmission spectrum of the device. Afterwards each ring was bleached individually with a different electron dose such that, after bleaching, all resonators

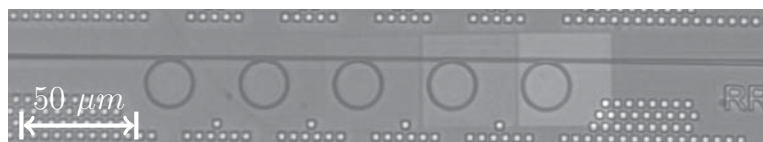


**Figure 3.4:** shows a light microscope image of bleached ring resonators. Bleached areas appear brighter in the image. The designed resonance wavelength increases from left to right. This is why the rightmost ring has to be bleached the strongest for matching the resonance wavelength of the leftmost ring.

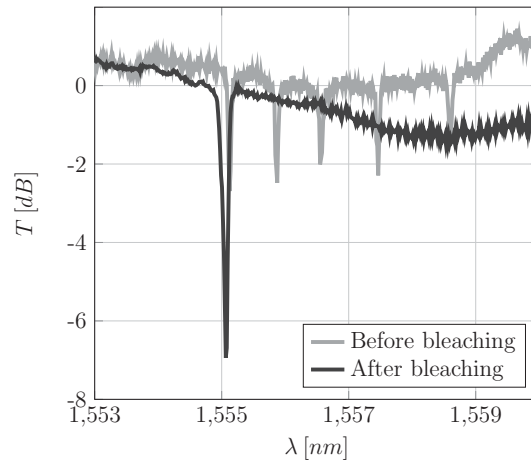


**Figure 3.5:** shows the measured transmission spectra of silicon ring resonators before and after bleaching.

are at resonance for the same wavelength. A microscope image of a device after bleaching is shown in figure 3.4. Figure 3.5 shows the transmission spectrum of a devices before and after bleaching. It can clearly be seen that the five resonance dips measured before bleaching collapse to a single dip with significantly higher extinction after bleaching. For the given parameters a resolution of the resonance shift of the bleaching process is expected to be 12 pm.

It has been reported that bleaching of polymer films increases the surface roughness of the film [100]. The increased roughness is assumed to come from gaseous residues, which are created during bleaching and leave the film through the surface. Measurements with an atomic force microscope yielded a surface roughness of 5 nm root mean square for a bleached polymer film, which is in agreement with reported results.

Furthermore it was reported that the optical loss inside bleached polymer waveguides increases by 1.1 dB/cm. The increased optical loss is supposed to come from local density fluctuations inside the polymer [100]. In order to find out if increased scattering from surface roughness or local density fluctuations pose a problem to our trimming approach we measured the Q-factors of ring resonators before and after bleaching. Figure 3.6 shows the transmission spectrum of a ring resonator that has been bleached with a dose of  $400 \mu\text{As}/\text{cm}^2$ . This dose

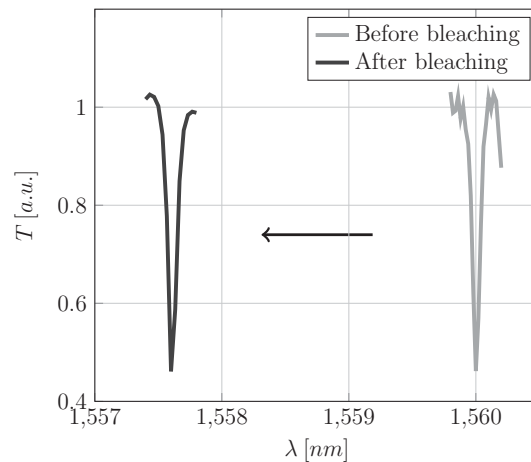


**Figure 3.6:** shows the transmission spectrum of a single ring resonator before and after bleaching with  $400 \mu\text{As}/\text{cm}^2$  dose.

is sufficient to shift the resonance by more than 2 nm. For the given device a Q-factor of approximately  $2 \cdot 10^4$  was measured before bleaching. Figure 3.6 shows that both extinction and Q-factor remain unaltered after the bleaching. Therefore for resonant structure with Q-factor below  $2 \cdot 10^4$  additional scattering losses due to bleaching are negligible. In addition, residual surface roughness could be smoothed out by a subsequent annealing process or during the poling process at elevated temperatures.

In summary it can be said that bleaching, either by UV illumination or by electron beam exposure can be used as a trimming mechanism with high wavelength resolution. This approach makes it possible to correct resonance shifts in silicon ring resonators with a resolution of 12 pm, which is almost two orders of magnitude less than the channel spacing in commercial optical telecommunication systems. The maximum expected shift of the resonance wavelength using this method is 4.3 nm and 16.4 nm for TE and TM polarized light respectively. Detrimental effects from increased surface roughness induced by the bleaching process have not been observed.



## Chapter 4

# Configurable Photonic Crystal Waveguides

**This chapter demonstrates how spatially resolved bleaching can be used to form configurable photonic crystal waveguides. Experimental results as well as parts of the text have been published in [103].**

A large part of the research that has been done in the recent years in the field silicon photonics was driven by the idea of integrating optical functionality into electronic integrated circuits. It is hoped that integrated optical circuits can remedy many of the problems of electrical interconnects today, such as cross talk, large propagation losses and high energy consumption [104, 105]. The highest integration density can be achieved using resonant structures with small foot prints such ring resonators or photonic crystal cavities. Photonic crystal waveguide based cavities in particular have attracted a considerable amount of attention since with these structures it is possible to confine light in a volume in the order of a cubic wavelength and obtain quality factors as high as  $3 \cdot 10^6$  at the same time [80]. Various concepts for filters and modulators based on photonic crystal waveguides and cavities have been realized [67, 106, 107].

So far photonic crystal waveguides and cavities are commonly optimized for a dedicated purpose including a precise engineering of the structure parameters,

which significantly increases the complexity of the design process. Additionally photonic crystals as well as ring resonators are susceptible to random fluctuations during the fabrication process resulting in random shifts of the transmission spectrum [92]. These two factors have so far averted the large scale use of these structures in highly integrated photonic systems. In order to facilitate integration and account for random process fluctuations it is therefore necessary to have generic waveguides that can be configured and trimmed according to the intended application. Another advantage of configurable waveguides is that its behavior can be altered also after the devices have been fabricated. This reduces the costs for lithography masks and lead times in the case of a design change.

The idea of using photonic crystal waveguides as configurable waveguides has been outlined by Grillet et al. [99]. The major requirement for a configurable photonic crystal waveguide is a mechanism to define a spatially resolved refractive index profile in either core or cladding of the waveguides. Accurate trimming has been shown utilizing the photorefractive effect in chalcogenide glasses [95]. The glass can either act as a cladding material for a semiconductor photonic crystal or as core material. Trimming of a photonic crystal cavity with chalcogenide glass cladding has been shown but according to the measurements additional losses due to trimming limit the quality factor to a value below  $1 \cdot 10^4$  [108]. Selective infiltration has been proposed as alternative approach. Intrinsic quality factors up to  $5.7 \cdot 10^4$  have been obtained however precise trimming of an existing cavity has not been reported [109]. Cai et al. have shown precise trimming of photonic crystal cavities using the photochromic effect in spiropyran [110]. However the photochromic effect in spiropyran is not temperature stable [111].

In the previous chapter it has been shown that electron beam bleaching of a chromophore doped polymer cladding is an elegant method for trimming silicon ring resonators. In this chapter it will be shown how configurable photonic crystal waveguides can be created by spatially resolved electron beam bleaching.

## 4.1 Tuning of Photonic Crystal Waveguides

For the experiments photonic crystal waveguides with a lattice constant  $a_0$  of 400 nm and a defect width of one lateral lattice constant, a so called W1 waveguide, were fabricated. The waveguides were structured by commercially available deep UV lithography on a SOI wafer. The thickness of the buried oxide layer and the silicon slab were  $2\ \mu\text{m}$  and 220 nm respectively. The lattice constant of the waveguide is kept constant for the whole waveguide range. At the beginning and end of the waveguides injector sections with a lattice constant of 430 nm have been attached to reduce coupling losses to the waveguide. An SEM image of a waveguide is given in figure 4.1.

The samples were spin coated with a solution of APC-CKL1 in cyclopentanone. The thickness of the polymer cladding was 500 nm. The photonic crystal waveguides were then bleached with varying electron doses to demonstrate how the transmission spectrum is shifted. All bleaching experiments have been carried out with a Raith Elphy Plus electron beam lithography unit combined with a Zeiss Supra electron microscope. The acceleration voltage was kept constant at 10 kV for all experiments.

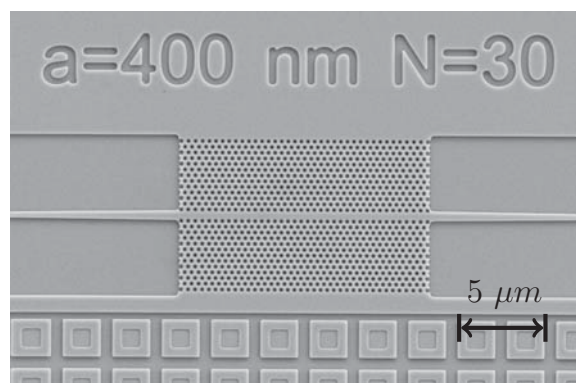


**Figure 4.1:** shows a SEM image of a  $15\ \mu\text{m}$  long photonic crystal waveguide.

Figure 4.2a shows the transmission spectrum of a  $15\ \mu\text{m}$  photonic crystal waveguide before bleaching and after bleaching with a dose of  $100\ \mu\text{As}/\text{cm}^2$  and  $200\ \mu\text{As}/\text{cm}^2$  respectively. It can be seen that the spectra are shifted in wavelength

while the fine structure of the spectrum remains unchanged. Figure 4.2b shows the shift of the transmission spectrum as a function of the applied electron dose. As described in the previous chapter the bleaching effect can be well described by an exponential function of the dose with the decay constant  $\gamma = 406 \mu\text{As}/\text{cm}^2$  determining the 1/e-value of the maximum refractive index change [88]. The lower value compared to the results obtained from ring resonators is most likely a result of the difference in the cladding height used in this case, nonetheless the maximum refractive index change is 0.06 as before. The maximum shift of the band edge obtained from the fit is 6.34 nm. For the electron beam equipment used in this work the minimum applicable dose is  $1.88 \mu\text{A}/\text{cm}^2$ , which corresponds to a shift of the band edge of 29 pm. In order to compare these figures to common lithography we define the effective lattice constant  $a_{eff}$  of the bleached waveguide as

$$a_{eff} = a_0 \frac{\lambda_{cut}}{\lambda'_{cut}} \quad (4.1)$$

with  $\lambda_{cut}$  and  $\lambda'_{cut}$  as the wavelengths of the band edge of the photonic crystal waveguide before and after bleaching respectively. The change in effective lattice constant  $\Delta a_{eff}$  is therefore given by

$$\Delta a_{eff} = a_0 - a_{eff}. \quad (4.2)$$

Using the presented numbers for the minimum band edge shift it follows that the effective lattice constant can be defined with a resolution of 7.6 pm, which is roughly a factor of 70 smaller than the lattice constant of silicon. The maximum change in effective lattice constant in this case is 1.64 nm. For state of the art CMOS processes critical structures can be fabricated with a  $3\sigma$  uniformity below 1 nm [112]. This means the effective lattice constant change shown here is sufficient to account for random process fluctuations.

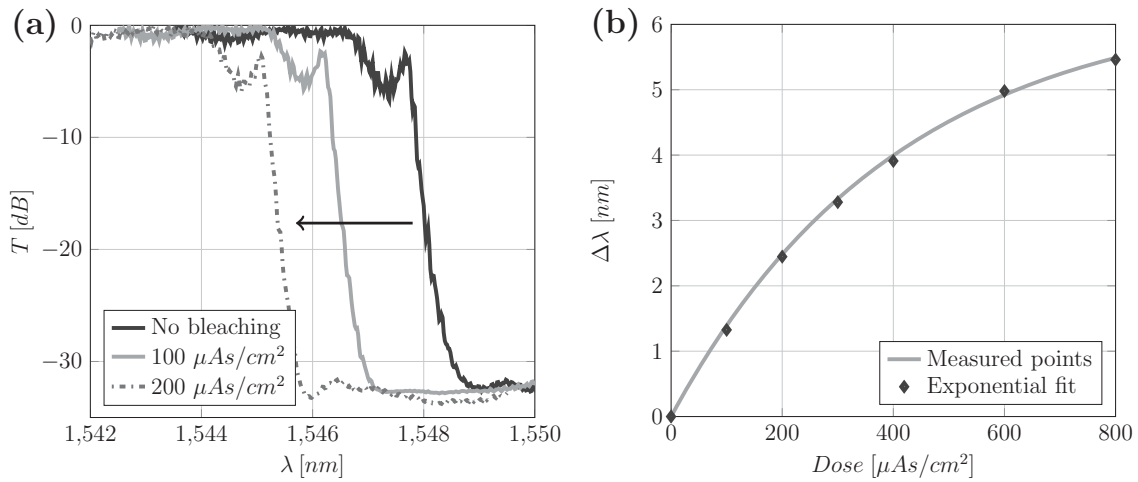


**Figure 4.2:** (a) shows the transmission spectra of a photonic crystal defect waveguide before and after bleaching. The direction of the shift for increasing dose is denoted by an arrow. (b) shows the shift of the transmission spectrum versus the electron dose. The measured values are depicted as diamonds. An exponential function is fit to the measured values.

## 4.2 Cavity Definition in Photonic Crystal Waveguides

Since photonic crystal waveguides exhibit strong reflection at the mode cut off bleaching allows to create wavelength selective dielectric reflectors. As described in Song et al. a cavity can be created from photonic crystal waveguides by adjoining a waveguide segment with lattice constant  $a$  between two waveguide segments with slightly smaller lattice constant [79]. Since the bleaching process can be used to reduce the effective lattice constant it is possible to define the reflector sections by bleaching instead of lithography [113]. The light can therefore be confined between two bleached sections.

Using the bleaching process instead of lithography the effective lattice constant reduction in the reflectors can be chosen at ease between 7.6 pm and 1.64 nm well below the geometrical lattice constant of the waveguide. In order to maintain a still moderate mode volume we bleached the reflector sections with a large dose of 544

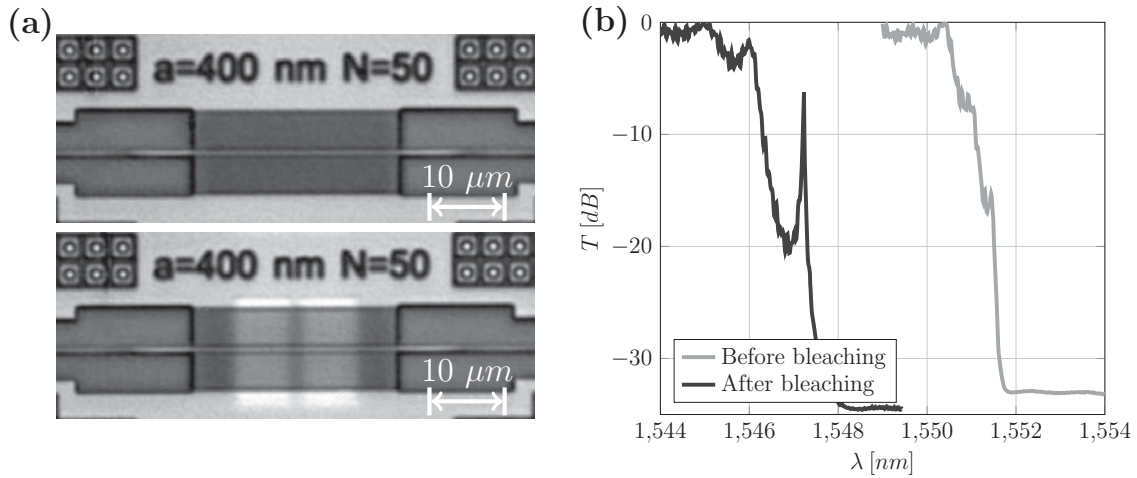


**Figure 4.3:** (a) shows light microscope images of the photonic crystal waveguides before and after bleaching. The bleached regions appear as bright rectangular areas above the waveguide. (b) shows the transmission spectrum of the device before and after bleaching. After bleaching, a cavity appears close to the band edge of the photonic crystal waveguide.

$\mu\text{As}/\text{cm}^2$ . This reduces the effective lattice constant in the reflectors by 1.2 nm. The reflector sections have a length of 17 lattice constants. The separation between the reflector sections is two lattice constants. Figure 4.3a shows light microscope images of the photonic crystal waveguide before and after bleaching. The brightened areas of the bleached mirror sections can clearly be identified. Figure 4.3b shows the transmission spectra of the waveguide before and after bleaching. After bleaching a resonance with a transmission of 26 % of the waveguide transmission is observed. A Lorentzian fit of the spectrum yields a resonator line width of 15.6 pm, which corresponds to an externally coupled Q-factor of  $9.9 \cdot 10^4$ . It can be seen that the cavity is close to the mode cut off of the bleached sections. This is expected since the unbleached waveguide section is significantly smaller than the penetration depth into the reflector sections. Previous works from Rattier et al. indicate that a larger splitting between the mode cut off and the resonance can be achieved by a larger separation of the reflector sections [114]. According to Kim et al. [115] the intrinsic Q-factor  $Q_{\text{intrinsic}}$  can be obtained from the transmission spectrum by

$$Q_{intrinsic} = \frac{Q_{total}}{(1 - \sqrt{T_{max}})} \quad (4.3)$$

where  $Q_{total}$  is the externally coupled Q-factor of the cavity and  $T_{max}$  is the maximum transmission of the cavity. From this an intrinsic Q-factor of  $2.6 \cdot 10^5$  is obtained, which is the highest reported Q-factor for a photonic crystal cavity with a polymer cladding so far.

### 4.3 Trimming of Photonic Crystal Cavities

For some applications such as coupled resonator waveguides or photonic molecules different cavities have to be adjusted to the same resonance wavelength [116, 117]. In order to demonstrate that this is also possible with bleaching we define a photonic crystal cavity. The bleaching dose for the reflectors is  $544 \mu\text{A}/\text{cm}^2$  as before. After measuring the spectrum the previously unbleached center of the cavity was illuminated with a dose of  $27 \mu\text{A}/\text{cm}^2$ . This dose corresponds to an effective change of the lattice constant of 108 pm, which is still a factor of five smaller than the silicon lattice constant. Since the bleached region only has a length of 800 nm proximity effects start to play a role for this experiment. A 1/e width of the electron beam of 117 nm close to the silicon was computed by Monte Carlo simulations using the NANOpecs software. This reduces the average refractive index change by 16 % compared to the ideal step index profile. Figure 4.4a shows simulated scattering trajectories for a 500 nm polymer cladding on silicon. Taking into account the proximity effect an expected resonance shift of 78 pm wavelength is obtained from a finite integration time domain simulation.

For the experiment where trimming of an existing cavity is demonstrated it is important to exclude any shifts of the cavity due to the thermo-optic effect. The measurements for this experiment were performed on a temperature stabilized sample holder. Figure 4.4b shows the measured thermo-optic shift of the resonance frequency with varying temperature of the sample holder. From a linear fit it is found that the thermo-optic shift of the cavity is  $50 \text{ pm}/^\circ\text{C}$ . For the experiment the

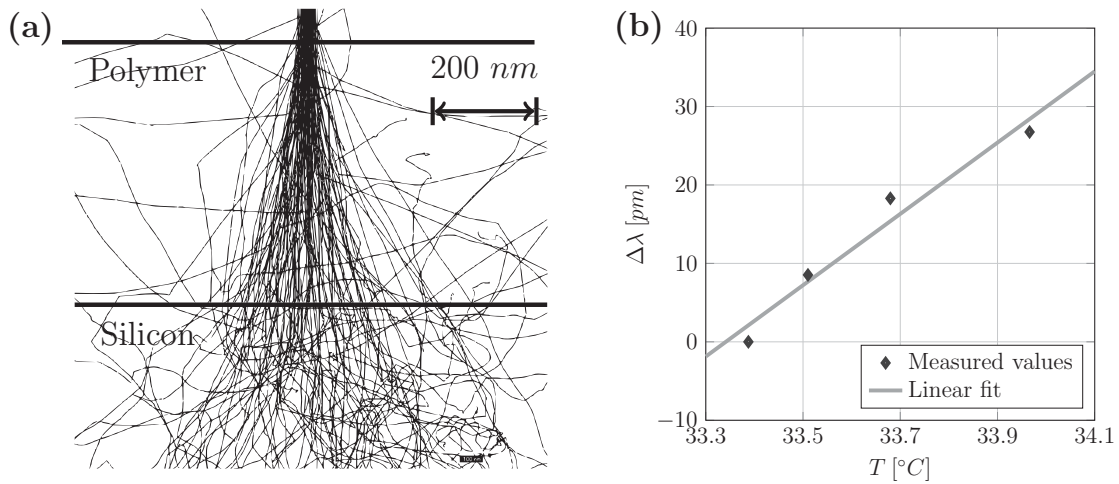


**Figure 4.4:** (a) shows simulated electron scattering trajectories at 10 kV acceleration voltage and 500 nm polymer thickness. (b) shows the measured resonance wavelength shift as a function of temperature. The measured points have been interpolated by a linear fit.

temperature of the sample holder and the ambient temperature were kept constant with an accuracy of better than 0.1 °C leading to an expected temperature induced shift of less than 5 pm.

The measured transmission spectra before and after trimming are given in Fig. 4.5. The spectra are fit with a Lorentzian function. A shift of the resonance of 73 pm is obtained from the fit parameters. Besides the good agreement between numeric and experimental results it is important to note that neither the Q-factor nor the maximum transmission change significantly due to the bleaching step. This shows that the penetration depth into the reflectors and the coupling strength of the cavity is nearly unaltered.

In summary, it has been shown that electron beam bleaching of a polymer cladding allows to create configurable photonic crystal waveguides. The effective lattice constant can be changed spatially resolved with 7.6 pm resolution, which is much smaller than the atomic lattice constant of silicon. In order to demonstrate the versatility of this fabrication method a cavity with an intrinsic Q-factor of  $2.6 \cdot 10^5$  has been fabricated. Furthermore it has been shown that an existing photonic

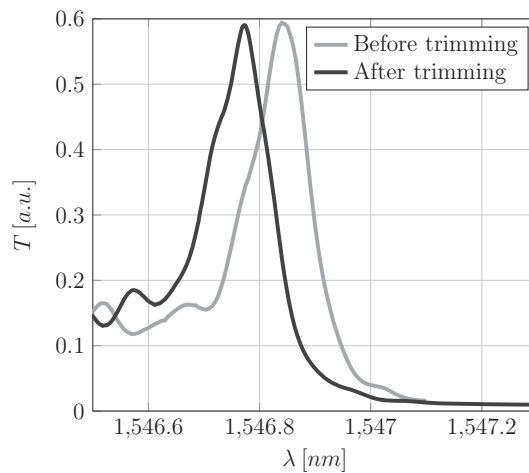


**Figure 4.5:** shows the transmission spectrum of a bleached photonic crystal cavity before and after trimming the center of the cavity. The transmission is normalized to the maximum pass band transmission of the waveguide. The resonance of the cavity is shifted by 73 pm after bleaching.

crystal cavity can be trimmed with a resolution of 73 nm wavelength. Since the described method does not impose any restrictions on the defined refractive index configurable waveguides can also be used to define more complicated structures such as cavities with graded reflectors as will be shown in chapter 5.



## Chapter 5

# Photonic Crystal Resonators with High Quality Factors

**In this chapter the mechanisms that influence the quality factor of photonic crystal cavities. Different techniques are discussed, which lead to an enhancement of the quality factor. Numerical results as well as parts of the text in section 5.2 been published in [118].**

The idea of combining silicon photonic crystal resonators with electro-optic polymers has first been proposed by Wülbern et al. [119]. They showed that using photonic crystal cavity that is infiltrated by electro-optic polymer modulation voltages as low as 1 V can be expected using a cavity with a quality factor of 8,000. At the same time the potential modulation bandwidth is as high as 100 GHz. One particular advantage of photonic crystal cavities is the strong confinement of light inside the resonator. This allows to bring the electrical contacts very close to center of the cavity without suffering excessive optical losses.

Later they succeeded in experimentally demonstrating electro-optic modulation in a polymer infiltrated photonic crystal cavity. However, two major challenges remained unresolved. The first challenge was the low quality factor of the cavity, which was only one third of the desired value of 8,000 [66]. The second challenge was the low in-device electro-optic coefficient. Both the low quality factor and

the low electro-optic coefficient lead to an increased modulation amplitude. This chapter provides an analysis of the mechanisms, which govern the quality factor in photonic crystal cavities. Different approaches to improve the quality factor will be discussed. The challenge of obtaining higher in-device electro-optical coefficients are addressed in the chapters 6 and 7.

## 5.1 Quality Factors in Single Defect Heterostructures

This subsection discusses the mechanisms of vertical and lateral energy leakage using the example of a photonic crystal heterostructure with a single center defect. As a starting point for this analysis the same photonic crystal waveguide parameters as in Wülbern et al. are chosen [119]. The hole radius  $r$  is  $0.3a$  where  $a$  is the lattice constant in propagation direction. The center defect has a width of  $1.4\sqrt{3}a$ . Only the slot width was reduced to 100 nm in order to shift the defect mode to lower frequencies. Figure 5.1a shows a unit cell of the photonic crystal waveguide and the electric field distribution of the defect mode at  $k = 0.5\frac{2\pi}{a}$ . Figure 5.1b shows the band diagram of the photonic crystal waveguide. The light cone is depicted with a dark shaded region. Dielectric and air bands are represented by bright shades.

For a vertically symmetric cladding coupling between the defect modes, which are transverse electrically (TE) polarized and the transverse magnetically (TM) polarized slab modes is not allowed. In the waveguide geometry chosen here however, the refractive index of the polymer cladding is higher than for the underlying glass layer. Due to the breaking of vertical symmetry by the asymmetric cladding the TE and TM polarization cannot be defined anymore [120]. If the vertical asymmetry is weak the modes still resemble the previous TE and TM modes. In the following they will therefore be called quasi TE and quasi TM modes. Due to the broken symmetry in vertical direction coupling between the two polarizations is possible if frequency and wave vector are matching. Therefore quasi TM modes need to be taken into account in the band diagram. The dispersion relation of the quasi TM mode guided by the silicon slab in figure 5.1 is depicted in green.

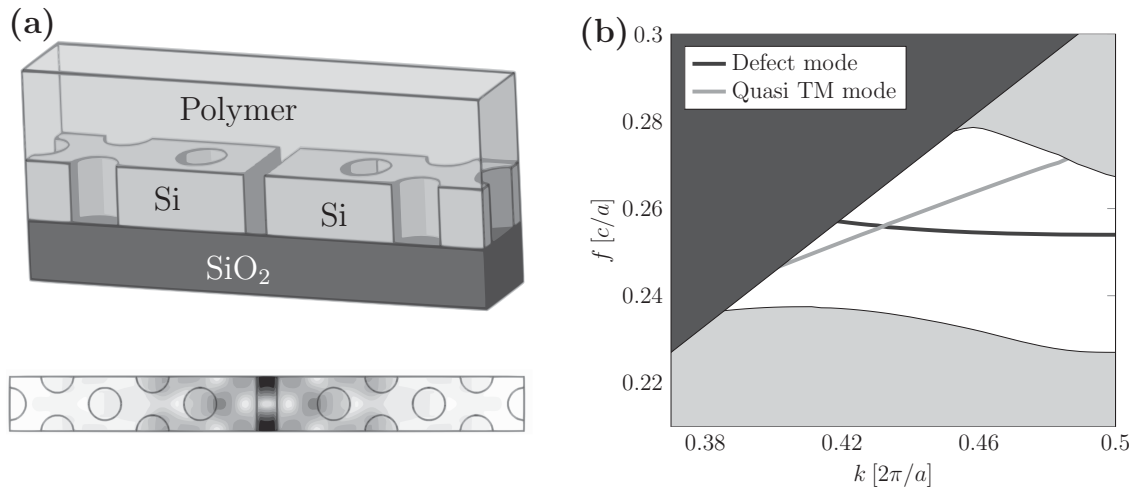


**Figure 5.1:** (a) shows the unit cell of the photonic crystal waveguide and the magnitude of the electric field distribution at  $k=0.5\frac{2\pi}{a}$ . The propagation direction is normal to front surface. (b) show the corresponding band diagram. The defect mode and the quasi TM mode are depicted in blue and green respectively.

Considering a vertically asymmetric cladding has high practical relevance because up to now silicon photonic crystals with vertically symmetric polymer cladding have not been reported. The removal of the buried oxide by means of hydrofluoric acid is an established process in CMOS fabrication [121, 122]. Nevertheless embedding a photonic crystal slab in polymer is challenging. The polymer infiltration of the volume that is formed by the etched glass below the silicon slab is likely to leave voids and the drying of the solvent can lead to stresses and deformations of the slab.

As described in chapter 2.3 a cavity can be formed from a photonic crystal waveguide by introducing a region with slightly larger lattice constant. Due to the spatial confinement of the cavity the resonant mode cannot be described anymore as an isolated point in the band diagram [123]. Instead the wave vector of the cavity becomes a continuous spectrum, which is given by the Fourier transform of the cavity field distribution. Part of the  $k$ -vector spectrum couples to the light cone and the quasi TM mode of the silicon slab. Undesired coupling between the

localized cavity mode and the light cone as well as the quasi TM mode leads to energy leakage, which limits the intrinsic quality factor of the cavity [124].

Englund et al. have derived the following expression for the vertically radiated power  $P$  given by

$$P \approx \frac{\eta}{2\lambda^2 k} \int_{k_{\parallel} \leq k} \frac{dk_x dk_y k_z}{k_{\parallel}^2} \left[ \frac{1}{\eta^2} |\mathcal{F}\{E_z\}|^2 + |\mathcal{F}\{H_z\}|^2 \right] \quad (5.1)$$

where  $\lambda$  and  $\eta$  are the resonance wavelength and the free space admittance given by  $\sqrt{\frac{\mu_0}{\epsilon_0}}$  [125].  $\mathcal{F}$  denotes the Fourier transform and  $k_{\parallel}$  and  $k_z$  correspond to the in-plane and out of plane k-vector components.  $E_z$  and  $H_z$  are electric and magnetic field components normal to the silicon slab taken in the centre of the slab plane.

For a vertically symmetric cladding the symmetry enforces that the electric field components in the centre of the slab lie inside the slab plane for the TE polarization while the magnetic field is pointing out of the slab plane. In this case the  $E_z$  term in equation 5.1 becomes zero and only the  $H_z$  term contributes to the vertical radiation. This is not strictly true anymore for a vertically asymmetric cladding. However, as discussed before the modes inside the photonic crystal slab are not strongly altered provided that the refractive index contrast between top and bottom cladding is weak. Therefore it is still valid to assume that the  $E_z$  part of equation 5.1 is negligible compared to the  $H_z$  contribution.

Figure 5.2 shows the out of plane magnetic field distribution and k-vector distribution of a cavity with a centre defect length of two lattice constants and a lattice constant mismatch of 10 nm. The intersection with the light cone is depicted by a white circle. The part of the spectral power density which extends farthest into the light cone lies on the  $k_x$ -axis. Therefore the further analysis will be focused on strategies to reduce the leakage through the  $k_x$  component of the cavity field distribution.

By limiting the discussion to the  $k_x$  contribution energy leakage out of the cavity becomes a one-dimensional problem

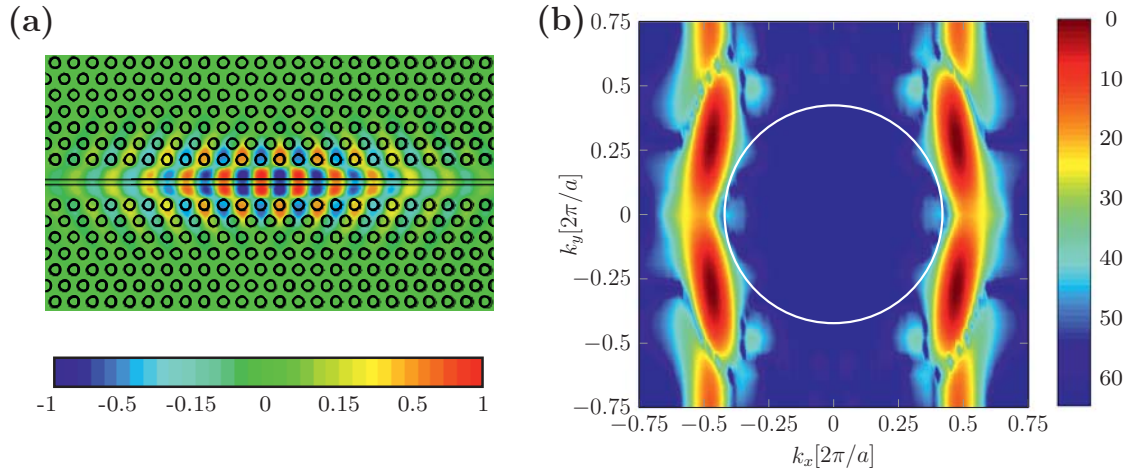


**Figure 5.2:** (a) shows the magnetic field distribution of a photonic crystal heterostructure cavity. (b) shows the corresponding  $k$ -vector spectrum in dB scale. The intersection with the light cone is depicted by a white line.

$$P \propto \frac{\eta}{2\lambda^2 k} \int_{k_x \leq k} \frac{dk_x \sqrt{k^2 - k_x^2}}{k_x^2} |\mathcal{F}\{H_z\}|^2 \quad (5.2)$$

where  $k$  is the wave vector in the cladding given by  $\frac{2\pi}{\lambda n}$  and  $n$  is the cladding refractive index. In order to increase the quality factor of the cavity the coupling to the quasi TM mode and the light cone must be reduced. The simplest approach to reduce the leakage of the cavity energy is to delocalize the resonant mode spatially. Based on the scaling property of the Fourier transform a more delocalized spectrum results in a narrower  $k$ -vector distribution which in turn reduces undesired coupling to the light cone or to the quasi TM mode.

A delocalization of the cavity field distribution can be realized in several ways. One approach is to increase the length of the centre defect. Prusser et al. have shown the enhancement of the quality factor by this method for silicon waveguide based Fabry-Perot resonators [126].

A second way to delocalize the resonant field distribution is the reduction of the mode mismatch between the cavity center and the reflector section [127]. In the double heterostructure cavities considered here the mode mismatch is given by the mismatch in lattice constant  $\Delta a$  between the center defect and the reflector sections.

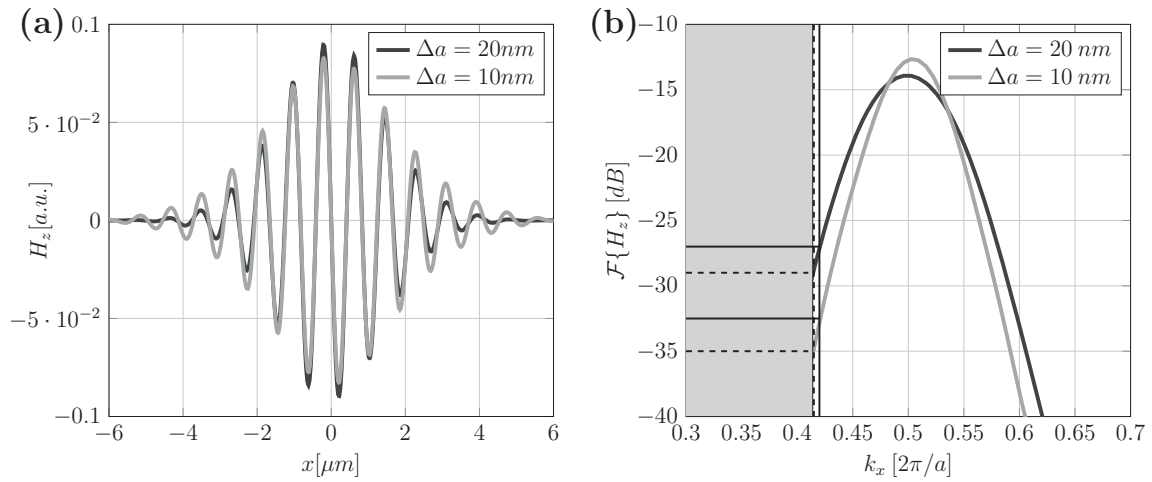


**Figure 5.3:** (a) shows the vertical magnetic field distribution along the waveguide direction. The fields are normalized to have constant energy. (b) shows the corresponding  $k$ -vector spectrum. Intersections with the QTM mode and the light cone are depicted by bold and dashed lines respectively.

Figure 5.3 shows the vertical magnetic field and the corresponding  $k$ -vector spectrum along the  $x$ -axis of two heterostructure cavities of 10 nm and 20 nm lattice mismatch. The field distributions for the vertically symmetric and asymmetric cladding are almost identical. It can be seen that the cavity with lower lattice constant mismatch has a broader spatial field distribution and a narrower  $k$ -vector distribution. In the vertically asymmetric case the quality factors of the cavities are  $2.5 \cdot 10^5$  and  $6.0 \cdot 10^4$  for a lattice constant mismatch of 10 nm and 20 nm respectively. The quality factor for 10 nm lattice constant mismatch is 4.2 times larger than for 20 nm lattice constant mismatch. This is in good agreement with the ratio of power spectral densities at the intersection of the quasi TM mode at  $k_x = 0.42$ .

The quality factor for the vertically symmetric polymer cladding is  $1.8 \cdot 10^5$  and  $4.4 \cdot 10^5$  for 10 nm and 20 nm lattice constant mismatch respectively. The ratio between the two quality factors is very close to the ratio of spectral power densities at the cut with the light cone.

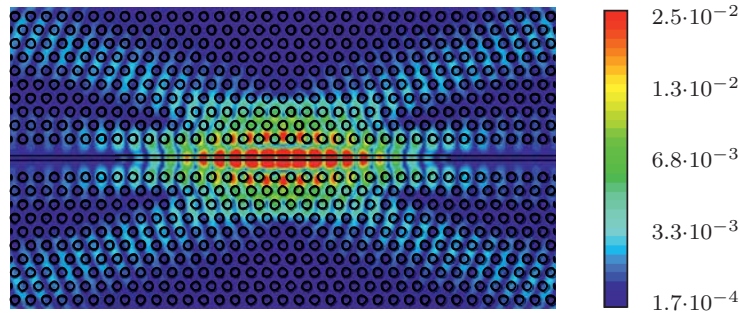


**Figure 5.4:** shows the magnetic field in the slab plane. The field is normalized to the maximum value of the magnetic field in the cavity.

The coupling to the quasi TM mode can also be directly observed in numerical simulations by plotting the magnetic field in the slab plane. Figure 5.4 shows the tangential magnetic field. The presented results support the validity of the one-dimensional approximation introduced in 5.2 and underlines the importance of coupling to the quasi TM mode for the quality factor.

Even though a further enhancement of the quality factor is observed in numerical simulations for a lattice mismatch below 10 nm this approach has experimental limitations. In order to have reproducible quality factors the mode gap of the defect should be significantly larger than the random frequency shifts of the cut off frequency along the waveguide due to process fluctuations. This requirement defines the lower limit for the lattice constant mismatch. It was shown in chapter 4 that for unslotted photonic crystal waveguides the lattice constant mismatch can be as low as 1.2 nm. Slotted waveguides however, exhibit larger scattering indicating a stronger sensitivity towards process fluctuations [128], which is why larger mode gaps are required for the slotted photonic crystal geometry.

Despite the fact that the lattice constant mismatch and the length of the cavity region are independent parameters it is important to note that a change in length of the centre defect can indirectly influence the penetration depth. Figure 5.5 shows the band diagram close to the cut off region at  $k=0.5\frac{2\pi}{a}$ . For frequencies below the cut off frequency the k-vector becomes complex leading to an exponentially decaying field. The complex part of the k-vector is equal to the decay constant

of the field. The complex  $k$ -vector as a function of frequency can be obtained by expanding the dispersion relation close to cut off into a Taylor series

$$\omega(k) = \omega_0 + \frac{1}{D}(k - 0.5\frac{2\pi}{a})^2 + O((k - 0.5\frac{2\pi}{a})^3) \quad (5.3)$$

with  $\omega(k)$  the frequency of the electromagnetic state corresponding to the given  $k$ -vector.  $\omega_0$  is the cut off frequency of the mode at  $k = 0.5\frac{2\pi}{a}$ .  $D$  describes the curvature of the waveguide dispersion relation.  $O((k - 0.5\frac{2\pi}{a})^3)$  is the residual approximation error. Close to the cut off frequency  $k$  can be approximated by the complex variable  $\tilde{k}$

$$\tilde{k} \approx 0.5\frac{2\pi}{a} + i\alpha \quad (5.4)$$

where  $\alpha$  is the decay constant of an electromagnetic wave inside the photonic crystal waveguide [129]. At the same time  $\alpha$  is the inverse of the penetration depth  $d_{pen}$ . Introducing the expression 5.4 into equation 5.3 yields

$$\omega - \omega_0 = \Delta\omega = -\frac{1}{D}\alpha^2 + O((i\alpha)^3). \quad (5.5)$$

Equation 5.5 can then be used to compute the the decay constant for frequencies below the waveguide cut off. Figure 5.5a shows the complex band diagram computed from equation 5.5. Heterostructure cavities have been simulated with a centre defect length  $N$  of two, four, six and eight lattice constants. The resonance frequencies are indicated by blue markers. The length of the centre defect is increasing along the arrow direction. It is observed that the resonance frequency of the cavity is monotonously decreasing as the lattice centre defect becomes larger. This behavior is well known for Fabry-Perot resonators and it follows from the requirement that the accumulated phase in one round trip must be a multiple of  $2\pi$  [114]. As a consequence of the decreasing frequency the decay constant increases along the complex dispersion.

As the the decay constant is increasing for an increasing length of the centre defect the penetration depth decreases. Figure 5.5b shows the penetration depths extracted from the band diagram compared to those extracted from the simulated

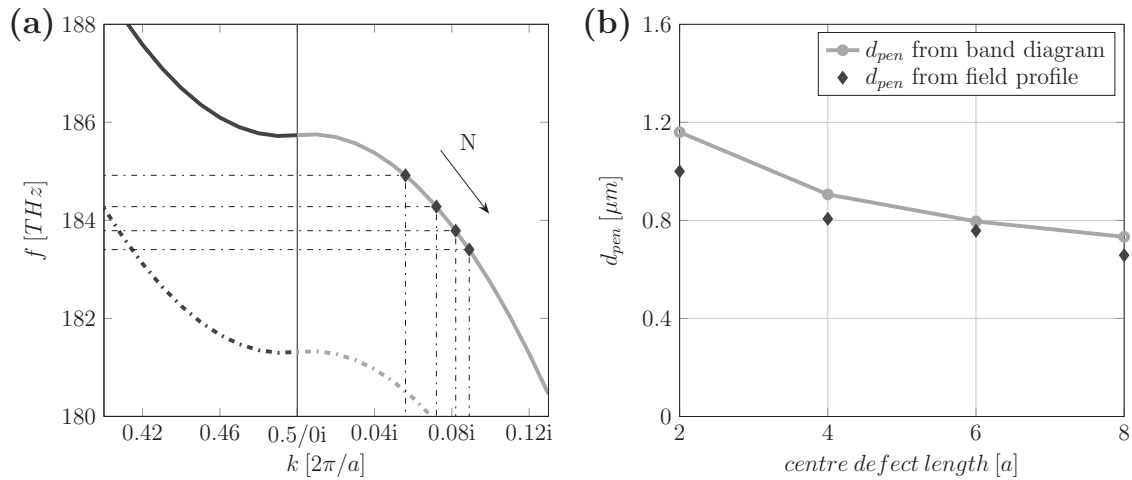


**Figure 5.5:** (a) shows the complex band diagram of a heterostructure with 10 nm lattice mismatch. Bold and dashed lines denote the dispersion of the defect mode in the defect and reflector section respectively. Simulated cavities are depicted as blue diamonds. The arrow indicates the direction of increasing centre defect length  $N$ . (b) shows the penetration depth for different defect lengths extracted from the band diagram and from the field profile.

field profiles. From figure 5.5 it can be understood that delocalization is also taking place for small defect sizes. Using a small defect length it is therefore possible to maintain a sufficiently large mode gap and still obtain high quality factors due to the delocalized mode profile.

Following the arguments given before it would be expected that that an increased penetration depth leads to a larger cavity quality factor. It would also be expected that a longer centre defect leads to a larger quality factor. Figure 5.6 shows the simulated quality factors for cavities with vertically symmetric polymer cladding and vertically asymmetric cavities with glass substrate and polymer top cladding. It can be seen that both vertically symmetric and asymmetric cavities exhibit a minimum in quality factor for a defect length of four lattice constants. Both smaller and larger defects lead to higher quality factors. A reduction of the centre defect length leads to an enhancement of almost a factor of two in quality factor for both the vertically asymmetric and the vertically symmetric cavity. An

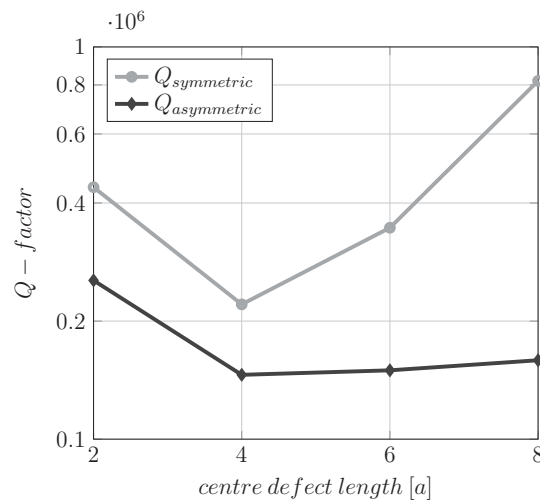


**Figure 5.6:** shows the  $Q$ -factor as a function of the defect length.

increase of the centre defect length beyond four lattice constants does not lead to a significant enhancement of the quality factor for the vertically asymmetric structure. For the vertically symmetric structure the quality factor increases by a factor of three by increasing the length of the center defect from four to eight.

In summary it can be said that the simulated quality factors and field profiles support the one-dimensional approximation for energy leakage from the cavity. For photonic crystal cavities with vertically symmetric cladding it was shown that the quality factor can be increased by increasing the length of the center defect. In the case of a vertically asymmetric cladding no significant improvement is observed. The analysis shows that for vertically asymmetric photonic crystal cavities high quality factors can only be achieved if the penetration depth into the reflector sections is large. This can either be achieved by a reduction of the lattice constant mismatch or by a reduction of the centre defect length. From the fabrication point of view it is advantageous to work with small defect dimensions and moderate lattice constant mismatches instead of small lattice constant mismatches as these structures are likely to be more tolerant towards process fluctuations.

## 5.2 Multistep Heterostructures with Gaussian Field Envelopes

The preceding analysis has shown that the field profile of the cavity mode and its corresponding Fourier spectrum are crucial for the quality factor of a photonic crystal cavity. It has also been shown that the quality factor in single step heterostructures is mainly determined by the penetration depth into the reflecting section. This qualitative argument is correct if the field distributions, which are compared have a similar overall shape. In general k-vector distribution is given by the Fourier transform of the cavity field envelope, which offers an option to further enhance the quality factor of photonic crystal cavities [123].

Akahan et al. have shown that the quality factor of a cavity can be significantly increased if the envelope of the cavity field distribution has a Gaussian shape [123]. Gaussian functions are good candidates as field envelopes because they have an optimal time bandwidth localization leading to a very narrow k-vector distributions [130].

In general synthesizing the refractive index distribution, which leads to a given electromagnetic field distribution is a challenging problem. Englund et al. have proposed a synthesis method for dielectric cavities [125]. Lu and Vučković have presented a method for non-resonant structures [131, 132].

For the special case of photonic crystal cavities some approximations can be made, which greatly simplify the synthesis of the desired field envelope. In the first step the desired Gaussian field envelope  $H_{env}$  is defined by

$$H_{env}(x) = H_0 \exp\left(-\frac{x^2}{2\sigma^2}\right) \quad (5.6)$$

with  $\sigma$  as the standard deviation of the Gaussian function and  $H_0$  a constant to normalize the envelope energy to unity. For the single step heterostructure it has been shown that the field inside the reflector section decays exponentially with a fixed decay constant  $\alpha$ . The field distribution  $H_z(x)$  inside the reflector section can therefore be written as

$$H_z(x) \propto \exp(-\alpha x) \quad (5.7)$$

By comparing equation 5.6 with equation 5.7 it is found that  $\alpha$  needs to be a linear function of the space variable  $x$  with

$$\alpha = \frac{x}{2\sigma^2} \quad (5.8)$$

in order to obtain a Gaussian field envelope. Inserting  $\alpha$  into the complex dispersion relation given by equation 5.5 yields

$$\omega(x) - \omega_0 = \Delta\omega(x) = -\frac{1}{4D}\left(\frac{x}{\sigma^2}\right)^2 + O(x^3). \quad (5.9)$$

Provided that the resonance frequency is close to the lower edge of the mode gap  $\Delta\omega$  represents the difference between the resonance frequency of the cavity and the local mode cut off of the photonic crystal waveguide. Equation 5.9 shows that a Gaussian envelope function is obtained for a quadratic variation of the cut off frequency.

In the case of a single step heterostructure cavity the cut off frequency was varied by the lattice constant. However, other parameters can be chosen to generate the spatial variation of the cut off frequency. Cavities with Gaussian field envelopes have been reported for a spatial variation of the lattice constant, a hole diameter and the width of the defect waveguide [124, 133, 134].

It has been noted before that the the smallest changes in the photonic crystal lattice are limited to a few nanometers due to the limited resolution of the fabrication process. Using the bleaching process introduced in chapter 4 the local cut off frequency of the photonic crystal waveguide can be adjusted very accurately, which is why in this case the cladding refractive index is chosen as parameter to define the local cut off frequency. For comparability the same waveguide geometry is chosen as in section 5.1. Since the bleaching induced changes in the cladding refractive index  $\Delta n$  are sufficiently small the local cut off frequency  $\omega$  can be considered proportional to the change in cladding refractive index

$$\omega(x) - \omega_0 = \gamma(n(x) - n_0) = \gamma\Delta n(x) \quad (5.10)$$

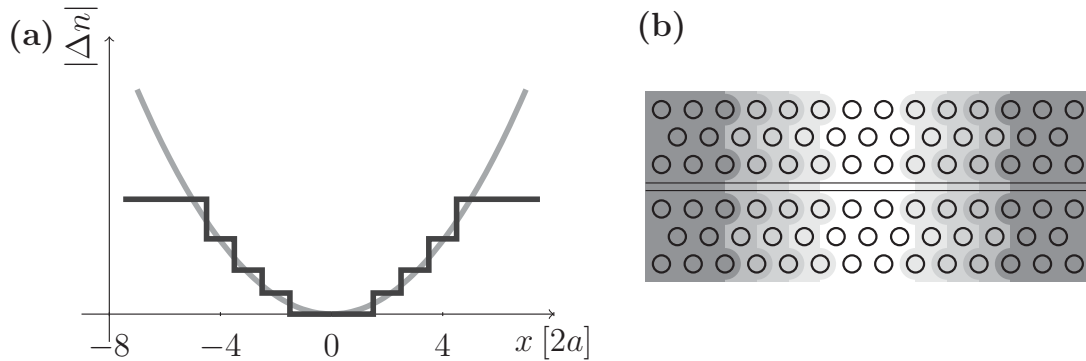


**Figure 5.7:** (a) shows schematic of the refractive index distribution. (b) shows the shape of the bleached sections which were used for the experiments. Darker shades of gray indicate a higher electron dose and thus lower refractive index.

where  $n_0$  is the unbleached cladding refractive index.  $\gamma$  is given by  $\frac{\delta\omega}{\delta n}|_{n=n_0}$  and describes the sensitivity of the cut off frequency towards changes in the cladding refractive index. Substituting 5.10 into 5.9 yields

$$\Delta n(x) = -\frac{1}{4D\gamma}\left(\frac{x}{\sigma^2}\right)^2 + O(x^3). \quad (5.11)$$

Hence a parabolic variation of the cladding refractive index will result in the desired Gaussian field envelope. It is interesting to note that explicit knowledge of the structure sensitivity and the dispersion are not required in order to synthesize a Gaussian field envelope. This becomes clear when substituting  $\gamma$  by an alternated value  $\gamma' = r\gamma$  where  $r$  is a positive factor. Equation 5.11 will then turn into

$$\Delta n(x) = -\frac{1}{4D\gamma'}\left(\frac{x}{\sigma^2}\right)^2 + O(x^3) = -\frac{1}{4D\gamma}\left(\frac{x}{(\sigma\sqrt{r})^2}\right)^2 + O(x^3) = -\frac{1}{4D\gamma}\left(\frac{x}{\sigma^2}\right)^2 + O(x^3) \quad (5.12)$$

Provided that the local cut off frequency is still proportional to the change in the cladding refractive index any variation of  $\gamma$  or  $D$  will only lead to a change in the standard deviation of the Gaussian envelope. The overall shape of the envelope is not affected.

In order to facilitate the numerical simulations and experiments the parabolic refractive index distribution in the cladding is approximated by a piecewise con-

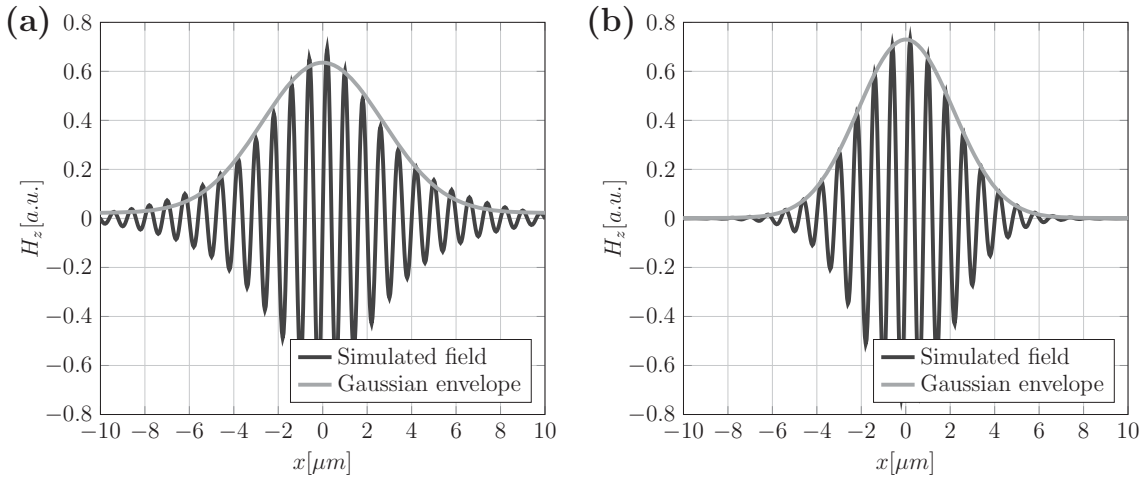


**Figure 5.8:** Field profiles with one (a) and five (b) interpolation steps. A Gaussian envelope is fitted to the simulated fields.

stant function. A schematic of the refractive index profile and the bleached photonic crystal waveguide is given in figure 5.7. For the numerical simulation the number of interpolation steps has been varied from one to five. The maximum refractive index change in the cladding was assumed to be 0.04. According to definition 4.2 this value corresponds to an effective change in the lattice constant of 2 nm.

The simulated field profiles for one and five interpolation steps are given in figure 5.8a and b respectively. The envelopes are fitted with a Gaussian function, which is depicted in green. For a single step the field profile deviates significantly from the Gaussian envelope, while for five interpolation steps a nearly perfect Gaussian envelope is obtained.

Figure 5.9 shows the simulated quality factors and the standard deviation of the Gaussian envelope fit for different numbers of interpolation steps. The simulations showed that  $\sigma$  decreases strongly from one to two steps. This explains why almost no improvement of the quality factor is observed from one to two interpolation steps. For more than two interpolation steps the  $\sigma$  value rises gently and the simulated quality factor increases by approximately 21% for each additional interpolation step. For five interpolation steps a quality factor of  $8.8 \cdot 10^5$  is simu-

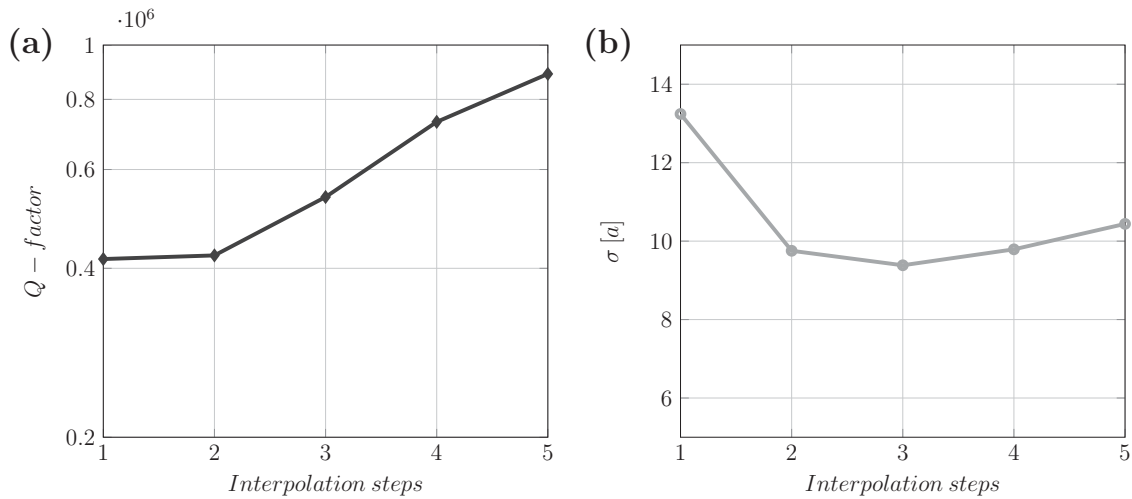


**Figure 5.9:** shows the quality factor (a) and standard deviation of the Gaussian envelope (b) for cavities with quadratic refractive index modulation as a function of number of interpolation steps.

lated, which is close to the highest quality factors realized for vertically symmetric glass infiltrated heterstructure cavities of  $1 \cdot 10^6$  [135].

In order to confirm the numerical results photonic crystal waveguides have been fabricated and coated with a 500 nm thick cladding of APC-CKL1 polymer cladding. After baking the transmission spectrum of the waveguides was recorded. Secondly the samples were bleached in accordance with the numerical simulations with five interpolation steps and a maximum refractive index change of 0.04.

Figure 5.10a shows light microscope images of a photonic crystal waveguide before and after bleaching. The graded change in the refractive index profile can be seen from the gradually changing color of the bleached section. The total length of the bleached section was 14 lattice constants. Figure 5.10b shows the measured transmission spectra before and after bleaching. The spectra have been low pass filtered to remove influences from endface reflections. A maximum quality factor of 8,570 was obtained for these experiments.

Compared to the numerical results presented in figure 5.9 the experimental quality factors are quite low. The most likely explanation for the low quality factors, also compared to the ones obtained for unslotted photonic crystal waveguides

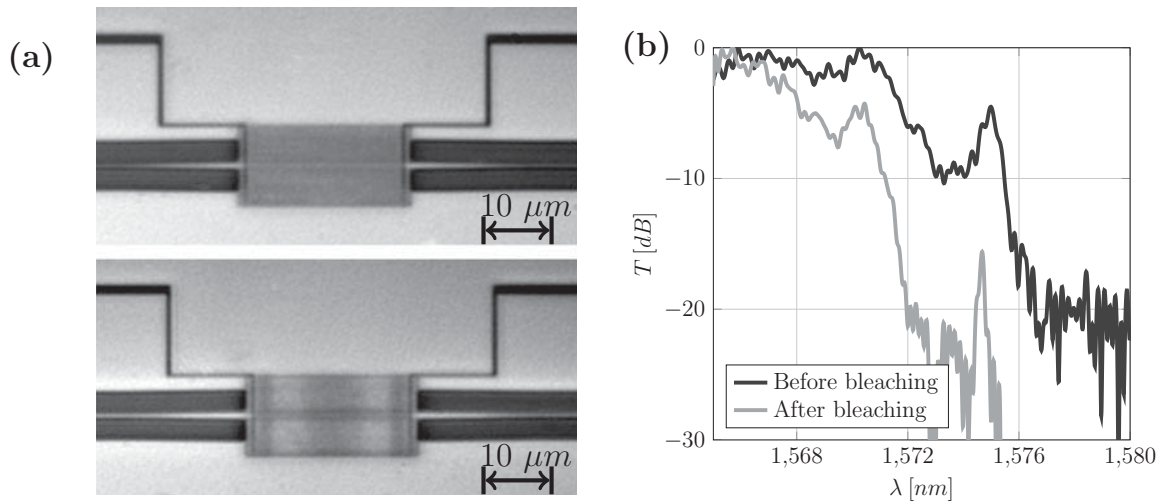


**Figure 5.10:** (a) shows light microscope images of the photonic crystal waveguide before and after bleaching. (b) shows the measured spectrum of a cavity with parabolic refractive index profile before and after bleaching.

in chapter 4, is increased scattering due to the presence of the slot. As noted in section 5.1 structures with stronger scattering require a larger mode gap. Since the maximum refractive index in this material is limited to 0.06 the effective lattice cannot be larger than 3 nm in this geometry. However, as this waveguide geometry was not optimized for refractive index sensitivity it is likely that larger mode gaps can be obtained for waveguides. In summary it can be said that the experimental results for bleached cavities with a parabolic refractive index distribution lag behind the expectations, however the numerical results show that Gaussian mode envelopes represent an interesting approach for obtaining cavities with very high quality factors.

### 5.3 Photonic Crystal Cavities with Raised Cosine Field Envelopes

It has been shown in the preceding section that the modification of the field envelope can be a powerful tool in order to control the vertical radiation and increase

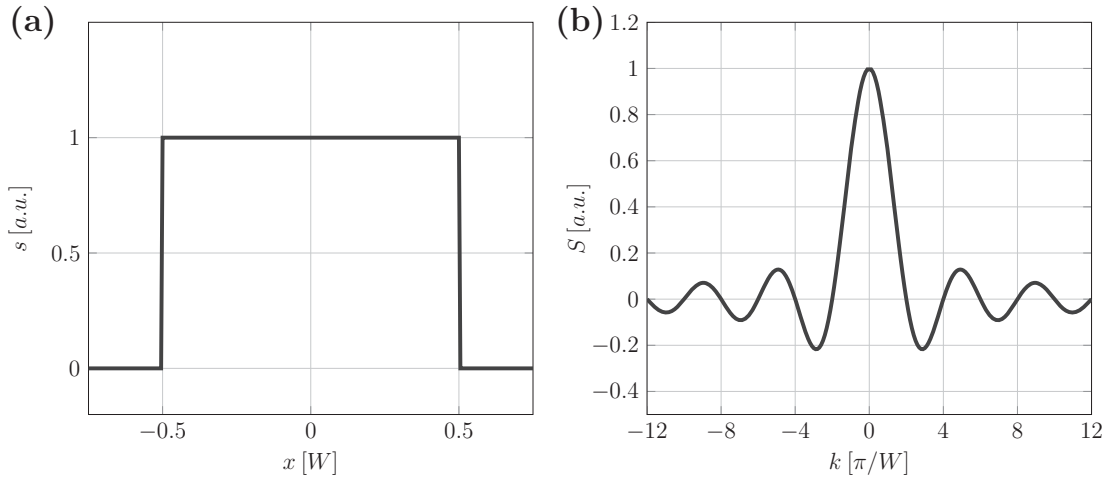


**Figure 5.11:** (a) shows a rectangle function and (b) its corresponding Fourier spectrum.

the quality factor in photonic crystal cavities. In this section raised cosine functions will be introduced as an alternative to Gaussian shaped field envelopes. It will be shown that, for a given mode volume, engineered raised cosine shaped field envelopes can in many cases lead to significantly higher quality factors compared to Gaussian envelopes.

Raised cosine functions are well known in digital signal processing, where their extraordinarily sharp spectra help to improve the frequency resolution and dynamic range of discrete Fourier transforms [136]. This property also makes them attractive as field envelopes in photonic crystal cavities. The idea behind raised cosine functions can be understood considering a rectangle function  $s(x, W)$  and its Fourier spectrum  $S(k, W)$  given by

$$s(x, W) = \frac{1}{W} \text{rect}\left(\frac{x}{W}\right) \quad \longleftrightarrow \quad S(k, W) = \text{sinc}\left(\frac{kW}{2}\right) \quad (5.13)$$

where the parameter  $W$  determines the width of the function. Figure 5.11 shows  $s(x, W)$  and the Fourier transform  $S(k, W)$ . The spectral energy is poorly confined and exhibits large side lobes. The first side lobe close to  $k = \pm 3\pi/W$  is as high as 23% amplitude of the main maximum. In order to reduce the side

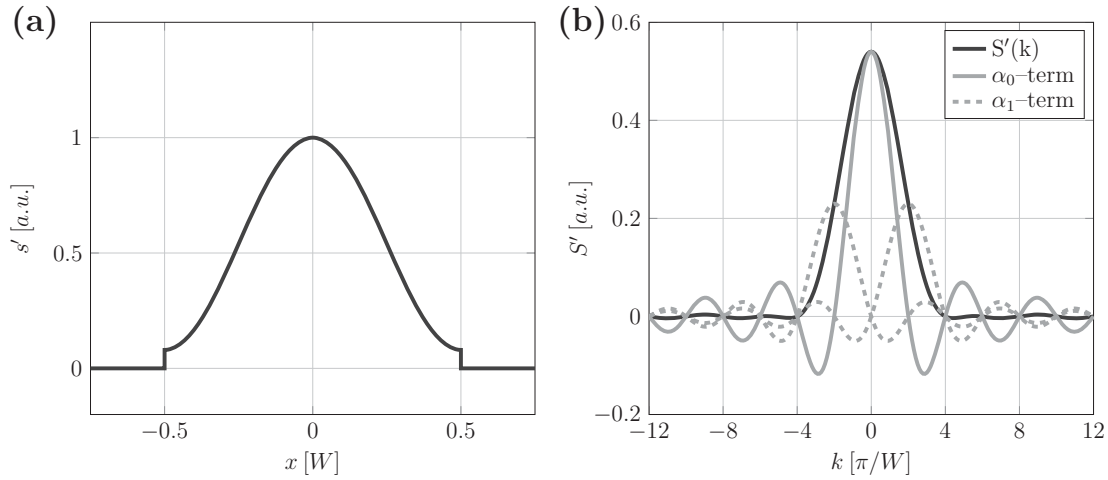


**Figure 5.12:** (a) shows the Hamming window and (b) its corresponding Fourier spectrum.

lobes and thereby improve the spectral confinement  $s(x, W)$  is multiplied with a harmonic function. Doing so a new function  $s'(x)$  is obtained with

$$s'(x) = s(x, W) \left( a_0 + a_1 \cos\left(\frac{2\pi}{W}x\right) \right) \quad \bullet \quad S'(k) = S(k) * \left( a_0 + \frac{a_1}{2} \left( \delta\left(k - \frac{2\pi}{W}\right) + \delta\left(k + \frac{2\pi}{W}\right) \right) \right) \quad (5.14)$$

where  $*$  denotes the convolution integral and  $\delta$  the Dirac delta function. Figure 5.12 shows the Hamming window  $s'(x)$  and its Fourier transform  $S'(k)$ , which is given by the coefficients  $a_0 = 0.54$  and  $a_1 = 0.46$  [137]. The coefficients of this particular raised cosine function have been chosen for optimum side lobe cancellation. Figure 5.12 shows that the central peak of  $S'(k)$  has widened as a result of the multiplication of the cosine term. Furthermore it can be seen that the different *sinc* functions interfere destructively, which leads to a strong suppression of the side lobes. For this raised cosine function the largest residual side lobe has an amplitude of 0.7% of the main peak. The side lobe suppression can be further improved by adding more cosine terms. The general raised cosine window  $\tilde{s}(x)$  of order  $N$  can then be written as

$$\tilde{s}(x) = s(x, W) \sum_{i=0}^N a_i \cos\left(\frac{2\pi i}{W} x\right) \quad \tilde{S}(k) = S(k) * \sum_{i=0}^N \frac{a_i}{2} \left( \delta\left(k - \frac{2\pi i}{W}\right) + \delta\left(k + \frac{2\pi i}{W}\right) \right), \quad (5.15)$$

which is very similar to the expression obtained for discrete time series in signal processing [138].

### 5.3.1 Synthesis of Raised Cosine Functions

As described for Gaussian functions a suitable field envelope should minimize the spectral energy for  $k$ -vectors inside the light cone. In order to meet this requirement the coefficients  $a_i$  are chosen such that the side lobes from  $N + 1$  till  $2N$  of  $s(x, W)$  are canceled optimally. This requirement can be written in a matrix form with

$$\begin{pmatrix} c_{11} & c_{12} & \dots & c_{1N} \\ c_{21} & c_{22} & \dots & c_{2N} \\ \vdots & \vdots & \ddots & \vdots \\ c_{1N} & c_{2N} & \dots & c_{NN} \end{pmatrix} \begin{pmatrix} a_1 \\ a_2 \\ \vdots \\ a_N \end{pmatrix} = a_0 \begin{pmatrix} S(k_{max,N+1}, W) \\ S(k_{max,N+2}, W) \\ \vdots \\ S(k_{max,2N}, W) \end{pmatrix} \quad (5.16)$$

where  $S(k_{max,i}, W)$  is amplitude of the  $i$ th side lobe of the *sinc* function  $S(x, W)$ . The matrix entries  $c_{mn}$  are given by

$$c_{mn} = (S(k_{max,N+m-n}, W) + S(k_{max,N+m+n}, W))(-1)^{(n+1)}. \quad (5.17)$$

Figure 5.13a shows raised cosine functions of different order, which were synthesized by means of equation 5.16. The functions and corresponding spectra were normalized to constant energy. The synthesized functions become narrower for larger function orders due to cosine terms with higher spatial frequencies. In figure 5.13b the corresponding Fourier spectra of the synthesized functions are shown. It can be seen that each additional coefficient reduces the residual side lobes by approximately 20 dB.

There are no fundamental limitations on how low the side lobes can become. Albrecht has shown a value of -289 dB for the highest side lobe using a raised cosine

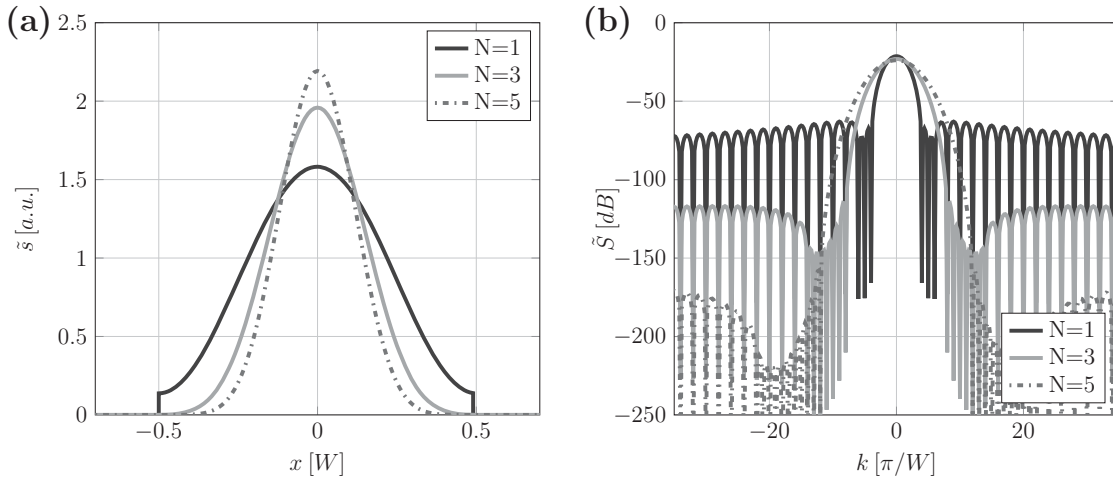


**Figure 5.13:** (a) shows raised cosine functions with rectangular boundary and (b) the corresponding spectra with different number of coefficients. Each additional coefficient reduces the side lobes by 20 dB.

function of order eleven [139]. For the photonic crystal resonators however, the highest applicable function order is constrained by the desired mode volume and the available  $k$ -space below the light cone. As can be seen in figure 5.12 the main maxima of the shifted *sinc* contributions are always located at zero intersections of all other *sinc* contributions. Hence, the main maxima of *sinc* contributions cannot be canceled by other *sinc* contributions. As a consequence all main maxima of the *sinc* functions must reside outside the light cone. This requirement defines the upper limit of the function order.

One complication using raised cosine functions as field envelopes for dielectric resonators is the fact that the synthesis given above relies crucially on the boundary condition given by the function  $s(x, W)$ . The rectangular boundary chosen before is not an ideal choice for field envelopes of photonic crystal cavities. In this case the electromagnetic field is forced to zero for  $|x| > W/2$ , which would require a very rapid decay of the electro-magnetic field. In order to account for a finite penetration depth of the electromagnetic field into dielectric reflectors exponential tails are therefore added to the rectangle function. The modified boundary condition is given by

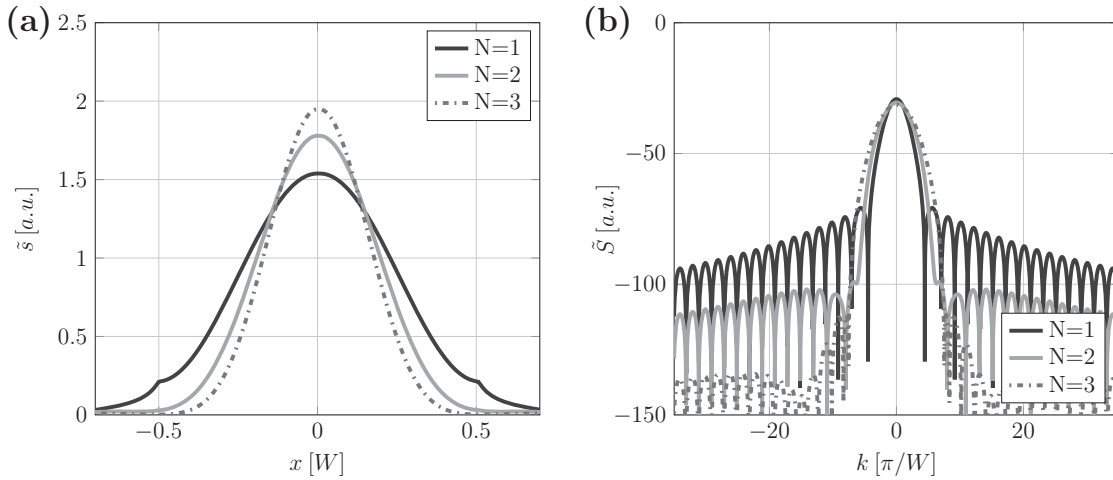


**Figure 5.14:** (a) shows raised cosine functions for a boundary with a finite decay constant of  $15/W$  and (b) corresponding spectra. In (a) the exponential tails are well visible for  $N = 1$ .

$$s(x, W) = \text{rect}(x/W) + u(x - W/2)e^{-\alpha(x-W/2)} + u(-(x - W/2))e^{\alpha(x-W/2)} \quad (5.18)$$

where  $u(x)$  is the Heaviside step function and  $\alpha$  is the decay constant. The corresponding k-vector distribution  $S(k, W)$  is given by

$$S(k, W) = \text{sinc}\left(\frac{Wk}{2}\right) + 2\left(\frac{\alpha}{\alpha^2 + k^2}\cos\left(\frac{Wk}{2}\right) - \frac{k}{\alpha^2 + k^2}\sin\left(\frac{Wk}{2}\right)\right). \quad (5.19)$$

Due to the exponential tails the Fourier spectrum is extended by two additional terms, which are proportional to  $\cos(\frac{Wk}{2})$  and  $\sin(\frac{Wk}{2})$ . These additional terms have two effects: They change the amplitude of the side lobes, which in turn changes the matrix elements  $c_{mn}$  in equation 5.16. Secondly the spacing of the side lobes is no longer periodic because the cosine term is not in phase with the  $\text{sinc}$  term and all terms decay with different rates as  $k$  grows larger. This leads to a slight dephasing of the shifted copies of  $S(k, W)$  in k-space as the distance to the centre maximum grows larger. As a consequence of the changing periodicity the extinction of the side lobes is no longer perfect.

In order to find the coefficients  $a_i$  for the case of finite penetration depth the position and amplitude of the side lobes is computed numerically. In the following a

moderate decay constant of  $\frac{15}{W}$  is assumed. Figure 5.14 shows the synthesized raised cosine functions for the modified boundary condition with exponential tails. The raised cosine functions have residual side lobes of similar magnitude as those for the rectangular boundary condition given in figure 5.13. Simulations showed that for the penetration depth chosen here no significant improvement of the extinction of the side lobes is observed for function orders larger than three. This is a direct consequence of the non optimal cancellation of side lobes due to the dephasing effect. Based on the given analysis however, an improvement for higher order functions is expected if larger values of  $\alpha$  are allowed.

For the sake of comparability the synthesized raised cosine functions are scaled to have the same effective widths  $\sigma$ . The effective width is defined by the root mean square criterion given by

$$\sigma = \sqrt{\frac{\int_{-\infty}^{\infty} \tilde{s}(x)^2 x^2 dx}{\int_{-\infty}^{\infty} \tilde{s}(x)^2 dx}} [140]. \quad (5.20)$$

The effective widths of the functions are brought into agreement by adjusting the parameter  $W$  for each function. The complete parameter set of the synthesized raised cosine functions is given in table 5.1.

In order to analyze how the synthesized functions perform as field envelopes the approach of Liu et al. is applied [141]. The field distribution  $H_z$  is modeled using a slowly varying envelope approximation given by

$$H_z(x) = \tilde{s}(x) \cos\left(\frac{\pi}{a}x\right) \circ \bullet \mathcal{F}\{H_z\} = \frac{1}{2}(\delta(k - \frac{\pi}{a}) + \delta(k + \frac{\pi}{a})) * \tilde{S}(k), \quad (5.21)$$

	$a_0$	$a_1$	$a_2$	$a_3$	W
$N = 1$	1.107	0.839			0.635
$N = 2$	0.841	0.950	0.143		0.853
$N = 3$	0.703	0.943	0.265	0.022	1.00

**Table 5.1:** Coefficients of raised cosine functions for a boundary with a finite decay constant of  $15/W$ .

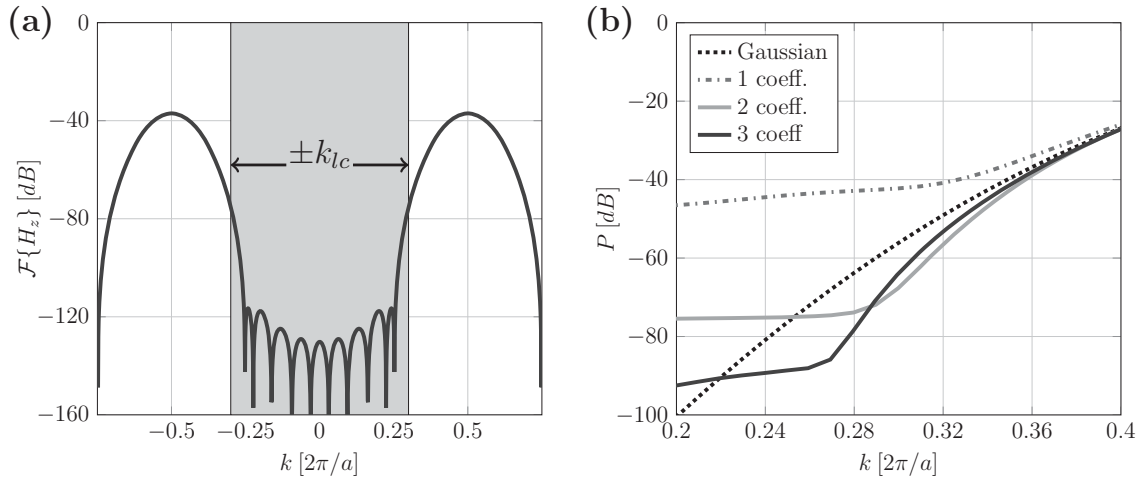


**Figure 5.15:** (a) shows the schematic of a numerical cavity spectrum. The integration domain is depicted by a gray shade. (b) shows the radiated power inside the light cone as a function of the integration boundary  $k_{lc}$ .

where  $a$  is the lattice constant of the photonic crystal and  $\tilde{S}(k)$  is the spectrum of the cavity field envelope. For the simulations presented here  $a$  was chosen to be  $16W$ . The spectral power coupled the light cone is calculated by integrating the spectral power between  $-k_{lc}$  and  $k_{lc}$  using equation 5.2. Figure 5.15a shows a schematic k-vector spectrum including the integration boundaries. Figure 5.15b shows the vertically radiated power versus the width of the light cone  $k_{lc}$  for the synthesized raised cosine functions from table 5.1 and a Gaussian function of the same effective width. For all functions the power increases monotonically as the integration boundary is moved towards  $k = \frac{\pi}{a}$ . For raised cosine envelopes with  $N = 2$  and  $N = 3$  a wide range exists where the radiated power is much lower as compared to a Gaussian envelope of the same width. In the maximum difference between the Gaussian envelope and the second and third order raised cosine envelopes are 12 dB and 18 dB respectively.

Provided that vertical radiation is the only loss path in the cavity  $P$  is inversely proportional to the cavity quality factor. Under this assumption the vertically radiated power and the quality factors for raised cosine envelopes and Gaussian envelopes can be related by

$$\frac{Q_{\text{Raised cosine}}}{Q_{\text{Gauss}}} = \frac{P_{\text{Gauss}}}{P_{\text{Raised cosine}}}. \quad (5.22)$$

The enhancement of the quality factor due to raised cosine field envelopes compared to a Gaussian field envelope of the same effective width can thus be up to a factor of 16 and 63 for the second and third order raised cosine function respectively. It should be noted that the choice the lattice constant  $a$  has little influence on the vertically radiated power at the point of maximum difference. Only the value of  $k_{lc}$  at which the maximum difference occurs is shifted.

### 5.3.2 Numerical Validation

The enhancement of the vertical quality factor due to raised cosine field envelopes can be confirmed by numerical simulations. The numerical model used in this case comprises of a set of infinitely extended alternating layers of air and silicon. The refractive index of silicon is assumed to be 3.5. The simulations were carried out in frequency domain using CST studio suite. The envelope of the resonant mode is shaped by a spatial variation of the silicon filling fraction, where the filling fraction is defined from zero to one for 0% to 100% material content. The filling fractions of the unperturbed photonic crystal are 0.47 and 0.53 for silicon and air respectively. Figure 5.16 shows the band diagram of the structure. The second mode is chosen to form the cavity since its dispersion is similar to that of photonic crystal defect waveguides shown in figure 5.6.

Before the cavities can be simulated the spatial variation of the silicon filling fraction needs to be computed that leads to the desired electro-magnetic field distribution. This is done by generalizing the synthesis approach presented for Gaussian functions. As long as the desired field envelope is symmetric and monotonously decaying from the centre the filling fraction of silicon  $f_{si}(x)$  can be approximated by

$$f_{si}(x) \approx f_0 - \frac{1}{\gamma D} \left( \frac{\ln(\tilde{s}(x))}{x} \right)^2 \quad (5.23)$$

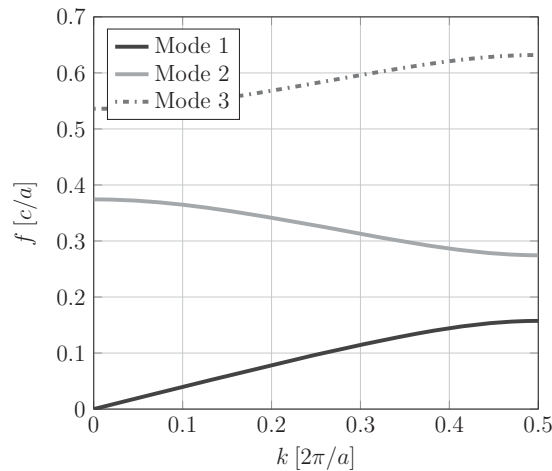


**Figure 5.16:** shows the band diagram of a one dimensional photonic crystal. The filling fractions of air and silicon are 53% and 47% respectively.

where  $\ln$  denotes the natural logarithm and  $f_0$  the filling fraction of the unperturbed photonic crystal. For the Gaussian function this equation yields the same parabolic dependence on the cut off frequency as given in equation 5.9.

For raised cosine functions that are oscillating in real space it was found that a better approximation to the desired envelope can be achieved by treating the local maxima of the envelope as coupled cavities. The functions are therefore split into segments at the local minima and the value of  $\frac{1}{D\gamma}$  was optimized for each segment. The different segments are then adjoined and simulated together. The local field maximum in each segment is fine tuned by introducing a small offset in the filling fraction.

Figure 5.17 shows the optimized distribution of the filling fraction and the corresponding the magnetic field profile profile for the third order raised cosine function from table 5.1. It can be seen that a good fit with the desired envelope function was achieved even for highly attenuated fields.

For comparison a Gaussian envelope with parabolic filling fraction of silicon was simulated. The  $\sigma$  of the Gaussian function was adjusted in such a way that the cavities with Gaussian and raised cosine envelope have the same effective width according to equation 5.20.

In a second step the infinitely extended layers were reduced to a slab maintaining the same spatial distribution of the filling fraction. The value of  $k_{lc}$  was

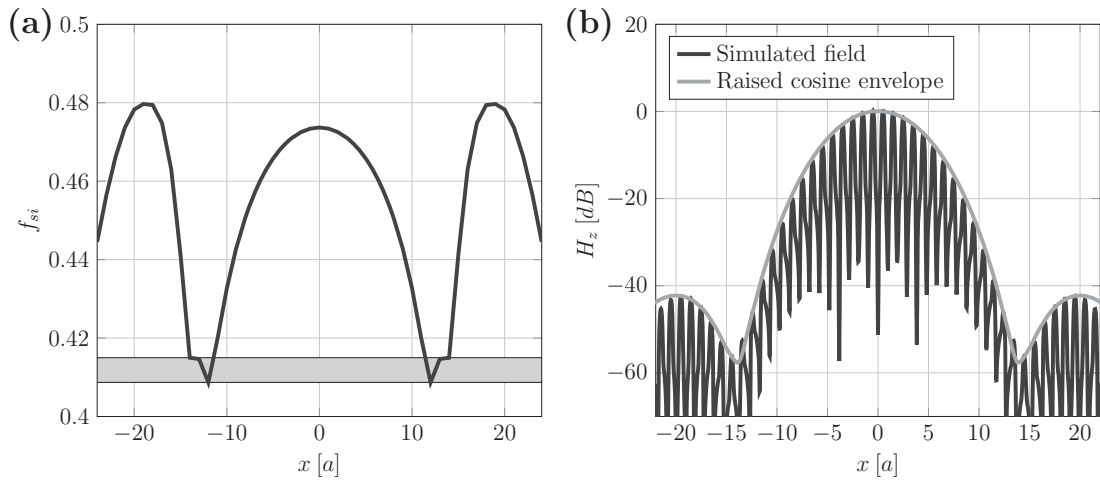


**Figure 5.17:** (a) shows the optimized spatial distribution of the silicon filling fraction. The offset between the two function segments is indicated by a grey shade. (b) shows the magnitude of the magnetic field in dB scale.

varied by changing the thickness of the slab, which in turn changed the resonance frequency of the cavity. The largest splitting between the Gaussian envelope and the optimized raised cosine envelope was found at a slab thickness of  $0.46a$ . At this slab thickness quality factors of  $33 \cdot 10^6$  and  $1.1 \cdot 10^6$  were obtained for the raised cosine and Gaussian envelope respectively. The simulated magnetic field distribution is depicted in figure 5.18. It can be seen that the vertical radiation is strongly suppressed in the case of the raised cosine mode envelope.

The numerically obtained ratio between the quality factor of the third order raised cosine envelope and the Gaussian envelope is smaller than anticipated by the analytic calculations. Possible reasons for this might lie in approximations, which enter equation 5.1. Also small deformations in the raised cosine envelope cannot be completely excluded since the values of  $\frac{1}{D\gamma}$  and the segment offsets for the filling fraction have been optimized manually.

Despite the approximations made in the analytic model, the simulations confirm the expectation of enhanced quality factor due to optimized raised cosine mode envelopes. Having established both the analytic and numerical methods it could be worthwhile to investigate other window functions like Kaiser-Bessel or

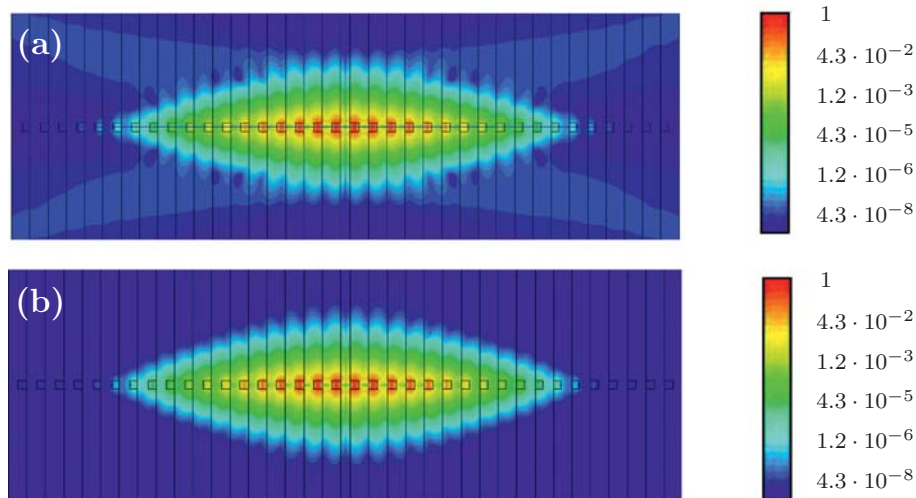


**Figure 5.18:** (a) shows the magnetic field intensity of a cavity with Gaussian envelope. (b) shows the magnetic field intensity of a cavity with raised cosine envelope. The fields are normalized to the maximum field value. It can be seen that the vertical scattering is much stronger in the case of the Gaussian envelope.

Dolph-Chebyshev windows for their potential as mode envelopes [142, 143]. In particular the problem of dephasing could be circumvented by choosing another type of function. Like for Gaussian mode envelopes the full potential of this approach can only be realized by means of a fabrication method, which allows to define small geometry changes in a reliable way. Post processing methods such as bleaching therefore represent interesting tools to experimentally investigate the influence of different spatial mode profiles on the quality factor.

In summary it can be said that for a proper choice of the waveguide geometry and centre defect length even single step heterostructure cavities are sufficient to obtain intrinsic quality factors above  $10^5$ . If higher quality factors are desired then cavities with Gaussian mode envelopes can be used. One possible way to fabricate cavities with a Gaussian shaped field envelope is to define a parabolic variation of the local cladding refractive index by bleaching. It could be shown numerically that the quality factor increases exponentially for an increasing number of refractive index steps. The highest quality factor simulated was  $8.8 \cdot 10^5$ . The largest



quality factor found experimentally was 8,570. None of the shown structures require an undercutting of the photonic crystal membrane, which greatly facilitates the fabrication process. Finally, even higher quality factors can be obtained by using a raised cosine shaped field envelope instead of a Gaussian envelope. For the chosen parameters it could be shown numerically that the quality factor in cavities with raised cosine envelopes can be enhanced by another factor of 30 compared to Gaussian field envelopes.



## Chapter 6

# Electro-Optic Modulation in Hybrid Silicon-Organic Waveguide Structures

This chapter discusses the methods and experiments to characterize electro-optically modulated silicon waveguide structures. Experimental results as well as parts of the text in subsection 6.3 have been published in [67].

In chapter 5 different methods were discussed in order to obtain photonic crystal cavities with high quality factors. In this chapter it will be experimentally shown how compact electro-optic amplitude modulators can be realized by taking advantage of both resonant and non-resonant photonic crystal waveguides.

One key aspect for efficient electro-optic modulation in polymer infiltrated silicon waveguides is a high electro-optic coefficient  $r_{33}$ . In order to optimize the poling procedure for high values of  $r_{33}$  slotted waveguides have been investigated. Compared to photonic crystal waveguides or cavities slotted waveguides are less challenging to fabricate and the experimental results are easier to interpret.

Furthermore this chapter will provide methods to interpret electro-optic measurements in photonic crystal waveguides. Using these methods electro-optic mod-

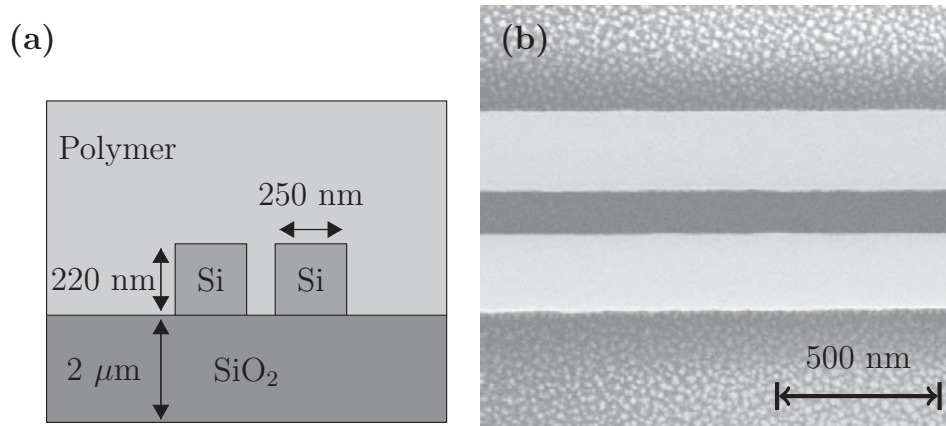


**Figure 6.1:** (a) shows a schematic cross section of a slotted waveguide with dimensions. (b) shows a SEM image of a slotted waveguide. The grey bars are the waveguide rails.

ulation in a photonic crystal cavity at kHz frequencies will be shown. Finally electro-optic modulation in a photonic crystal waveguide at 40 GHz modulation frequency is demonstrated.

## 6.1 Electro-Optic Phase Modulation in Slotted Waveguides

The slotted waveguides used here are similar to the waveguides presented in [21] however, the structure parameters have been adapted for the purpose of this study. A schematic cross section as well as a scanning electron microscope image are given in figure 6.1. The silicon rail height was kept constant at 220 nm. The rail width has been optimized using the CST mode solver in order to obtain a high refractive index sensitivity  $\frac{d\beta}{dn}$  inside the slot. For a slot width  $w_{slot} = 100$  nm an optimal refractive index sensitivity of  $1.36 \cdot 10^6/\text{m}$  is found for a rail width of 250 nm. The slotted waveguides have been fabricated in lengths between 100  $\mu\text{m}$  and 400  $\mu\text{m}$ .

The waveguides were infiltrated by drop casting with a solution of APC-CKL1 in cyclopentanone. Afterwards the samples were placed into an evacuated oven at 90 °C for 12 hours to remove residual solvents. The samples were poled under

nitrogen atmosphere on a temperature controlled hot plate. The temperature was increased at a rate of 10 °C/min until the final temperature was reached. The sample was then kept at this temperature for a defined dwell time and subsequently cooled down to room temperature. The poling field remained applied during the whole temperature cycle. The poling field  $E_p$  is defined as

$$E_p = \frac{V_p}{w_{slot}} \quad (6.1)$$

where  $V_p$  is the voltage applied to the sample. For the electro-optic characterization the slotted waveguides are contacted by wafer probes. As a voltage is applied to the probes an electric field forms between the two silicon rails, which induces a change in propagation constant given by

$$\Delta\beta = \frac{d\beta}{dn} \Delta n_{eo} \quad (6.2)$$

where  $\Delta n_{eo}$  is the electro-optically induced refractive index change. Inserting Pockels formula from equation 2.20 for  $\Delta n_{eo}$  and multiplying by the slotted waveguide length  $L_{wg}$  gives the electro-optically induced change in the waveguide transmission phase

$$\delta\Phi = \frac{1}{2} \frac{d\beta}{dn} n^3 r_{33} \frac{V}{w_{slot}} L_{wg}. \quad (6.3)$$

The electro-optic phase change  $\delta\Phi$  in the waveguide is then measured in a Mach-Zehnder interferometer. Figure 6.2 shows a schematic of the setup. A fiber coupled tunable laser source is used as excitation. The polarization of the laser beam is controlled via a fiber based polarization controller. Collimator lenses are used to couple the light from fibers into free space. The beam path is split by a beam splitter. The light in the sample path is coupled into the waveguide via microscope objectives. The two beam paths are reunited at the second beam splitter and coupled back into a fiber, which is connected to a photodiode.

The transmitted intensity through the interferometer is given by

$$I(\Phi) = \frac{I_{max}}{2} (1 + \cos(\Phi)) + I_0 \quad (6.4)$$

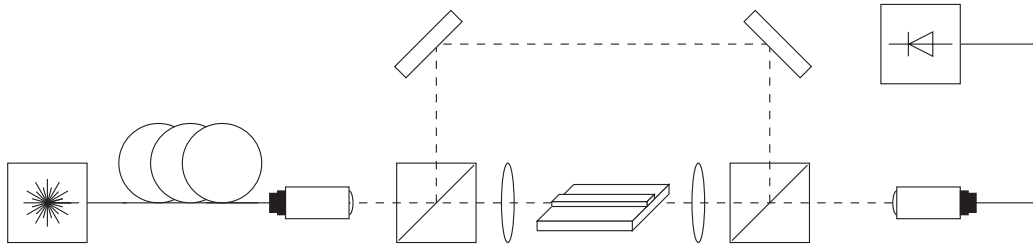


**Figure 6.2:** Shows a schematic of the Mach-Zehnder interferometer used to characterize polymer infiltrated slotted waveguides. Fibers and beams in free space are depicted as bold and dashed lines respectively.

where  $\Phi$  defines the operating point of the interferometer,  $I_{max}$  is the maximum intensity and  $I_0$  is an offset resulting from unbalanced transmission through the two interferometer arms. The change in transmission intensity  $\delta I$  due to a small electro-optic phase shift  $\delta\Phi$  can then be written as

$$\delta I = \delta\Phi \frac{dI}{d\Phi} = \tilde{I} \sin(\Phi). \quad (6.5)$$

Figure 6.4 shows a schematic response of an electro-optically modulated interferometer. The constants  $I_{max}$  and  $\tilde{I}$  are obtained by measuring the transmission through the interferometer and the electro-optically induced change in transmission intensity for different values of  $\Phi$ . Figure 6.3 shows a schematic of the interferometer response. Substituting  $\delta\Phi$  in equation 6.5 by equation 6.3 gives an expression that can be solved for the electro-optic coefficient  $r_{33}$  in the slotted waveguide

$$r_{33} = \frac{4\tilde{I}w_{slot}}{I_{max} \frac{d\beta}{dn} V L_{wg}}. \quad (6.6)$$

In order to increase the sensitivity of the setup a lock in amplifier is used to apply a sinusoidal electric signal  $V$  of one kHz frequency to the waveguide. This results in an electro-optically induced change in waveguide transmission phase, which follows the frequency of the lock in amplifier. The phase  $\Phi$  between the reference and the sample beam is adjusted via the wavelength of the laser. This

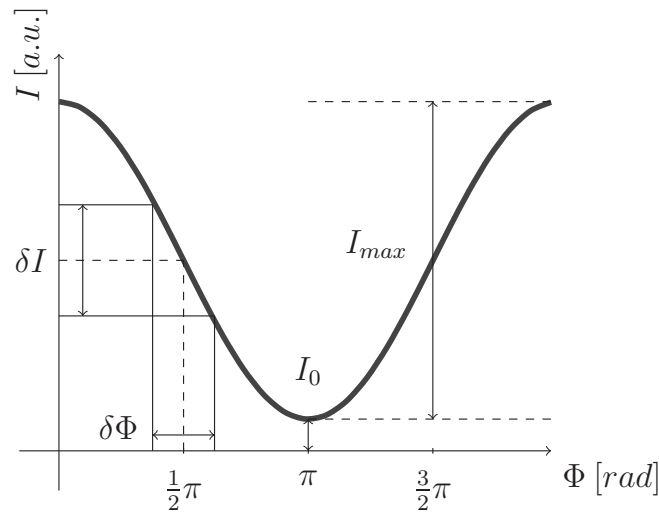


**Figure 6.3:** shows a schematic response of a Mach Zehnder interferometer

approach is valid since neither the electro-optic coefficient nor the waveguide dispersion vary significantly in the wavelength interval of the measurement.

Figure 6.4 shows a measurement of a slotted waveguide with a length of  $100 \mu\text{m}$ . The waveguide had been poled at  $200 \text{ V}/\mu\text{m}$ . The detected lock in signal  $\delta I$  and the DC photodiode signal  $I$  are 90 degree phase shifted as expected from the equations 6.4 and 6.5. The highest electro-optic coefficient in slotted waveguide samples was found for a poling field of  $300 \text{ V}/\mu\text{m}$ , a poling temperature of  $150^\circ\text{C}$  and a dwell time of 20 seconds. For these parameters a  $r_{33}$  of  $25 \text{ pm}/\text{V}$  was obtained. However, values above  $20 \text{ pm}/\text{V}$  have also been observed  $150 \text{ V}/\mu\text{m}$  and  $200 \text{ V}/\mu\text{m}$ . The fact that for some devices it is possible to apply poling fields of  $300 \text{ V}/\mu\text{m}$  and more to the electro-optic polymer without observing any dielectric breakdown is noteworthy itself. In thin films of thicknesses of  $1 \mu\text{m}$  or more dielectric breakdown is frequently observed for poling fields that are larger than  $100 \text{ V}/\mu\text{m}$ . This is most likely a consequence of the smaller poled polymer volume in slotted waveguides, which reduces the probability of defects inside the high field region.

Since the largest electro-optic coefficients measured in the slotted waveguides are about a factor of four lower than in a thin film of  $800 \text{ nm}$  thickness on ITO coated glass substrates the orientation of the chromophore molecules is expected

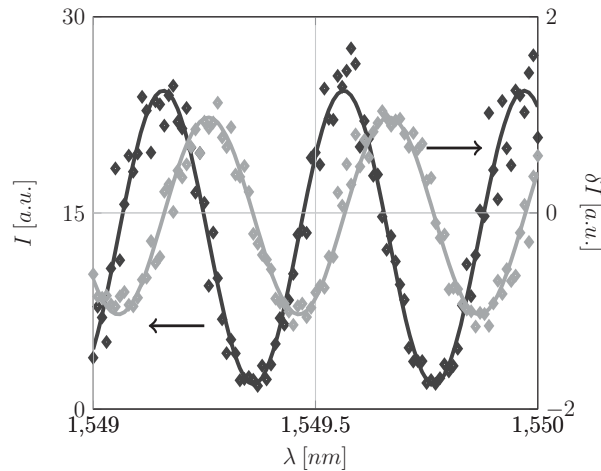


**Figure 6.4:** shows a measurement of a slotted waveguide of  $100 \mu\text{m}$  length. The sample has been modulated by a sinusoidal signal of five volt amplitude and one kHz frequency.  $I$  and  $\delta I$  denote the DC photodiode signal and the lock in signal respectively. Measured points are indicated by markers and the solid lines were obtained from a sinusoidal fit.

to be weak. In such a case it would be expected that the electro-optic coefficient increases linearly with the applied poling field. However, experimentally no clear field dependence is observed for poling fields between  $150 \text{ V}/\mu\text{m}$  and  $300 \text{ V}/\mu\text{m}$ . A possible explanation for this might be the presence of a current induced chromophore decay, which limits the electro-optic coefficient inside the slot. Poling induced chromophore decay has previously been observed in PMMA-DR1 [144].

Even though the electro-optic coefficients obtained in slotted waveguides are low compared to thin film values a significant improvement of the in device  $r_{33}$  was achieved in this study. The electro-optic coefficient reported here is approximately two times larger than the previously reported values for slotted waveguides of similar geometry [66, 67, 30, 68]. It should be mentioned at this point that for the high field strengths used in the experiments only a few samples exhibited comparatively high electro-optic coefficients. From nine samples poled at field strengths between 150 and  $300 \text{ V}/\mu\text{m}$  three showed an  $r_{33}$  above  $20 \text{ pm}/\text{V}$ . Three samples showed no measurable electro-optic effect. Another three samples showed very low electro-optic coefficients below  $5 \text{ pm}/\text{V}$ .

A major challenge of this study laid in the low currents during poling of the slotted waveguide samples. The currents were too low to be monitored reliably and thus it was often not possible to judge if a sample had been poled properly. In summary it can be said that poling fields between 150 and 200 V/ $\mu\text{m}$  and dwell times below two minutes at a temperature of 148.5 °C yield close to optimal electro-optic coefficients in slotted waveguides. However, for these parameters the probability for failure appears to be considerable.

## 6.2 Electro-Optic Amplitude Modulation in Photonic Crystal Cavities

The analysis presented in chapter 5 has shown that optimized single defect heterostructures can easily reach the desired Q-factors of 8000, even for a vertically asymmetric cladding. For the experimental realization slotted photonic crystal cavities with a single defect in the centre of the cavity have been fabricated. The waveguide parameters are the same as introduced in section 5.1. A defect length of two lattice constants was chosen in order to benefit from the delocalization of the resonant mode. In figure 6.5 the scanning electron image of the fabricated photonic crystal heterostructure is given.

The samples have been coated with APC-CKL1 and baked the same way as the slotted waveguides before. Figure 6.6 shows the transmission spectrum of a photonic crystal heterostructure before poling. A pronounced resonance peak is observed at 1,550.2 nm. The peak is fit to a Lorentzian function  $L(\lambda)$  with

$$L(\lambda) = L_{max} \frac{\Gamma^2}{4((\lambda - \lambda_0)^2 + (0.5\Gamma)^2)} \quad (6.7)$$

where  $\Gamma$  is the full width half maximum value of the function and  $\lambda_0$  is the resonance wavelength of the cavity.  $L_{max}$  is the maximum value of  $L(\lambda)$ . The value for  $\Gamma$  obtained by the fit is 210 pm, which corresponds to a quality factor of 7,450, close to the desired value of 8,000. The deviation from the Lorentzian fit towards lower wavelengths can be explained by the vicinity of the transmission band edge.

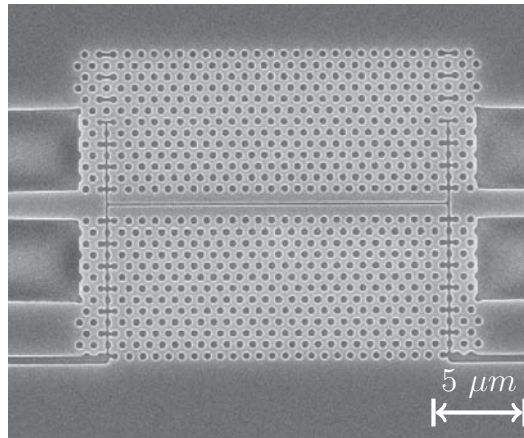


**Figure 6.5:** shows a SEM image of a slotted photonic crystal cavity before infiltration.

The cavity has been poled at moderate electric fields of  $100 \text{ V}/\mu\text{m}$  in order to reduce the probability of a dielectric breakdown. After the poling step the transmission spectrum was measured again. Figure 6.7 shows the measured transmission spectrum before and after poling. It can be seen that the cavity resonance is shifted to shorter wavelengths after poling. This is surprising because it was expected that due to the poling step the chromophore molecules orient along the the direction of the poling field. This in turn should lead to an increase of the refractive index in the direction of poling due to the uniaxial oriented state and due to the positive anisotropy of the molecular polarizability. Since the optic electric field inside the slot is parallel to the direction of poling the increased refractive index should shift the cavity resonance to longer wavelengths. Also the quality factor is reduced to a value of 3,300. Besides the saturation of the  $r_{33}$  value in slotted waveguides this observation serves as further evidence for chromophore decay inside the slotted waveguide during the poling step.

For the electro-optic characterization the transmission spectrum of the sample was recorded by means of a tunable laser source. At the same time the sample was modulated using a lock-in amplifier and the wavelength dependent electro-optic amplitude modulation was recorded. The measured spectrum after poling and the corresponding lock in signal are given in figure 6.8.

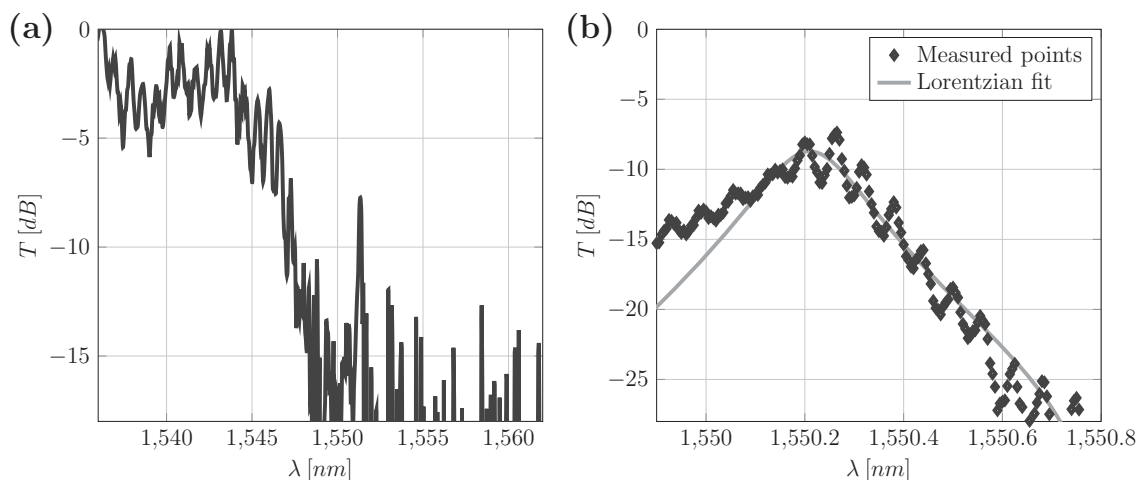


**Figure 6.6:** shows the measurement of a slotted photonic crystal cavity. (a) has been measured using a broad band source and an optical spectrum analyzer. (b) has been measured using a tunable laser source in order to increase the resolution of the spectrum.

The electro-optic effect inside the slot leads to a change in refractive index  $\Delta n_{eo}$ , which in turn leads to a shift in the cavity resonance wavelength by  $\Delta\lambda$  given by

$$\Delta\lambda = \frac{d\lambda}{dn} \Delta n_{eo} \quad (6.8)$$

where  $\frac{d\lambda}{dn}$  determines the sensitivity of the resonator towards refractive index changes inside the slot. For a 100 nm wide slot a sensitivity of 112 nm has been calculated from eigenmode simulations of the photonic crystal waveguide. Provided that the electro-optically induced refractive index shift is sufficiently small the resonance wavelength change of the the cavity is given by

$$\frac{dL(\lambda)}{d\lambda} \Delta\lambda = -L_{max} \frac{8(\lambda - \lambda_0)\Gamma^2}{\pi(4(\lambda - \lambda_0)^2 + \Gamma^2)^2} \Delta\lambda. \quad (6.9)$$

Equation 6.9 reaches its maximum value at  $\lambda_{mod,max} = \lambda_0 \pm \frac{\Gamma}{2\sqrt{3}}$ . The wavelength shift can be obtained from the following expression

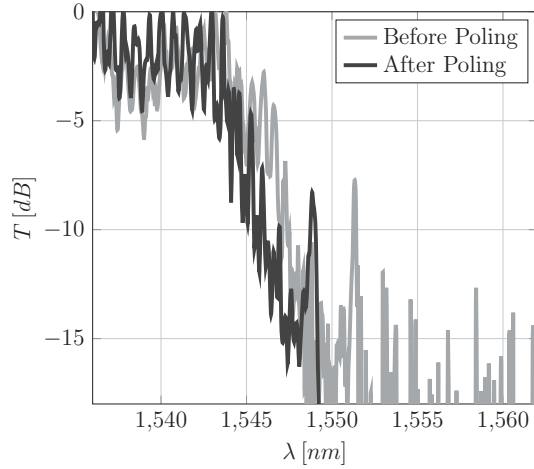


**Figure 6.7:** shows transmission spectra of a photonic crystal cavity before and after the poling step.

$$\left. \frac{dL(\lambda)}{d\lambda} \right|_{\lambda_{mod,max}} \frac{\Delta\lambda}{L(\lambda_0)} = -\Delta\lambda \frac{3\sqrt{3}}{4\Gamma} \quad (6.10)$$

Figure 6.8 shows the transmission spectrum and the measured modulation in the poled cavity for a modulation amplitude of 5 V. Using equation 6.10 a resonance frequency shift of 38 pm is obtained, which corresponds to a refractive index change of  $3.4 \cdot 10^{-4}$ . Using Pockels formula and equation 6.8 an electro-optic coefficient of 3.1 pm/V inside the slot is calculated for this sample. One possible explanation for the very low electro-optic effect in the sample could be that the electrical contact was interrupted during poling. However, as for slotted waveguides, the poling current was too low to confirm this hypothesis.

### 6.3 Electro-Optic Modulation at GHz Frequencies

In this section electro-optic modulation at GHz frequencies in a photonic crystal waveguide will be demonstrated. The waveguide parameters are the same as in the previous section, except for a slightly increased slot width of 150 nm.

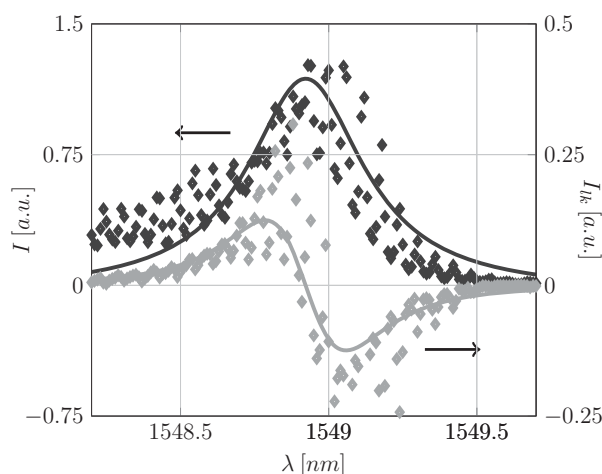


**Figure 6.8:** shows the transmission and electro-optic modulation signal of photonic crystal cavity. Measured points are indicated by markers and the solid lines have been obtained from a Lorentzian fit.

As for photonic crystal cavities the transmission spectrum can be shifted in wavelength by an electro-optically induced refractive index change inside the slot. In agreement with equation 6.9 the change in transmission  $\Delta T$  due to the electro-optic effect can be written as

$$\Delta T = \frac{dT}{d\lambda} \frac{d\lambda}{dn} \Delta n \quad (6.11)$$

where  $T$  is an arbitrarily shaped transmission spectrum. It can be seen from equation 6.11 that, like for cavities, the modulation is proportional to the slope of the spectrum. As discussed in chapter 4 the transmission drops rapidly at the waveguide mode cut off leading to a large slope in the transmission spectrum. This means that the mode cut off can be used for electro-optic modulation like the photonic crystal cavities shown before. Since the slot width for the photonic crystals waveguides in this section is increased from 100 nm to 150 nm the refractive index sensitivity inside the slot  $\frac{d\lambda}{dn}$  is slightly increased to a value of 120 nm.

The silicon slab was p-doped by ion implantation of Boron to a concentration of  $10^{18}/cm^3$  reducing the specific resistance to  $0.03 \Omega cm$ . The reduced resistance is necessary to enable a charging time of the slot capacitance of 10 ps, permitting

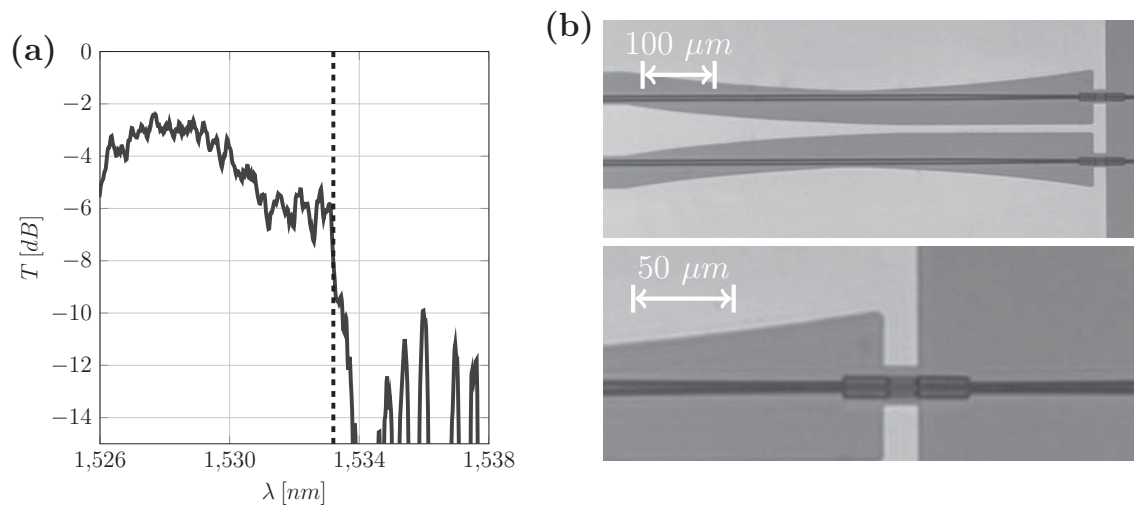


**Figure 6.9:** (a) shows the transmission spectrum of the photonic crystal waveguide. The modulation wavelength is indicated by a dashed line. (b) shows light microscope images of the photonic crystal waveguide and the RF electrodes.

modulation speeds up to 100 GHz, as proposed in [119]. A 150 nm gold film was deposited using electron beam evaporation. The electrical contact pads and radio frequency feeding lines were structured through photolithography and potassium iodide iodine etch. Light microscope images of the structured electrodes are given in figure 6.9b.

After the electrodes had been structured the samples were infiltrated with APC-CKL1 and baked as described for the slotted waveguide experiments. The sample was poled with a maximum temperature of 145 °C while applying 20 volts to the electrodes, resulting in a poling field in the slot of approximately 130 V/μm. After reaching the maximum temperature the sample was rapidly cooled down to room temperature.

The transmission properties of the devices were characterized using a broadband source of 1,525 to 1,605 nm optical bandwidth and an optical spectrum analyzer. The transmission spectrum of a slotted PhC waveguide device is displayed in figure 6.9. The transmission edge of the defect mode is located near 1533 nm wavelength.

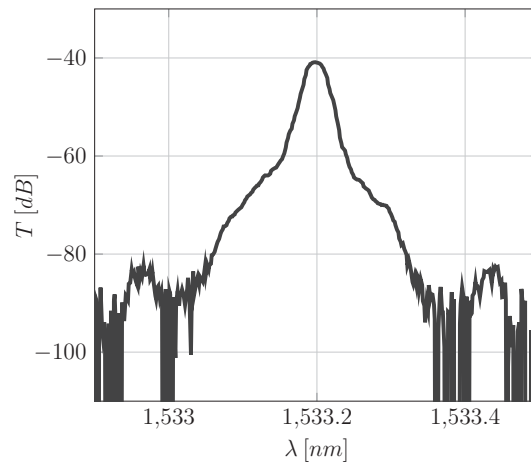


**Figure 6.10:** shows the spectrum of the optical carrier, which has been modulated at 30 GHz.

The response to high frequency modulation was measured by monitoring the side bands in the optical spectrum of a narrow band laser source. The laser, which serves as optical carrier, is amplitude modulated with a sinusoidal signal and hence the optical spectrum consists of a main peak for the carrier and two side peaks equally spaced around the carrier. The spectral distance from side to main peak is equal to the modulation frequency [145]. For the modulation experiment the carrier was tuned to 1,533.2 nm wavelength, closely at the transition region from optical pass band to stop band, where the slope of the transmission curve is steep. The output signal was detected and spectrally scanned with high resolution around the carrier wavelength using an optical spectrum analyzer. A measurement taken for 30 GHz modulation frequency is given in figure 6.10.

Optical spectra have been recorded using modulation frequencies of 15, 20, 30, and 40 GHz. For ease of interpretation the modulated carrier spectrum is plotted versus frequency and the carrier has been relocated to the origin. The readings are presented in figure 6.11. All traces show symmetric sidebands left and right from the optical carrier. The frequency offset between the carrier and the side bands matches with the modulation frequency. The experiment was repeated for samples in which the polymer had not been poled. In this case no side bands were observed, proving that the modulation is indeed due to the electro-optic response of the polymer in the slot.

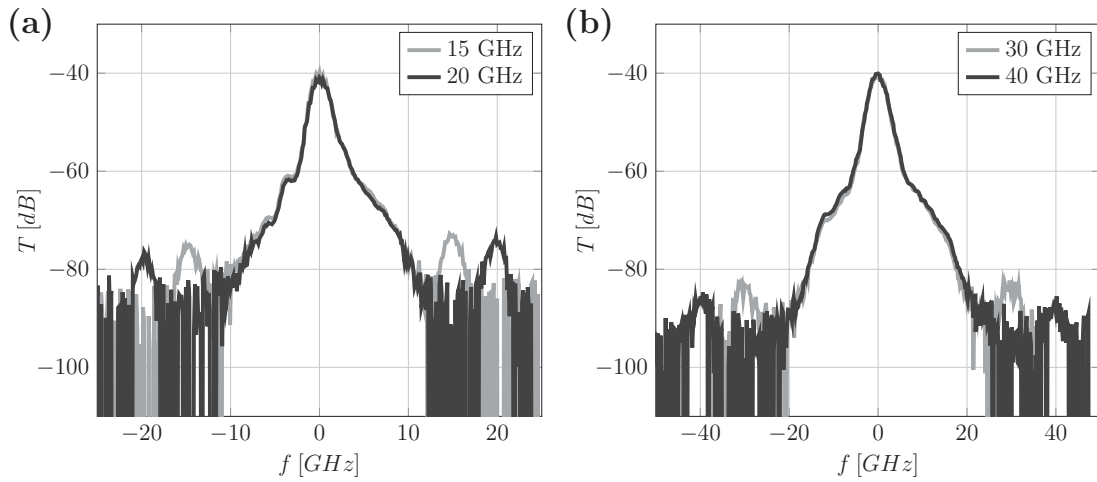


**Figure 6.11:** shows the optical carrier, which has been modulated at (a) 15 and 20 GHz and (b) 30 and 40 GHz respectively.

At 15 and 20 GHz modulation frequency the radio frequency (RF) power delivered to the chip, including insertion losses from the cable and wafer probe, is approximately 13 dBm. From numerical simulations the modulation voltage drop at the slot corresponding to this input power is calculated to be 1.4 V<sub>pp</sub>. From the slope of the transmission spectrum at the carrier frequency, together with the side band to carrier power ratio, a spectral shift of approximately 40 pm is obtained.

The drop in side band power with increasing frequency can be attributed to the combined effect of reduced output power of the RF source as well as increased insertion loss from the feeding cable and wafer probe, which is estimated to be 6 dB. Additionally, a shift in the transmission spectrum was observed, most likely due to thermal drift, which decreased the slope of the transmission curve at the probing wavelength. The combined effects lead to the observed drop in side band power of approximately 10 dB.

The in-device Pockels coefficient can be calculated from the transmission spectrum using equation 6.11 and Pockels formula in equation 2.20. For the presented device a Pockels coefficient of 12 pm/V is found for the electro-optic polymer inside the slot.

In summary, the experiments presented in this chapter show that careful optimization of the poling process can significantly increase the in-device electro-optic coefficient. Nevertheless, the obtained values for  $r_{33}$  are still several times lower than those found in thin films on ITO coated glass substrates. Based on the theoretic analysis in chapter 5 photonic crystal cavities were fabricated, which showed a sufficiently high quality factor for efficient electro-optic modulation. Electro-optic amplitude modulation photonic crystal cavities and waveguides was demonstrated. The measurements seem to indicate that partial chromophore decay is taking place during the high field poling. However, a direct proof for this is difficult to obtain due to the small geometry of the slotted waveguide.

In addition to the electro-optic experiments at kHz frequencies electro-optic modulation up to 40 GHz has been demonstrated in slotted photonic crystal waveguides. The modulation frequency was limited only by the available RF source and power feeding scheme. A significant roll off in the modulation signal amplitude up to this value was not observed, indicating that operation at even higher bandwidths should be feasible.



## Chapter 7

# Electrical and Nonlinear Characterization of Polymer Thin Films on Silicon Substrate

In this chapter the physical effects, which lead to current flow during the poling step are analyzed in a thin film geometry. The electro-optic coefficients of the thin films are determined using a modified Teng-Man method, which allows to measure both electro-optic coefficients in a single measurement. The results on the modified Teng-Man method in section 7.1 and parts of the analysis on conduction mechanisms have been published in [146] and [147] respectively

As described in chapter 6 the poor poling efficiency remains a major challenge in hybrid silicon organic waveguide systems. In order to find ways to improve the poling efficiency it is essential to understand the mechanisms that contribute to the electrical current during poling. It has been noted that excessive current flow during the poling process is detrimental for a high electro-optic coefficient [63, 148].

The conduction mechanisms in electro-optic polymers during poling have been studied by several groups. For a variety of electrode and polymer materials it was

consistently found that current density for moderate poling fields scales exponentially with the square root of the applied field [149, 150, 64]. For PMMA-DR1 Blum et al. were able to prove that this current voltage behavior is explained by lowering of the charge injection barrier due to the Schottky effect [47].

For higher fields the current voltage characteristics deviate from the thermionic emission behavior. Blum et al. found that for PMMA-DR1 on ITO coated glass the current voltage behavior can be described by Fowler-Nordheim tunneling [47]. In the tunneling regime the current is exponentially dependent on the applied electric field and thus increases significantly faster than in the thermionic emission regime. Sprave et al. showed that once the current enters the tunneling regime the probability for a dielectric breakdown event increases strongly, which limits the maximum applicable poling field [149].

In contrast Huang et al. applied a combined model of thermionic emission and space charge limited current for films from APC-CKL1 on ITO coated glass substrates [64]. They argued that space charge limited current is detrimental to the poling behavior because a space charge inside the polymer leads to electric field screening and to a locally reduced poling efficiency.

Previous works have stressed the importance of the polymer electrode interface for the obtained electro-optic coefficients [64, 151, 149]. However, silicon electrodes have not been investigated yet. As pointed out in chapter 6 studying the mechanisms of the current flow in slotted waveguides is challenging since the area through which the current flows is very small. Also the complex geometry of a slotted waveguide poses an experimental challenge. Effects from surface roughness or field enhancements at edges cannot be easily taken into account.

In order to overcome these experimental challenges the current conduction and the electro-optic coefficient in nonlinear polymers are studied in thin films on silicon substrate. In contrast to slotted waveguides the preparation of polymer thin films is simple and highly reproducible. Furthermore the low number of surface defects on the silicon substrate is advantageous for identifying the physical principles, which govern the poling current and limit the poling efficiency.

The poled thin films on silicon substrate are characterized electro-optically using a modified Teng-Man experiment, which allows to obtain both electro-optic coefficients in a single measurement.

## 7.1 Electro-Optic Characterization of Thin Films on Silicon Substrate

Several methods are known to measure the electro-optic coefficients in thin films. Attenuated total internal reflection using TE- and TM-polarizations is one of the standard methods to measure both electro-optic coefficients. However, this method only works if the substrate refractive index is lower than that of the electro-optic film, which is unsuitable for silicon substrates [152]. Another way of assessing the electro-optic coefficients is by interferometry. Both Mach-Zehnder and Michelson interferometers have been used to measure the electro-optic coefficients [153, 154, 155] but multiple reflections inside the sample are not considered in the equations, which is not valid for a highly reflective substrate such as silicon. Park et al. have provided an analytic model to account for multiple reflections in interferometric experiments, however the strong wavelength dependence due to multiple reflections in the substrate remain an experimental challenge for silicon substrates [156].

Fabry-Perot resonators have also been presented for measuring the electro-optic coefficients [157, 158, 159]. However, this method only works accurately if the polymer layer is sufficiently thick to support at least one resonance. This drawback could be overcome following the proposal of O'Brian et al. who are used the bottom interface of the substrate as a second reflective interface for transmission measurements [160].

The most widely used method to characterize electro-optic thin films is the Teng-Man method [65]. It is an ellipsometric method, which works by monitoring the electro-optic response as a function of varying input polarization. This method has the drawback that only one electro-optic coefficient can be obtained while the ratio between the two coefficients must be assumed. For poled electro-optical polymers employing rod-like molecules and at lower poling field strengths this ratio is close to three. The Teng-Man method is applied to low index contrast materials

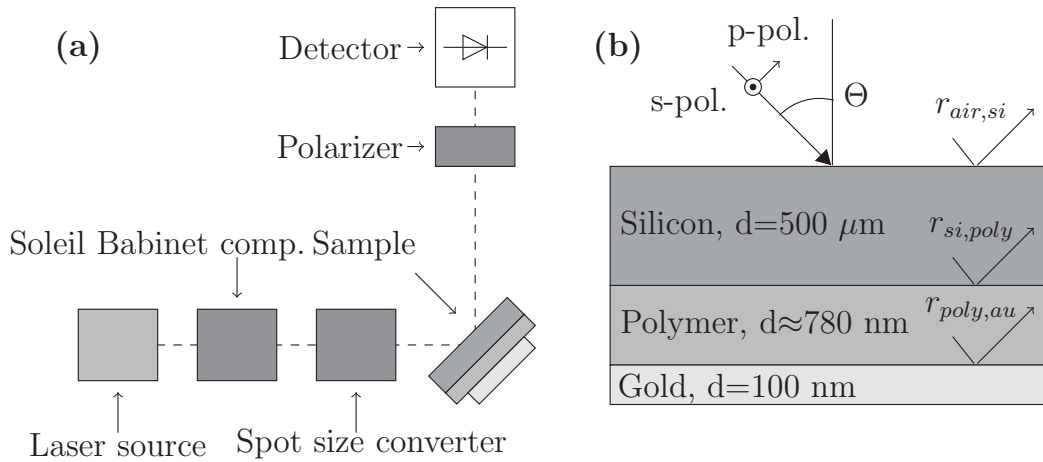


**Figure 7.1:** (a) shows a schematic of the experimental setup. (b) shows a schematic of the sample including the relevant reflections and layer thicknesses. The direction of the electric field for the corresponding polarization is given.

and does not take into account multiple reflections. Park et al. have shown how to correct for errors due to multiple reflections in Teng-Man experiments [161]. In this section it is demonstrated how a Fabry-Perot resonator formed by a high refractive index substrate can be used in a Teng-Man experiment to measure both  $r_{33}$  and  $r_{13}$  without the necessity of an additional setup. In this case, a wavelength scan is done to obtain these values. Compared to previous experiments on Fabry-Perot resonators the presented approach works in reflection and does not require semitransparent mirrors or auxiliary conductive layers. This simplifies the sample preparation and increases the experimental reproducibility.

Figure 7.1a shows a schematic of the experimental setup. The largest part of the setup is equivalent to the original setup proposed by Teng and Man [65]. In addition to the original setup a beam size converter was placed between the Soleil Babinet compensator and the sample to reduce diameter of the beam to 0.5 mm. As light source an Agilent 8164 A tunable laser source was used. All experiments have been carried out at an incident angle of  $45^\circ$  to the sample normal.

Figure 7.1b shows a schematic of the sample including points of reflection and layer thicknesses. The given multilayer structure of the sample was analyzed following the approach of Park et al. [161]. Assuming that the incident light on

the sample can be approximated by a plane wave the reflection coefficient  $r_i$  at each layer  $i$  can be written as Airy function with

$$r_i = \frac{r_{i-1,i} + r_{i,i+1} e^{2j\beta_i d_i}}{1 + r_{i-1,i} r_{i,i+1} e^{2j\beta_i d_i}} \quad (7.1)$$

where  $r_{i-1,i}$  is Fresnel reflection coefficients between layer  $i-1$  and  $i$ ,  $r_{i,i+1}$  is the reflection coefficient between layer  $i$  and  $i+1$ ,  $d_i$  is the thickness of the layer and  $\beta_i$  is the normal wave number given by

$$\beta_i = k_0 n_i \cos(\Theta_i) \quad (7.2)$$

where  $k_0$ ,  $n$  and  $\Theta_i$  are the propagation constant of the wave in air, the refractive index and the incidence angle of light in the layer respectively. For the experiments presented in this chapter three layers are to be taken into account: The silicon substrate, the polymer thin film and the gold layer. The gold layer is assumed to be sufficiently thick such that no multiple reflections occur inside the gold film. From these assumptions the following expression is obtained:

$$r = \frac{r_{air,si} + \frac{r_{poly,si} + r_{poly,au} e^{2j\beta_{poly} d_{poly}}}{1 + r_{poly,si} r_{poly,au} e^{2j\beta_{poly} d_{poly}}} e^{2j\beta_{si} d_{si}}}{1 + r_{air,si} \frac{r_{poly,si} + r_{poly,au} e^{2j\beta_{poly} d_{poly}}}{1 + r_{poly,si} r_{poly,au} e^{2j\beta_{poly} d_{poly}}} e^{2j\beta_{si} d_{si}}} \quad (7.3)$$

with  $r_{air,si}$ ,  $r_{si,poly}$  and  $r_{poly,au}$  represent the reflection coefficients at the air-silicon interface, the silicon polymer interface and the polymer gold interface respectively as depicted in figure 7.1b. Each reflection coefficient in equation 7.3 is polarization dependent given by the Fresnel equations. As the absorption losses in the sample are small the magnitude of  $r$  is close to unity. The phase of  $r$  however, is strongly wavelength and polarization dependent.

By poling the polymer film the chromophore molecules are oriented normal to the substrate plane. If afterwards a modulating electric field is applied to the poled polymer film a change of the refractive index is induced into the film. The refractive index change parallel and normal to the modulating field  $\Delta n_o$  and  $\Delta n_e$  are given by the Pockels formula introduced in section 2.2.2. In order to apply the Pockels formula it is necessary to know the ordinary and extraordinary refractive

index of the polymer after poling. Values for the poling induced birefringence for APC-CKL1 are not reported. However, for other guest-host systems poled at 100 V/ $\mu\text{m}$  poling field a poling induced birefringence of  $2 \cdot 10^{-2}$  has been found [154]. Neglecting the birefringence in this case would lead to errors in the calculated electro-optic coefficients below 5 %. Therefore in the experimental part of this section poling induced birefringence is neglected and the bulk refractive index of 1.63 is used for both polarizations. Nevertheless, if the birefringence is known, the effects of birefringence can be taken into account by calculating  $n_i$  for the p-polarization by means of the extraordinary and ordinary indices of the uniaxial poled polymer medium. The refractive indices of silicon and gold have been set to 3.5 and  $0.44+9.1j$  respectively with  $j$  as the complex unit [162, 163].

From figure 7.1 it can be seen that the s-polarization is only affected by  $\Delta n_o$  while the p-polarization is affected by both by  $\Delta n_o$  and  $\Delta n_e$ . The change in the refractive index translates into a change in reflection phase of  $r_s$  and  $r_p$ .

The Teng-Man experiment allows measuring the difference of these electro-optically induced phase shifts in s-and the p-polarization. As described in Park et al. the electro-optic phase shift scales with the derivative of the reflection phase  $\Psi$  with respect to the polymer refractive index [161]. Figure 7.2 shows  $\frac{\delta\Psi}{\delta n}$  for s-and p-polarization. Figure 7.2 shows that the electro-optic phase shift has a strong wavelength dependence, which originates from Fabry-Perot resonances inside the silicon substrate. It can also be seen that the finesse of the resonator is higher in s-polarization since the reflectivity of the substrate is larger than for the p-polarization. Simulations show that due to this fact both electro-optic coefficients can still be measured for film thicknesses below 150 nm. This is an important aspect since the slot widths in silicon waveguides are usually between 100 nm and 200 nm wide. It should be noted that instead of varying the wavelength it would also be possible to vary the angle of incidence. Experimentally however it is advantageous to vary the wavelength in order to avoid unnecessary alignment after each step.

In order to demonstrate this method thin films of APC-CKL1 were fabricated. The polymer blend has been dissolved in cyclopentanone with 8% wt. concentra-

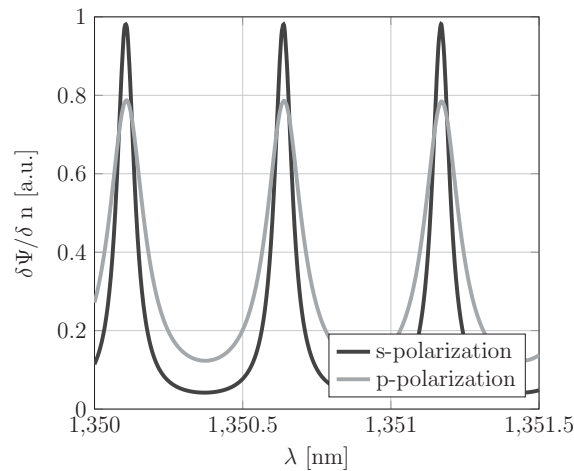


**Figure 7.2:** shows the simulated derivative of the reflection phase  $\Psi$  towards refractive index changes in the polymer layer for both *s*- and *p*-polarization. The polymer film thickness in this case was assumed to be 780 nm.

tion. The solution has been spin coated at 2,000 rpm on a double polished n-doped wafer of 500  $\mu\text{m}$  thickness and 10  $\Omega\text{cm}$  conductivity. The measured film thickness was between 760 and 820 nm for all samples. Afterwards the samples were baked and gold pads of 100 nm thickness were thermally evaporated onto the sample.

After measuring the film thickness the samples were poled at different field strengths. For the poling procedure an electric field was applied between the silicon substrate and the gold pad. The samples were heated to a final temperature of 145  $^{\circ}\text{C}$  at a rate of 10  $^{\circ}\text{C}/\text{min}$ . The samples remained at the final temperature for 60 seconds and were cooled down immediately afterwards. The field remained applied during the whole temperature ramp. The poling procedure was carried out in nitrogen atmosphere.

After poling the samples were placed into the Teng-Man setup and measured. Figure 7.3a shows the photodiode signal as well as the electro-optic modulation signal. The modulation signal was recorded at a frequency of 1 kHz. No change in the modulation amplitude was observed between 100 Hz and 10 kHz indicating that there is no significant voltage drop over the silicon substrate at the modulation frequency of 1 kHz. The sample was modulated with an electric signal of 5 V amplitude and had a polymer thickness of 815 nm. On the horizontal axis the

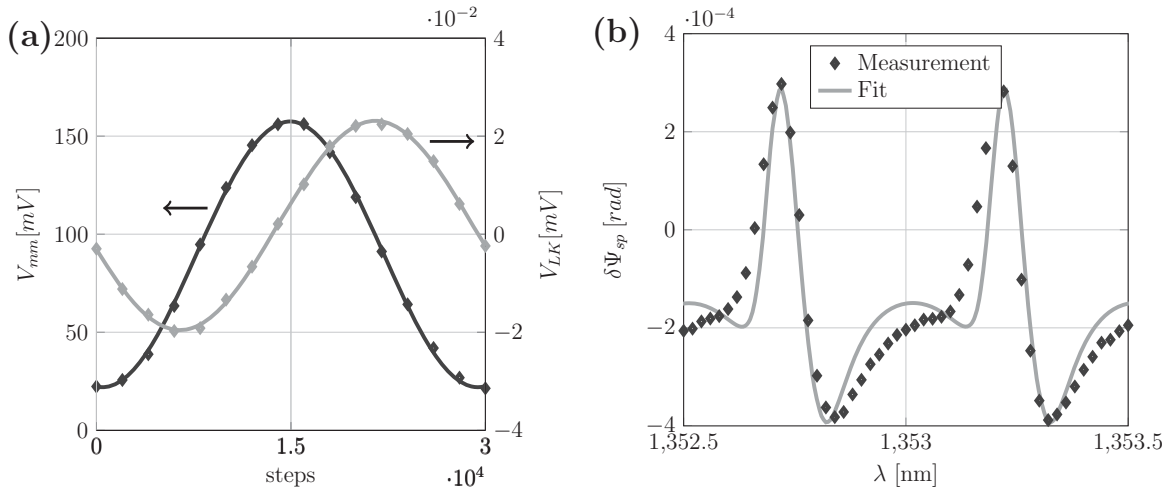


**Figure 7.3:** Shows the measurements obtained from a sample poled with an electric field of 61 V/m. The measured points are indicated by markers. Fitted functions are indicated by bold lines. In figure (a) the reading of the photodiode and the modulations signal from the lock in amplifier at 1,352.72 nm wavelength are given. Figure (b) shows the difference in electro-optic phase shift between s and p polarization as a function of wavelength.

step size of the Soleil Babinet compensator, which defines the state of polarization of the incident light. On the vertical axis the reflected intensity as expressed as photodiode output voltage  $V_{mm}$  and the electro-optic modulation signal  $V_{LK}$  are given. The electro-optically induced phase shift between s-and p-polarization can be obtained by

$$\delta\Psi_{sp} = \text{Imag}\left(\frac{\tilde{V}_{LK}}{\tilde{V}_{mm}}\right) \quad (7.4)$$

where  $\tilde{V}_{LK}$  and  $\tilde{V}_{mm}$  are the complex phasors of the harmonic functions  $V_{mm}$  and  $V_{LK}$ . Figure 7.3b shows the phase shift  $\delta\Psi_{sp}$  obtained for this sample at different wavelengths. The sharp peak towards positive phase shifts corresponds to a resonance inside the substrate in s-polarization. The dips towards negative phase shifts correspond to a resonance in p-polarization. The resonance in p-polarization is much broader since the reflection at the substrate interfaces is lower for the p-polarization.

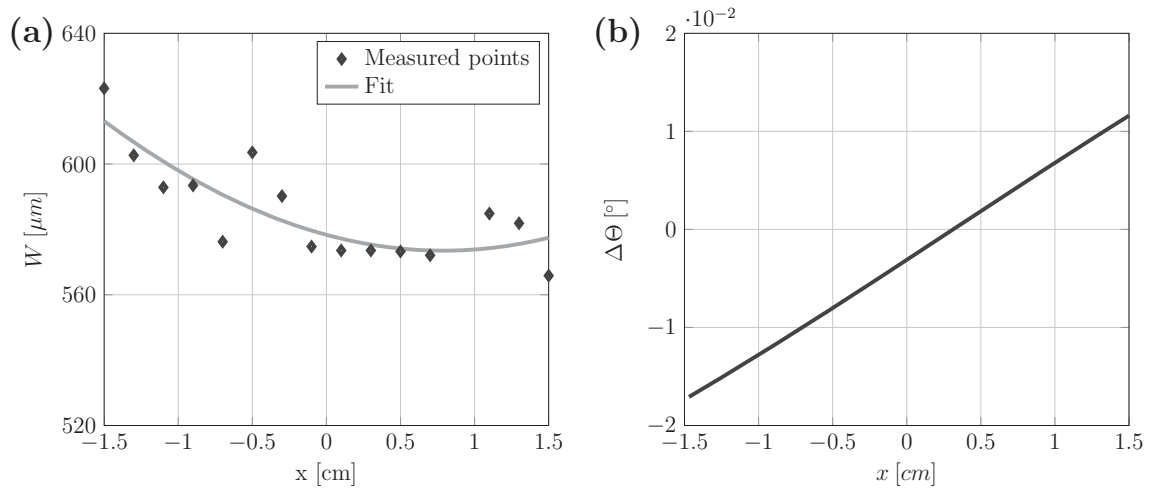


**Figure 7.4:** (a) shows the 20/80 beam width of the probing laser. Measured points and the fit function are depicted as diamonds and green line respectively. The sample resides at  $x=0$ . (b) shows divergence angle of the beam calculated from the fit in (a).

It was found that compared to the ideal model the experimentally obtained spectral features are slightly smoothed out. Possible reasons for this are the beam divergence of the probing laser and the line width of the laser. In order to determine the beam divergence a knife edge measurement was performed in the setup. Figure 7.4 shows the obtained beam profile and the corresponding divergence angle of the beam. From this measurement a beam divergence of  $0.003^\circ$  was found. A detailed description of the knife edge measurement can be found in appendix A. The beam divergence found in the knife edge measurement is about a factor of ten too small to account for the smoothing observed in the electro-optic measurements. Measurements of the laser line width show that the line width is also too small to explain the smoothing.

Since source incoherence and beam divergence can be ruled out as explanations for the smoothing of the measurements the broadening is attributed to an inhomogeneous polymer film thickness. The thickness of each sample has been measured at ten different positions around the gold pad using a Dektak surface profilometer. From these measurements the mean thickness  $d_{poly}$  and thickness

variance  $\sigma$  are estimated. A Gaussian thickness variation is incorporated in the model by simulating the electro-optic response of the multistack for several closely spaced thicknesses that are weighted by a Gaussian function and integrated. The smoothed electro-optic response is therefore given by

$$\delta\bar{\Psi}_{sp}(\lambda) = \frac{\Delta d_{poly}}{\sigma\sqrt{2\pi}} \sum_{i=-N}^N \delta\Psi_{sp}(\lambda, d_{poly} + i\Delta d_{poly}) e^{-\frac{(i\Delta d_{poly})^2}{2\sigma^2}} \quad (7.5)$$

where  $\Delta d_{poly}$  was chosen to be 1 nm, well below  $\sigma$  and N was chosen to be  $\text{round}(2/\Delta d)$ .

The electro-optic coefficients are obtained from the model in a sequential fitting procedure of the s- and p-peaks in the electro-optic phase shift. As the substrate represents a Fabry-Perot resonator of high order the matching of the absolute peak wavelengths with the model would require very precise knowledge of the incidence angle and the substrate thickness. However, absolute wavelength matching is not required in order to calculate the electro-optic coefficients. Figure 7.3b shows that the shape of the electro-optic phase shift is nearly periodic with the free spectral range. Thus small changes in the substrate thickness have negligible impact on the peak shape. Therefore offsets in the peak positions between simulation and experiment have been accounted for by introducing a small correction of the substrate thickness in the analytic model.

The mean film thickness is kept constant during the fitting. The thickness variance is set to the value estimated from the thickness measurements. Furthermore the ratio of  $r_{33}$  and  $r_{13}$  is assumed to be three leaving only  $r_{33}$  as free parameter for the first fitting step. Next the  $r_{33}$  is set such that the average electro-optic phase shift in the model and in the experiment are the same. The average phase shift is calculated by taking the mean value of the phase shift  $\delta\Psi_{sp}$  for one free spectral range of the Fabry-Perot resonator.

Using these values as a starting point for the fit the width of the peaks can be adjusted by changing the thickness variance in the model. Finally the height of the peaks for s- and p-polarization is fit by adjusting the values for  $r_{33}$  and  $r_{13}$  manually while keeping the average phase shift constant. Following this procedure a close to optimal fit of the data in figure 7.3b is found for a Gaussian distribution

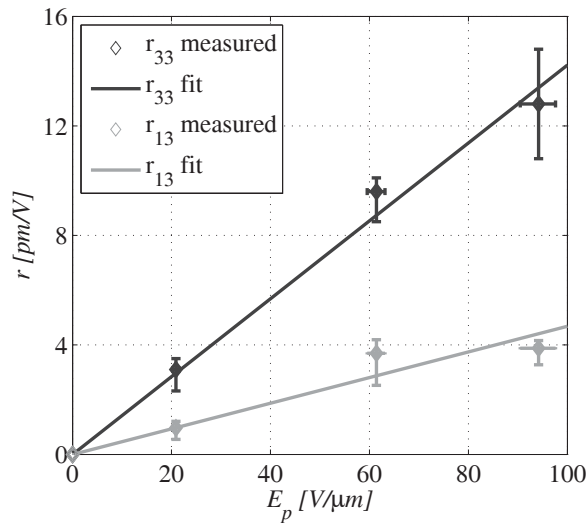


**Figure 7.5:** shows the measured electro-optic coefficients for samples poled at different electric fields. Both  $r_{33}$  and  $r_{13}$  scale approximately linear with the applied poling field. The ratio between the two line slopes is 3.0, which agrees well with the value of 3 predicted for a poled film with weak chromophore alignment.

of film thicknesses with a sigma of 27 nm, which is close to the estimated sigma of 24 nm obtained from the thickness measurements. For comparison a trace of a perfectly flat polymer film is depicted by a dashed line. For this sample we obtain values of 9.6 pm/V and 2.6 pm/V for the  $r_{33}$  and  $r_{13}$  coefficient respectively.

Several samples that had been poled with different field strengths have been measured. The electro-optic coefficients are fit individually for the thicknesses  $d_{poly} - \sigma$ ,  $d_{poly}$  and  $d_{poly} + \sigma$ . The uncertainty in the film thickness acts both on the applied poling and modulation field as well as on the fitted value for the electro-optic coefficients, which is reflected in the error bars in both horizontal and vertical direction. The obtained values for  $r_{33}$  and  $r_{13}$  as a function of the poling field are given in figure 7.5. It can be seen that both  $r_{33}$  and  $r_{13}$  are linearly dependent on the applied poling field. However, the achieved electro-optical coefficients are six times lower than thin films of comparable thickness on ITO substrates. These values are comparable to those found in slotted silicon waveguides. The ratio

between  $r_{33}$  and  $r_{13}$  obtained from the fit is 3.0, which is close to the value of 3 predicted from the free gas model [45]. However, the uncertainty of the film thickness limits the accuracy of the experimentally found ratio between  $r_{33}$  and  $r_{13}$ . More samples would thus be required in order to find possible deviations from the free gas model.

## 7.2 High Field Poling of Thin Polymer Films of APC-CKL1

The low electro-optic coefficients obtained in thin films on silicon substrate indicate that the geometric constraints present in slotted waveguides cannot fully explain the low in-device electro-optic coefficients. It is therefore manifest that the electronic properties of the silicon substrate play a key role for the high field poling process of electro-optic polymers. In this section the conduction mechanisms in thin films of APC-CKL1 during high field poling are investigated. The results are complemented by measurements of the electro-optic coefficients and the interplay between current conduction during poling, electronic properties of the substrate and the obtained electro-optic coefficients is discussed.

### 7.2.1 Conduction Mechanisms in Thin Films of APC-CKL1

It has been shown earlier by Sprave et al. that the current conduction during high field poling has big impact on the attainable electro-optic coefficients [149]. Based on current-voltage measurements they were able to identify the physical effects that govern the charge transport during high field poling and develop methods to enhance the electro-optic coefficients. In order to compare the current conduction mechanisms during high field poling on silicon substrate and ITO coated glass substrates the approach used by Huang and Sprave was followed [149, 64]. Thin films polymer films of 800 nm thickness of have been spin coated on double polished silicon substrates and ITO coated glass substrates. Two different types of silicon substrate were used: Untreated silicon substrate and silicon coated with a

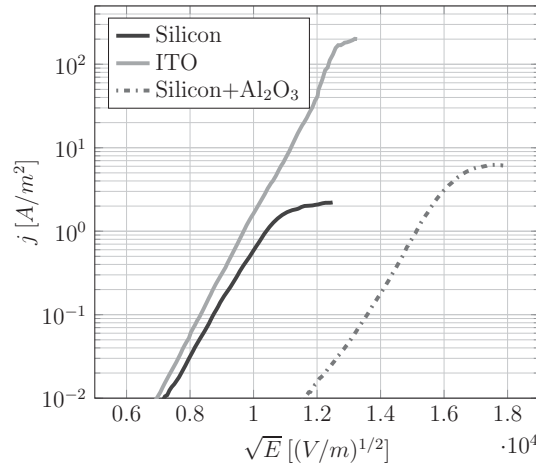


**Figure 7.6:** shows current-voltage curves of 800 nm thin films of APC-CKL1 on different substrates at a temperature of 140 °C. The substrates are biased positively.

5 nm layer of aluminum oxide. The silicon substrates had the same dopant and doping level as those used in the preceding section. The aluminium oxide was deposited using atomic layer deposition (ALD) [164]. The reaction cycle involved two steps using trimethylaluminium and water as precursors. 45 deposition cycles were carried out at a deposition temperature of 200 °C. After the polymer deposition the samples have been baked and gold electrodes of 100 nm thickness have been thermally evaporated on the polymer film.

Figure 7.6 shows the current-voltage relation of APC-CKL1 thin films on different substrates in the Schottky representation. The raw data from figure 7.6 has been provided by M.Sc. Marvin Schulz and is used with his permission. The samples were measured at a temperature of 140 °C, close to the glass transition temperature of the polymer. Previous works have shown that the current conduction is mainly determined by the hole injecting interface [165]. Therefore the silicon and ITO substrates are biased positively. Two different regimes for current conduction can be identified. For low applied fields the current density can be written as

$$j \propto e^{c\sqrt{E}} \quad (7.6)$$

where  $c$  is a constant defining the slope in the Schottky plot. For larger fields the current enters a different regime in which the current obeys a power law with

$$j \propto E^\gamma \quad (7.7)$$

and  $\gamma < 1$ . The resulting current-voltage relation in this regime is sub-ohmic. In the following this regime will be called the saturated current regime. A sub-ohmic dependence between current and voltage has been shown experimentally for several different dielectric and electrode combination [166, 167, 168]. Often this type of current conduction is described like a reverse biased pn or metal–semiconductor junction. The current then follows the Shockley equation with

$$j(V) = j_0(e^{V/kT} - 1) \quad (7.8)$$

where  $V$  is the voltage applied to the junction and  $j_0$  is the saturation current density [169].  $k$  and  $T$  are Boltzmann's constant and the absolute temperature in K respectively. For negative values of  $V$  the junction is biased in reverse direction. For a large negative bias the current converges towards the saturation current density. The value of the saturation current density depends on the analytic model used to describe the junction. In the thermionic emission model the saturation current density is field independent [170]. In the diffusion model the current density is weakly field dependent with  $\gamma = 0.5$  [171]. Both models predict that the saturation current density scales exponentially with the potential barrier for charge carriers presented by the junction such that

$$j_0 \propto e^{-\frac{\Phi}{kT}} \quad (7.9)$$

with  $\Phi$  as the potential barrier.

The finding of a sub-ohmic current regime refutes the proposed model Huang et al. who have measured current-voltage curves of APC-CKL1 thin films on ITO coated glass substrates. Their model predicts a transition into space charge limited current in which  $\gamma$  would assume a value of two or larger [64, 172]. However, current-voltage curves, which support their claim have not been provided.

The exponential current-voltage behavior in polymers observed at low fields has been reported by several groups [64, 173, 47]. It is often explained by the Schottky effect. The Schottky effect describes the lowering of the potential barrier  $\Phi$  by image charges that accumulate on both sides of the junction. In the model presented in equation 7.8 can be extended in order to include the the Schottky effect. The modified current density is given by

$$j(E) = j_0(e^{(V/kT)} - 1)e^{\frac{\beta_s \sqrt{E}}{kT}}. \quad (7.10)$$

$\beta_s$  is the Schottky coefficient given by  $\sqrt{q/(4\pi\epsilon_0\epsilon_r)}$  where  $q$  and  $\epsilon_0$  are the unit charge and the vacuum permittivity [174].  $\epsilon_r$  and  $E$  are the relative permittivity of the semiconductor and the externally applied electric field respectively. For large negative values of  $V$  equation 7.8 takes the simple form of  $j(E) = j_0 e^{\frac{\beta_s \sqrt{E}}{kT}}$ , which matches the current-voltage curves in figure 7.6.

Alternatively the exponential current-voltage relation at low fields can be explained by Poole-Frenkel emission. In this model it is assumed that charge carriers move through an insulator by hopping from one trap state to the next. The charge carriers are thermally excited and the electric field lowers the potential barrier between adjacent hopping sites. The current for Poole-Frenkel emission is given by

$$j(E) \propto E e^{-\frac{q\Psi}{kT}} e^{\frac{\beta_{pf} \sqrt{E}}{kT}} \quad (7.11)$$

where  $\beta_{pf} = \sqrt{q/(\pi\epsilon_0\epsilon_r)}$  is the Poole-Frenkel coefficient.  $\Psi$  is the depth of the trap potential [175, 176]. Both conduction mechanisms are exponentially dependent on the square root of the electric field  $E$ . For sufficiently large electric fields the multiplication with the electric field in the case of Poole-Frenkel emission does not lead to considerable deviations from the straight line in the Schottky plot [177]. It should be emphasized that Poole-Frenkel emission is only determined by the bulk properties of the polymer while barrier lowering due to the Schottky effect is a process that is influenced by the electronic properties of the electrode. Previous publications have shown that Poole-Frenkel emission is the limiting factor for the current density in polycarbonate for wide range of applied electric fields [178, 179].

As Poole-Frenkel emission and barrier lowering due to the Schottky effect lead to similar current-voltage dependencies a differentiation of those two mechanisms is challenging. However, assuming that for the low field regime the current-voltage behavior is dominated by the Schottky effect means that the Schottky effect is only present until a certain applied field. This is not consistent with the established models. Assuming Poole-Frenkel emission on the other hand would mean that for low applied field the current is bulk limited and enters an interface limited regime once the Poole-Frenkel emission surpasses the saturation current.

A transition from bulk limited current to a saturated current regime has been reported before by Mazur [180]. He studied the current-voltage dependence and space charge distribution in PMMA using nickel electrodes. For small electric fields he found bulk limited current. For higher fields the current showed a square root dependence, which matches with the diffusion model for a reverse biased pn junction. The measured space charge distribution supports the model of a junction in reverse direction given by the Shockley equation.

Further evidence for Poole-Frenkel emission at low fields can be found by calculating the values of  $\beta$  from figure 7.6. The values for  $\beta$  are  $5.77 \cdot 10^{-5} \text{ eV} \sqrt{\frac{m}{V}}$ ,  $5.48 \cdot 10^{-5} \text{ eV} \sqrt{\frac{m}{V}}$  and  $4.63 \cdot 10^{-5} \text{ eV} \sqrt{\frac{m}{V}}$  for ITO coated glass, silicon and aluminum oxide coated silicon respectively. Dielectric measurements of thin films showed a static permittivity of 3.8. The corresponding values for  $\beta_{pf}$  and  $\beta_s$  are  $3.89 \cdot 10^{-5} \text{ eV} \sqrt{\frac{m}{V}}$  and  $1.94 \cdot 10^{-5} \text{ eV} \sqrt{\frac{m}{V}}$  respectively. Taking the average value of  $\beta$  for all substrate types the deviation from the theoretic value of  $\beta_{pf}$  is only 26 %. Based on the given analysis a transition from bulk limited Poole-Frenkel emission to interface limited saturation is the likeliest explanation for the observed current-voltage characteristic.

### 7.2.2 Interrelation between Electronic Substrate Properties and the Electro-Optic Coefficient

Having established a qualitative model of the different current regimes it is possible to analyze how the electronic properties of the substrate influence the current region conduction. For PMMA Mazur found a strong space negative space charge

in the vicinity of the positively biased electrode [180]. This space charge leads to a field enhancement close to the interface and to a screening of the electric field inside the polymer. The electric field at the interface can be several times larger than in the polymer bulk. It can thus be said that the voltage applied to the sample during poling is divided between a narrow space charge region close to the interface and the polymer bulk.

It has been noted before that an inhomogeneous field distribution inside the polymer film is detrimental for the attainable electro-optic coefficient [64]. In order to obtain high electro-optic coefficients the electronic properties of the hole injecting electrode should be chosen such that space charges are avoided. A qualitative judgment on how well space charges are avoided can be obtained by comparing the saturation current densities. Two extreme cases can be considered: For a very low value of the saturation current density the current would be in the saturated regime irrespectively of the applied field. In this case the polymer bulk would be almost field free and the applied voltage would drop only over the space charge region close to the interface. In the case of a large saturation current density the interface has a low resistivity and no significant voltage drop over the interface is expected. As the local electric field and the space charge density are linked by Poisson's equation this also means that no significant space charges are to be expected in this case. It can therefore be concluded that a low saturation current density is indicative for strong space charges inside the polymer during poling. The measurement of the saturation current therefore provides a simple method in order to compare the amount of space charge during poling for different types of substrates.

Even though the presented model allows to assess the amount of space charge created by a given electrode based on current-voltage measurements it does not explain how the space charge formation is linked to the electronic properties of the interface or how it can be avoided. In the case of ITO coated glass substrates the interface can be modeled by a metal-semiconductor junction taking the HOMO and LUMO levels of the polymer instead of conduction and valence band of the semiconductor. Neglecting interface states the saturation current is determined by the metal work function of ITO, which defines the hole barrier  $\Phi$  [165].

Sailor et al. have shown that also silicon-organic junctions can be modeled by established semiconductor methods if the metal contact is replaced by silicon and the polymer is taking the place of the semiconductor [181]. However, intermediate layers such as the native oxide or additional coatings need to be taken into account carefully.

Green et al. have shown that the saturation current density in metal-insulator-semiconductor (MIS) diodes is determined by the potential barriers for electrons and holes presented by the insulator [174, 182]. The insulator thicknesses considered in their work was between one and three nanometers, which is similar to the thickness of the native silicon oxide [183, 182]. For such thin insulators the tunneling current through the insulators is the dominant charge transport mechanism.

In their studies Green et al. found that a low saturation current density is obtained if the barrier for minority carriers in the semiconductor is significantly lower than for majority carriers. In this case the charge transport is dominated by tunneling of minority carriers from the semiconductor to the metal. Under these conditions the semiconductor is inverted close to the metal interface and a strong space charge is formed. For lower majority carrier barriers the current is dominated by tunneling of majority carriers from the metal to the semiconductor. In this case the semiconductor is weakly accumulating. An inversion close to the interface is only observed for large negative bias. The saturation current density in the case of a majority carrier dominated current can be orders of magnitude larger than for minority carrier dominated current. A schematic for both cases is shown in figure 7.7.

Green's results indicate that in order to avoid space charge formation in APC-CKL1 on silicon substrate the interface barriers need to be altered such that the current through the interface is dominated by injection of holes from the silicon into the polymer. It has been confirmed experimentally that an interface modification by a thin insulating layer can alter the interface barriers and thereby increase the saturation current by several orders of magnitude [184, 185]. It is important to note that besides the bulk properties of the insulator interfacial charges can have

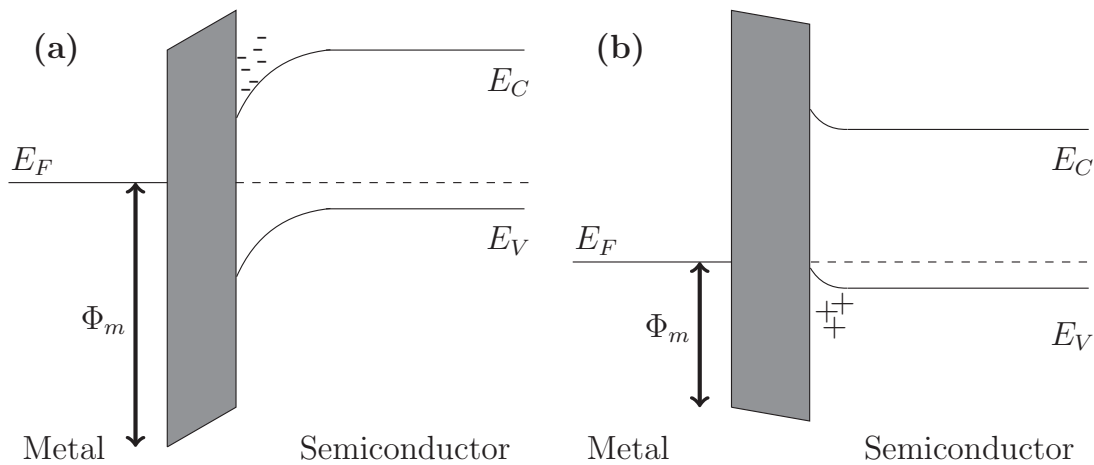


**Figure 7.7:** shows schematic band diagrams for a MIS structure for (a) a high majority carrier barrier and (b) low majority carrier barrier. The insulator is depicted by a gray shade. Plus and minus signs indicate the respective space charges in the semiconductor.  $\Phi_m$  denotes the potential barrier for majority carriers.

a strong influence on the barrier height. Barrier height changes of up to 0.5 eV due to surface charge effects have been reported [186].

In order to test if the concept of interface modification can be transferred to silicon-polymer junctions amorphous aluminum oxide was chosen as interface modifier. Thin layers of alumina had been previously used as interface modifiers in order to increase the saturation current [184]. The reported LUMO level of amorphous aluminum oxide is close that of the native oxide leading to an increase of the tunneling resistance for electrons [174, 187]. The reported HOMO level of amorphous aluminum oxide is 0.4 eV above the silicon valence band and the reported HOMO of the polymer [165]. Hence, the influence on the hole tunneling current is assumed to be weak.

Comparing the current-voltage measurements on untreated silicon substrate and silicon substrate coated with 5 nm aluminum oxide two observations can be made. First, the current-voltage curve is shifted towards higher electric fields. This observation is in line with the work from Dogish and Ho who pointed out that for MIS structures the potential drop over the insulator is strongly depending

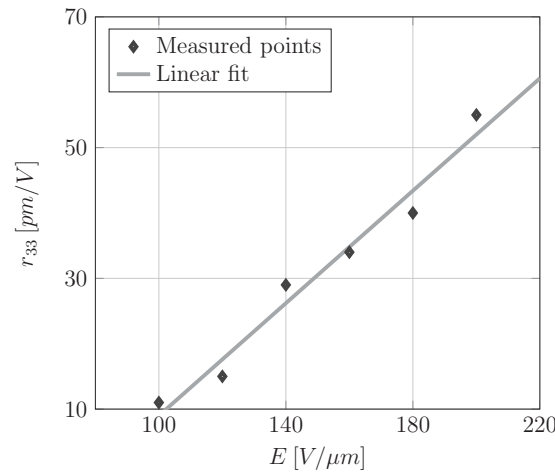


**Figure 7.8:** shows the measured electro-optic coefficient  $r_{33}$  for aluminum oxide coated silicon as a function of the applied electric field.

on the insulator thickness. For thick insulating layers a significant potential drop over the insulator can be expected, while for thinner layer the potential drop is mainly taking place in the space charge region [188]. More importantly however, the saturation current density is increased from about  $2 \text{ A/m}^2$  for untreated silicon to  $6 \text{ A/m}^2$  for aluminum oxide coated silicon.

The current-voltage measurements are complemented by measurements of the electro-optic coefficients on aluminum oxide coated silicon samples. The coefficients have been measured using the modified Teng-Man method introduced in the previous section. The obtained values of  $r_{33}$  can be found in figure 7.8. A good way to compare different substrates in terms of their poling efficiency is to consider a constant current density. Depending on the electronic properties of the electrode interface a given current density will imprint a characteristic space charge distribution on the polymer film. Comparing the current density instead of the externally applied electric field is advantageous because potential drops over additional insulating layers and the resulting shift of the current-voltage curve are automatically taken into account. This way the experimental challenge of measuring the electronic properties of the interface modifications is avoided.

Figure 7.9 shows the obtained electro-optic coefficients for the three investigated substrate types as a function of the current density. The values on the x-

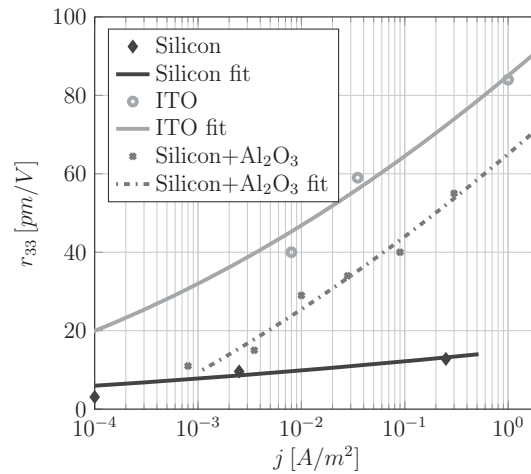


**Figure 7.9:** shows the measured electro-optic coefficient  $r_{33}$  as a function of the poling current for different substrates. Measured points are indicated by markers.

axis are obtained by looking up the corresponding current densities for the applied poling fields in figure 7.6. The fitted curves correspond to a linear dependence between  $r_{33}$  and the poling field. The measurements show that highest electro-optic coefficients were obtained for samples with ITO electrodes, followed by aluminum oxide coated silicon substrate and uncoated silicon. At current densities of  $5 \cdot 10^{-1}$  A/m<sup>2</sup> all substrates are still in the Poole-Frenkel regime, however the measured electro-optic coefficients show the influence of the space charges. The electro-optic coefficient for plain silicon substrate is 14 pm/V while for alumina uncoated silicon a value of 62 pm/V was obtained, an improvement by more than a factor of four. The  $r_{33}$  coefficient for alumina coated silicon is 20 % lower than on ITO coated glass substrates for the same current density. The electro-optic measurements confirm the expected correlation between the saturation current and the attainable electro-optic coefficient.

In summary it was shown that the low electro-optic coefficients found in silicon slotted waveguides are also found in polymer thin films on silicon substrate. In contrast to Teng-Man measurements of thin films on glass substrates, silicon substrates allow to measure both electro-optic coefficients independently by taking advantage of strong multiple reflections at the interfaces. The measurements

showed a ratio of three between the  $r_{33}$  and  $r_{13}$  coefficient as predicted by the free gas model.

In order to identify possible reasons for the low electro-optic coefficients on silicon substrate current-voltage measurements were performed on thin films of APC-CKL1 for ITO coated glass substrates and silicon substrate. The measurements revealed a distinctive saturation of the current density at high electric fields. The saturation was observed for all samples but it was particularly pronounced for silicon substrates. The current-voltage measurements were explained by bulk limited Poole-Frenkel emission for low fields. For high fields the current enters an interface limited regime and can be modeled like a reverse biased pn junction.

The presented model predicts the formation of a space charge region and a strong concentration of the electric field close to the hole injecting interface. It was shown that a saturation of the current at low current densities is indicative for a strong space charge and an inhomogeneous field distribution inside the polymer film. Therefore the space charges formed inside the polymer films during poling are expected to be more pronounced on silicon substrate, which would explain the low electro-optic coefficients compared to ITO coated glass substrates. It was also shown that an interface modification of the silicon surface by a thin layer of aluminum oxide increases the saturation current. Measurements of the electro-optic coefficient confirmed the correlation of a high saturation current and a high electro-optic coefficient.

The fact that the electro-optic coefficients on ITO substrate are higher as for the alumina coated silicon substrate indicates that aluminum oxide might not be an optimum choice as interface modifier. A systematic study is necessary in order to find more effective interface modifiers, which yield higher electro-optic coefficients. The correlation between the saturation current and space charge formation allows to evaluate interface modifications based on simple current-voltage measurements. The electro-optic measurements, which are more time consuming can then be conducted for a small number of modifications with the highest saturation current densities.



# Chapter 8

## Conclusion and Outlook

### 8.1 Conclusion

This thesis is motivated by the increasing need of electro-optic modulators with large electrical bandwidth and low modulation amplitude. The beneficial combination of high refractive index silicon and electro-optic polymers for this purpose has been highlighted before in several publications. The high refractive index of silicon allows to create waveguides with strong confinement and the formation of resonators with high quality factors. By introducing slots into waveguides or resonators light can be concentrated in a low refractive index polymer cladding. Additionally the small slots allow to apply strong electric fields to the polymer using moderate voltages, which reduces the energy consumption of the modulator.

It has been shown before that the major requirements for next generation electro-optic modulators such as high electrical bandwidth, low modulation amplitude and small geometrical footprint can be met using polymer infiltrated photonic crystal cavities. Nevertheless, up to now these structures are not used in commercial products. This thesis is aimed at the resolution of challenges, which so far have averted the use of hybrid silicon-polymer resonators as electro-optic modulators and filters, namely:

- Fabrication induced random geometry fluctuations

- Low quality factor
- Low in device electro-optic coefficients

The compensation of random geometry fluctuations is one of the major issues for resonant filters and modulators. Precise placement of the optical resonance for WDM applications require fabrication accuracies, which are in the order of one atom. In chapter 3 it is shown that electron-beam or UV bleaching of a dye doped polymer cladding can be used to compensate such geometry fluctuations. In silicon ring resonators wavelength offsets of up to 4.3 and 16.4 nm can be compensated by bleaching for TE and TM polarization respectively. The resonators can be adjusted in wavelength with a resolution of 12 pm corresponding to a frequency shift of 1.5 GHz. The main advantages of the bleaching approach are temperature stability, compatibility with UV lithographic equipment and high wavelength resolution.

Since bleaching can be applied in a spatially resolved way, local modifications of silicon waveguide structures are possible. This is particularly interesting for photonic crystal waveguides, which have a strong frequency dependence. In chapter 4 it was shown that spatially resolved bleaching of photonic crystal waveguides can be used to create configurable optical components such as tunable edge filters, and resonators by effectively reducing the local lattice constant of the photonic crystal. The effective local lattice constant can be defined with resolution of 7.6 pm, which is a factor of 70 smaller than the silicon lattice constant. In order to demonstrate the versatility of the bleaching process a photonic crystal resonator with an intrinsic quality factor of  $2.6 \cdot 10^5$  was defined in a previously non-resonant photonic crystal waveguide.

The quality factors of bleached cavities presented in chapter 4 are sufficient to create energy efficient electro-optical modulators. However, in order to explain the the underlying mechanisms that determine the quality factor of photonic crystal resonators a more in-depth analysis was provided in chapter 5. One particular feature for polymer infiltrated photonic crystal resonators is the vertical asymmetry of the cladding refractive index. It was shown that this asymmetry leads to undesired coupling of the resonant mode to a quasi TM mode, which is not confined

to the cavity. It was also shown that this coupling is the dominant loss factor in vertically asymmetric photonic crystal cavities.

In order to increase the quality factor several approaches were discussed. It was shown that for a proper choice of geometrical parameters resonators with a single step defect can yield acceptable quality factors for electro-optic modulation. If higher quality factors are desired, graded defects can be employed. A procedure was provided in order to synthesize multistep photonic crystal cavities, which exhibit a defined field envelope. Field envelopes with a narrow k-vector distribution such as Gaussian envelopes significantly reduce the vertical radiation and the coupling to quasi TM modes. Though the Gaussian function is generally a good choice as field envelope it does not necessarily yield optimal quality factors in cases where a very narrow k-vector spectrum is required. In these cases raised cosine shaped field envelopes lead to significantly higher quality factors. Enhancements of the quality factor by a factor of 63 have been obtained analytically comparing cavities with raised cosine and Gaussian field envelopes of identical effective mode volume. In numeric simulations a maximum enhancement of the quality factor by a factor of 30 has been found.

Chapter 6 provides experimental methods and results for electro-optically tunable silicon waveguides. The poling field and the poling temperature were optimized in order to increase the in-device electro-optic effect. A maximum electro-optic coefficient of 25 pm/V was obtained in a 100 nm slot, which is roughly a factor of two larger than the reported electro-optic coefficients for comparable geometries. Electro-optic amplitude modulation has been realized in a photonic crystal cavity of quality factor 3,300. Furthermore high frequency electro-optic modulation has been demonstrated with modulation frequencies up to 40 GHz. No significant roll off has been observed, which confirms the large electrical bandwidth of this type of modulator.

Despite the significant improvement of the in-device electro-optic coefficient due to the optimization of the poling process this study did not provide insight why the in-device electro-optic coefficients deviate so strongly from the coefficients measured in thin films on ITO coated glass substrates. In order to investigate this

aspect thin polymer films on silicon substrates have been studied. These films have been poled and electro-optically characterized by the Teng-Man method. One remarkable property of high refractive index substrates like silicon is the fact that it is possible to measure both electro-optic coefficients in a single measurement. The electro-optic coefficients found in this experiment are similar to the values found in slotted waveguides. It was therefore evident that the low electro-optic coefficients in APC-CKL1 poled with silicon electrodes must be linked to the electronic properties of silicon.

In order to identify the physical mechanisms that govern the current conduction during poling current-voltage curves have been measured for silicon and ITO coated glass substrates. Unlike previously reported results for other electro-optic polymers thin films of APC-CKL1 show a distinctive current saturation for high applied fields. The saturation has been observed both for ITO coated glass substrate and silicon substrate. Based on the provided model the saturation of the poling current is found to be indicative for the formation of a space charge region close to the positively biased electrode. The space charge region leads to an inhomogeneous electric field distribution inside the polymer film, which is detrimental for obtaining high electro-optic coefficients. The provided current-voltage measurements show that the current saturation is particularly pronounced for silicon substrates. The presented results show that the saturation current density and the electro-optic coefficients are correlated. An increase of the saturation current by a factor of three could be achieved by modifying the silicon interface with a thin layer of  $\text{Al}_2\text{O}_3$ . The measured electro-optic coefficient on aluminum oxide coated silicon was a factor of four higher compared to a treated silicon substrate poled with the same current density.

In summary it can be said that the challenge of fabrication induced fluctuations in silicon resonators can be treated effectively using the presented bleaching approach. The mechanisms, which govern the quality factor in polymer infiltrated photonic crystal resonators have been analyzed and structures with sufficient quality factor have been fabricated. Electro-optic modulation in polymer infiltrated photonic crystals was demonstrated experimentally. Furthermore, electro-optic

and current-voltage measurements in thin films on silicon and ITO coated glass substrate have been performed. Based on the experimental evidence it is suspected that the low electro-optic coefficients on silicon substrate and in silicon waveguides are a result of detrimental space charges formed during poling. It was shown for thin films on silicon substrate that a 5 nm coating of aluminum oxide helps to avoid detrimental space charges and leads to four times larger electro-optic coefficients compared to untreated silicon substrates.

## 8.2 Outlook

The numeric and experimental data provided in this thesis show that both the challenges of random process fluctuations and the fabrication of silicon photonic crystal cavities with sufficient quality factor are manageable. This holds in particular for professional facilities with specialized equipment.

A problem, which could not be resolved entirely within the scope of this thesis is the low poling efficiency in silicon waveguides and in thin films on silicon substrate. Strong evidence was presented that the low poling efficiency for silicon electrodes is related to the formation of a detrimental space charge during poling but more experiments are necessary to obtain a quantified model of the silicon-polymer interface and its electrical properties. In particular a thickness dependent study of the electro-optic coefficient and current-voltage behavior would be valuable in this respect.

The firm understanding of the electronic properties of the silicon-polymer interface could be the basis for future research projects in which tailored interface modifications are studied to improve the electro-optic coefficient in silicon slotted waveguides. Thin films on silicon substrate represent a good model system for such kind of study due to the simple sample fabrication and geometry. The provided experimental results have shown that a first assessment of interface modifiers is possible by comparing the saturation current obtained from current-voltage measurements. In a second step the electro-optic coefficient for the most promising candidates can be checked using the Teng-Man method. Knowledge obtained in

the thin film system can then be transferred to slotted waveguides. The fact that the  $r_{33}$  coefficient could be significantly enhanced by applying a 5 nm thick coating of aluminum oxide to the silicon underlines the potential of this approach.

Another aspect, which could not be systematically studied in this work is the question whether poling in slotted waveguides leads to a decay of chromophore molecules and additional poling induced losses. Evidence for this was observed in slotted photonic crystal cavities. This question could be answered by doing reflection spectroscopy of poled thin films on silicon substrate.

Aside from the poor alignment and potential poling induced losses high field poling is related to several other problems such as limited chromophore density, CMOS incompatibility and thermal instability. It is therefore reasonable to investigate alternatives to electric field poling. One possible approach to avoid high field poling is using self assembled layers. Self assembled layers possess the potential of a far better polar alignment of the chromophore molecules than poled films [189].

Of particular interest in this respect are self assembled superlattices. Self assembled superlattices are typically built up in a layer by layer fashion. Each monolayer is covalently bound to the previous layer. Katz et al. have demonstrated this approach by using a chromophore molecule which can covalently bind to a chemically functionalized surface [189]. The chromophore molecules self assemble until all available bonding sites at the surface are saturated. Afterwards the layer is immersed into a second solution which activates a second bonding site in the chromophore molecules which allows the next layer of chromophores to bond. Using this approach Katz et al. have obtained highly oriented layers, which are mechanically and thermally stable.

In order to self assemble chromophore molecules inside a slotted waveguide it is necessary to differentiate the two sides of the slotted waveguide in order to break the symmetry of the structure. This can be done lithographically by covering one of the two rails with a photoresist. Figure 8.1 shows a cross section image, which illustrates the approach.

Comparing the performance of reported silicon modulators based on the plasma dispersion effect and hybrid silicon-organic modulators reported it can be said that

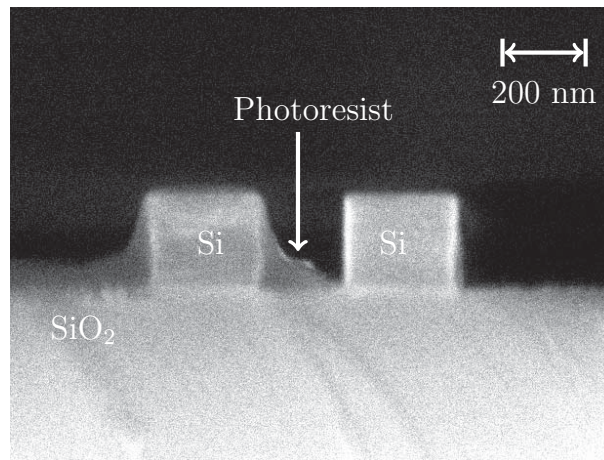


**Figure 8.1:** shows the cross section of a slotted waveguide. The left rail of the waveguide is covered with a thin layer of photoresist while the right rail is exposed and can be functionalized by wet chemistry.

currently hybrid modulators feature larger electrical modulation bandwidth. On the other hand, non-hybrid modulators require smaller modulation signals and are fully CMOS compatible i.e. no poling is required. Full CMOS compatibility is also the major reason why plasma dispersion based modulators dominate the market for integrated electro-optic modulators.

The fact that since 2012 only few works have reported progress in modulations speed for plasma dispersion based modulators have appeared indicates that the possibilities for geometry and doping optimization are nearly exhausted. As the physical limitations such as carrier drift velocity cannot be changed easily the demand for larger modulation speeds will promote a shift to other types of electro-optic modulators. The question whether hybrid silicon-organic modulators can take their place depends crucially on the question whether it will be possible to remedy the problems related to high field poling.

# Appendix A

## Beam Characterization by the Knife Edge Method

The intensity distribution  $I(\rho, z)$  of a Gaussian beam can be written as

$$I(\rho, z) = \frac{2P_0}{\pi W(z)} \exp\left(-\frac{2\rho^2}{W^2(z)}\right) \quad (\text{A.1})$$

where  $z$  is the direction of propagation and  $\rho$  is the radial direction.  $P_0$  and  $W$  are the integrated power of the beam and the beam radius given by  $W(z) = W_0 \sqrt{1 + (\frac{z}{z_0})^2}$ .  $z_0$  and  $W_0$  are the Rayleigh length and the beam waist radius respectively [60].

In order to find the parameters  $W_0$  and  $z_0$  a knife edge is positioned at different points along the direction of propagation. For each point the knife edge is moved normal to the direction of propagation. A large area photo detector is used to measure the power as the knife edge is moved normal to the propagation direction.

Figure A.1 shows a sample measurement. The beam power behind the knife edge as a function of the lateral position of the edge  $x$  follows a Gaussian error function [190]

$$P(x, z) = \frac{P_0}{2} \left(1 - \operatorname{erf}\left(\frac{\sqrt{2}x}{W(z)}\right)\right). \quad (\text{A.2})$$

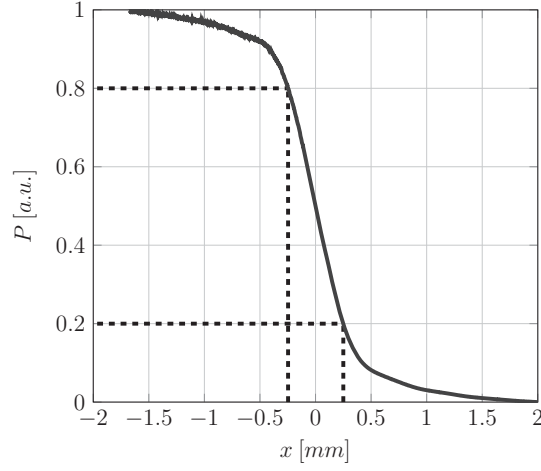


**Figure A.1:** shows an example for a knife edge measurement. The measured points are depicted by a blue line. 20% and 80% values are indicated by dashed black lines.

Since the shape of the function  $P(x, z)$  is known fitting of the whole function is not necessary. Instead the x-coordinates for  $0.8P_0$  and  $0.2P_0$  are interpolated from the measured data. Inserting those values into A.2 gives

$$W(z) = \frac{\sqrt{2}x|_{P=0.8P_0}}{\operatorname{inverf}(0.6)P_0} \quad (\text{A.3})$$

and

$$W(z) = -\frac{\sqrt{2}x|_{P=0.2P_0}}{\operatorname{inverf}(0.6)P_0} \quad (\text{A.4})$$

where  $\operatorname{inverf}$  is the inverse error function. Summing up the two equations  $W(z)$  can be written as

$$W(z) = \frac{x|_{P=0.8P_0} - x|_{P=0.2P_0}}{\sqrt{2}\operatorname{inverf}(0.6)P_0}. \quad (\text{A.5})$$

Fitting the obtained values for  $W(z)$  with the expression  $W_0\sqrt{1 + (\frac{z}{z_0})^2}$  the beam waist and the Rayleigh length can be determined. The opening angle divergence  $\Delta\Theta(z)$  can be calculated from the  $W(z)$  by

$$\Delta\Theta(z) = 2\operatorname{atan}\left(\frac{dW}{dz}\right). \quad (\text{A.6})$$



# Bibliography

- [1] A. Das, M. Schuchhardt, N. Hardavellas, G. Memik, and A. Choudhary, “Dynamic directories: A mechanism for reducing on-chip interconnect power in multicores,” in *Proceedings of the Conference on Design, Automation and Test in Europe*, pp. 479–484, EDA Consortium, 2012.
- [2] A. Fanara, “Report to congress on server and data center energy efficiency,” tech. rep., U.S. Environmental Protection Agency, 2007.
- [3] M. Eastwood, “Worldwide server market revenues decline -6.2% in second quarter as market demand remains weak, according to idc,” tech. rep., IDC Corporate USA, 2013.
- [4] J. Rosenberg, W. Green, S. Assefa, D. Gill, T. Barwicz, M. Yang, S. Shank, and Y. Vlasov, “A 25 Gbps silicon microring modulator based on an interleaved junction,” *Optics express*, vol. 20, no. 24, pp. 26411–26423, 2012.
- [5] A. N. Udipi, N. Muralimanohar, R. Balasubramonian, A. Davis, and N. P. Jouppi, “Combining memory and a controller with photonics through 3d-stacking to enable scalable and energy-efficient systems,” in *ACM SIGARCH Computer Architecture News*, vol. 39, pp. 425–436, ACM, 2011.
- [6] X. Zheng, F. Liu, J. Lexau, D. Patil, G. Li, Y. Luo, H. Thacker, I. Shubin, J. Yao, K. Raj, R. Ho, J. Cunningham, and A. Krishnamoorthy, “Ultralow power 80 Gb/s arrayed CMOS silicon photonic transceivers for WDM optical links,” *Lightwave Technology, Journal of*, vol. 30, pp. 641–650, Feb 2012.

- [7] M. Birk, P. Gerard, R. Curto, L. Nelson, X. Zhou, P. Magill, T. Schmidt, C. Malouin, B. Zhang, E. Ibragimov, *et al.*, “Real-time single-carrier coherent 100 Gb/s PM-QPSK field trial,” *Journal of Lightwave Technology*, vol. 29, no. 4, pp. 417–425, 2011.
- [8] G. Cocorullo, F. Della Corte, and I. Rendina, “Temperature dependence of the thermo-optic coefficient in crystalline silicon between room temperature and 550 K at the wavelength of 1523 nm,” *Applied Physics Letters*, vol. 74, no. 22, pp. 3338–3340, 1999.
- [9] T. Chu, H. Yamada, S. Ishida, and Y. Arakawa, “Compact 1 x N thermo-optic switches based on silicon photonic wire waveguides,” *Optics Express*, vol. 13, no. 25, pp. 10109–10114, 2005.
- [10] R. A. Soref and B. Bennett, “Electrooptical effects in silicon,” *Quantum Electronics, IEEE Journal of*, vol. 23, no. 1, pp. 123–129, 1987.
- [11] G. V. Treyz, P. May, and J. M. Halbout, “Silicon optical modulators at 1.3  $\mu\text{m}$  based on free-carrier absorption,” *Electron Device Letters, IEEE*, vol. 12, no. 6, pp. 276–278, 1991.
- [12] J. Lorenzo and R. Soref, “1.3  $\mu\text{m}$  electro-optic silicon switch,” *Applied Physics Letters*, vol. 51, no. 1, pp. 6–8, 1987.
- [13] C. A. Barrios, V. R. Almeida, R. Panepucci, and M. Lipson, “Electro-optic modulation of silicon-on-insulator submicrometer-size waveguide devices,” *Journal of Lightwave Technology*, vol. 21, no. 10, p. 2332, 2003.
- [14] A. Liu, R. Jones, D. Samara-Robio, D. Rubin, O. Cohen, and R. Nicolaescu, “A high-speed silicon optical modulator based on a metal-oxide-semiconductor capacitor,” *Nature*, vol. 427, no. 6975, pp. 615–618, 2004.
- [15] F. Gardes, G. Reed, N. Emerson, and C. Png, “A sub-micron depletion-type photonic modulator in silicon on insulator,” *Optics Express*, vol. 13, no. 22, pp. 8845–8854, 2005.



- [16] C. A. Barrios, V. R. de Almeida, and M. Lipson, “Low-power-consumption short-length and high-modulation-depth silicon electrooptic modulator,” *Journal of Lightwave Technology*, vol. 21, no. 4, p. 1089, 2003.
- [17] A. Liu, L. Liao, D. Rubin, H. Nguyen, B. Ciftcioglu, Y. Chetrit, N. Izhaky, and M. Paniccia, “High-speed optical modulation based on carrier depletion in a silicon waveguide,” *Optics Express*, vol. 15, no. 2, pp. 660–668, 2007.
- [18] M. Ziebell, D. Marris-Morini, G. Rasigade, J.-M. Fédéli, P. Crozat, E. Cassan, D. Bouville, and L. Vivien, “40 Gbit/s low-loss silicon optical modulator based on a pinip diode,” *Optics Express*, vol. 20, no. 10, pp. 10591–10596, 2012.
- [19] S. Manipatruni, Q. Xu, and M. Lipson, “Pinip based high-speed high-extinction ratio micron-size silicon electrooptic modulator,” *Optics Express*, vol. 15, pp. 13035–13042, Oct 2007.
- [20] D. Thomson, F. Gardes, J. M. Fedeli, S. Zlatanovic, Y. Hu, B. P. P. Kuo, E. Myslivets, N. Alic, S. Radic, G. Mashanovich, and G. Reed, “50-Gb/s silicon optical modulator,” *Photonics Technology Letters, IEEE*, vol. 24, no. 4, pp. 234–236, 2012.
- [21] T. Baehr-Jones, M. Hochberg, G. Wang, R. Lawson, Y. Liao, P. Sullivan, L. Dalton, A. Jen, and A. Scherer, “Optical modulation and detection in slotted silicon waveguides,” *Optics Express*, vol. 13, no. 14, pp. 5216–5226, 2005.
- [22] J. Luo, X.-H. Zhou, and A. K.-Y. Jen, “Rational molecular design and supramolecular assembly of highly efficient organic electro-optic materials,” *Journal of Materials Chemistry*, vol. 19, pp. 7410–7424, 2009.
- [23] G. L. Li, P. K. L. Yu, and I. Tutorial, “Optical intensity modulators for digital and analog applications,” *Journal of Lightwave Technology*, vol. 21, no. 9, p. 2010, 2003.

- [24] S. Xiao, F. Wang, X. Wang, Y. Hao, X. Jiang, M. Wang, and J. Yang, “Electro-optic polymer assisted optical switch based on silicon slot structure,” *Optics Communications*, vol. 282, no. 13, pp. 2506 – 2510, 2009.
- [25] J. Witzens, T. Baehr-Jones, and M. Hochberg, “Design of transmission line driven slot waveguide mach-zehnder interferometers and application to analog optical links,” *Optics Express*, vol. 18, no. 16, pp. 16902–16928, 2010.
- [26] T. Baehr-Jones, B. Penkov, J. Huang, P. Sullivan, J. Davies, J. Takayesu, J. Luo, T.-D. Kim, L. Dalton, A. Jen, M. Hochberg, and A. Scherer, “Nonlinear polymer-clad silicon slot waveguide modulator with a half wave voltage of 0.25 V,” *Applied Physics Letters*, vol. 92, no. 16, p. 163303, 2008.
- [27] R. Ding, T. Baehr-Jones, Y. Liu, R. Bojko, J. Witzens, S. Huang, J. Luo, S. Benight, P. Sullivan, J.-M. Fedeli, M. Fournier, L. Dalton, A. Jen, and M. Hochberg, “Demonstration of a low  $V_{\pi}L$  modulator with GHz bandwidth based on electro-optic polymer-clad silicon slot waveguides,” *Optics Express*, vol. 18, no. 15, pp. 15618–15623, 2010.
- [28] W. M. Green, M. J. Rooks, L. Sekaric, and Y. A. Vlasov, “Ultra-compact, low RF power, 10 Gb/s silicon Mach-Zehnder modulator,” *Optics Express*, vol. 15, no. 25, pp. 17106–17113, 2007.
- [29] C. Monat, B. Corcoran, M. Ebnali-Heidari, C. Grillet, B. J. Eggleton, T. P. White, L. O’Faolain, and T. F. Krauss, “Slow light enhancement of nonlinear effects in silicon engineered photonic crystal waveguides,” *Optics Express*, vol. 17, no. 4, pp. 2944–2953, 2009.
- [30] C.-Y. Lin, X. Wang, S. Chakravarty, B. S. Lee, W. Lai, J. Luo, A. K. Y. Jen, and R. Chen, “Electro-optic polymer infiltrated silicon photonic crystal slot waveguide modulator with 23 dB slow light enhancement,” *Applied Physics Letters*, vol. 97, no. 9, p. 093304, 2010.



- [31] G. Lenz, B. Eggleton, C. Madsen, and R. Slusher, "Optical delay lines based on optical filters," *Quantum Electronics, IEEE Journal of*, vol. 37, no. 4, pp. 525–532, 2001.
- [32] J. Li, T. P. White, L. O’Faolain, A. Gomez-Iglesias, and T. F. Krauss, "Systematic design of flat band slow light in photonic crystal waveguides," *Optics Express*, vol. 16, pp. 6227–6232, Apr 2008.
- [33] Q. Xu, B. Schmidt, S. Pradhan, and M. Lipson, "Micrometre-scale silicon electro-optic modulator," *Nature*, vol. 435, no. 7040, pp. 325–327, 2005.
- [34] B. Bortnik, Y.-C. Hung, H. Tazawa, B.-J. Seo, J. Luo, A. K. Y. Jen, W. H. Steier, and H. R. Fetterman, "Electrooptic polymer ring resonator modulation up to 165 GHz," *Selected Topics in Quantum Electronics, IEEE Journal of*, vol. 13, no. 1, pp. 104–110, 2007.
- [35] I.-L. Gheorma and J. Osgood, R.M., "Fundamental limitations of optical resonator based high-speed eo modulators," *Photonics Technology Letters, IEEE*, vol. 14, no. 6, pp. 795–797, 2002.
- [36] Y.-J. Cheng, J. Luo, S. Hau, D. H. Bale, T.-D. Kim, Z. Shi, D. B. Lao, N. M. Tucker, Y. Tian, L. R. Dalton, P. J. Reid, and A. K.-Y. Jen, "Large electro-optic activity and enhanced thermal stability from diarylaminophenyl-containing high- $\beta$  nonlinear optical chromophores," *Chemistry of Materials*, vol. 19, no. 5, pp. 1154–1163, 2007.
- [37] X. Piao, X. Zhang, Y. Mori, M. Koishi, A. Nakaya, S. Inoue, I. Aoki, A. Otomo, and S. Yokoyama, "Nonlinear optical side-chain polymers post-functionalized with high- $\beta$  chromophores exhibiting large electro-optic property," *Journal of Polymer Science Part A: Polymer Chemistry*, vol. 49, no. 1, pp. 47–54, 2011.
- [38] J. Luo and A.-Y. Jen, "Highly efficient organic electrooptic materials and their hybrid systems for advanced photonic devices," *Selected Topics in Quantum Electronics, IEEE Journal of*, vol. 19, no. 6, pp. 42–53, 2013.

- [39] K. D. Singer, M. G. Kuzyk, and J. E. Sohn, "Second-order nonlinear-optical processes in orientationally ordered materials: relationship between molecular and macroscopic properties," *Journal of the Optical Society of America B*, vol. 4, no. 6, pp. 968–976, 1987.
- [40] J.-L. Oudar and D. Chemla, "Hyperpolarizabilities of the nitroanilines and their relations to the excited state dipole moment," *The Journal of Chemical Physics*, vol. 66, no. 6, pp. 2664–2668, 1977.
- [41] M. Del Zoppo, C. Castiglioni, V. Gerola, P. Zuliani, and G. Zerbi, "Effect of bond length alternation and of bond length alternation oscillations on the molecular nonlinear optical response of push pull polyenes," *Journal of the Optical Society of America B*, vol. 15, no. 1, pp. 308–317, 1998.
- [42] S. Marder, B. Kippelen, and A. K.-Y. Jen, "Design and synthesis of chromophores and polymers for electro-optic and photorefractive applications," *Nature*, vol. 388, no. 6645, pp. 845–854, 1997.
- [43] L. Dalton and S. Benight, "Theory-guided design of organic electro-optic materials and devices," *Polymers*, vol. 3, no. 3, pp. 1325–1351, 2011.
- [44] M. G. Kuzyk, "Using fundamental principles to understand and optimize nonlinear-optical materials," *Journal of Materials Chemistry*, vol. 19, no. 40, pp. 7444–7465, 2009.
- [45] D. M. Burland, R. D. Miller, and C. A. Walsh, "Second-order nonlinearity in poled-polymer systems," *Chemical Reviews*, vol. 94, no. 1, pp. 31–75, 1994.
- [46] R. Wortmann and D. M. Bishop, "Effective polarizabilities and local field corrections for nonlinear optical experiments in condensed media," *The Journal of Chemical Physics*, vol. 108, no. 3, pp. 1001–1007, 1998.
- [47] R. Blum, M. Sprave, J. Sablotny, and M. Eich, "High-electric-field poling of nonlinear optical polymers," *Journal of the Optical Society of America B*, vol. 15, no. 1, pp. 318–328, 1998.



- [48] M. Eich, A. Sen, H. Looser, G. Bjorklund, J. Swalen, R. Twieg, and D. Yoon, “Corona poling and real-time second-harmonic generation study of a novel covalently functionalized amorphous nonlinear optical polymer,” *Journal of Applied Physics*, vol. 66, no. 6, pp. 2559–2567, 1989.
- [49] M. A. Mortazavi, A. Knoesen, S. T. Kowel, B. G. Higgins, and A. Dienes, “Second-harmonic generation and absorption studies of polymerdye films oriented by corona-onset poling at elevated temperatures,” *Journal of the Optical Society of America B*, vol. 6, no. 4, pp. 733–741, 1989.
- [50] J. Wu, “Birefringent and electro-optic effects in poled polymer films: steady-state and transient properties,” *Journal of the Optical Society of America B*, vol. 8, no. 1, pp. 142–152, 1991.
- [51] S. Herminghaus, B. A. Smith, and J. Swalen, “Electro-optic coefficients in electric-field-poled polymer waveguides,” *Journal of the Optical Society of America B*, vol. 8, no. 11, pp. 2311–2317, 1991.
- [52] L. Dalton, “Rational design of organic electro-optic materials,” *Journal of Physics: Condensed Matter*, vol. 15, no. 20, p. R897, 2003.
- [53] K. Singer and L. King, “Relaxation phenomena in polymer nonlinear optical materials,” *Journal of applied physics*, vol. 70, no. 6, pp. 3251–3255, 1991.
- [54] M. Eich, H. Looser, D. Y. Yoon, R. Twieg, G. Bjorklund, and J. C. Baumert, “Second-harmonic generation in poled organic monomeric glasses,” *Journal of the Optical Society of America B*, vol. 6, no. 8, pp. 1590–1597, 1989.
- [55] A. Suzuki and Y. Matsuoka, “Relaxation processes in poled nonlinear optical polymer films,” *Journal of applied physics*, vol. 77, no. 3, pp. 965–969, 1995.
- [56] P. McCluskey, C. O’Connor, and K. Nathan, “Evaluating the performance and reliability of embedded computer systems for use in industrial and automotive temperature ranges,” *Intel Developer Network News*, vol. 1, pp. 62–65, 2001.



- [57] S.-K. Kim, Y.-C. Hung, B.-J. Seo, K. Geary, W. Yuan, B. Bortnik, H. Fetterman, C. Wang, W. Steier, and C. Zhang, "Side-chain electro-optic polymer modulator with wide thermal stability ranging from  $-46\text{ }^{\circ}\text{C}$  to  $95\text{ }^{\circ}\text{C}$  for fiber-optic gyroscope applications," *Applied Physics Letters*, vol. 87, no. 6, pp. 061112–061112, 2005.
- [58] C. Zhang, C. Wang, J. Yang, L. R. Dalton, G. Sun, H. Zhang, and W. H. Steier, "Electric poling and relaxation of thermoset polyurethane second-order nonlinear optical materials: Role of cross-linking and monomer rigidity," *Macromolecules*, vol. 34, no. 2, pp. 235–243, 2001.
- [59] J. Luo, M. Haller, H. Li, T.-D. Kim, and A.-Y. Jen, "Highly efficient and thermally stable electro-optic polymer from a smartly controlled crosslinking process," *Advanced Materials*, vol. 15, no. 19, pp. 1635–1638, 2003.
- [60] E. Saleh and M. Teich, *Fundamentals of Photonics*. John Wiley and Sons, 1991.
- [61] W. Kozlovsky, C. D. Nabors, and R. Byer, "Efficient second harmonic generation of a diode-laser-pumped CW Nd:YAG laser using monolithic MgO:LiNbO<sub>3</sub> external resonant cavities," *Quantum Electronics, IEEE Journal of*, vol. 24, pp. 913–919, June 1988.
- [62] F. C. A. Pockels, *Lehrbuch der Kristallogoptik*, vol. 19. Leipzig, 1906.
- [63] H. Chen, B. Chen, D. Huang, D. Jin, J. D. Luo, A. K.-Y. Jen, and R. Dinu, "Broadband electro-optic polymer modulators with high electro-optic activity and low poling induced optical loss," *Applied Physics Letters*, vol. 93, no. 4, p. 043507, 2008.
- [64] S. Huang, T.-D. Kim, J. Luo, S. K. Hau, Z. Shi, X.-H. Zhou, H.-L. Yip, and A. K.-Y. Jen, "Highly efficient electro-optic polymers through improved poling using a thin tio<sub>2</sub>-modified transparent electrode," *Applied Physics Letters*, vol. 96, no. 24, p. 243311, 2010.



- [65] C. C. Teng and H. T. Man, “Simple reflection technique for measuring the electro-optic coefficient of poled polymers,” *Applied Physics Letters*, vol. 56, no. 18, pp. 1734–1736, 1990.
- [66] J. H. Wulbern, J. Hampe, A. Petrov, M. Eich, J. Luo, A. K.-Y. Jen, A. D. Falco, T. F. Krauss, and J. Bruns, “Electro-optic modulation in slotted resonant photonic crystal heterostructures,” *Applied Physics Letters*, vol. 94, no. 24, p. 241107, 2009.
- [67] J. H. Wülbern, S. Prorok, J. Hampe, A. Petrov, M. Eich, J. Luo, A. K.-Y. Jen, M. Jenett, and A. Jacob, “40 GHz electro-optic modulation in hybrid silicon–organic slotted photonic crystal waveguides,” *Optics Letters*, vol. 35, no. 16, pp. 2753–2755, 2010.
- [68] X. Wang, C.-Y. Lin, S. Chakravarty, J. Luo, A. K.-Y. Jen, and R. T. Chen, “Effective in-device  $r_{33}$  of 735 pm/V on electro-optic polymer infiltrated silicon photonic crystal slot waveguides,” *Optics letters*, vol. 36, no. 6, pp. 882–884, 2011.
- [69] L. Rayleigh, “XVII. On the maintenance of vibrations by forces of double frequency, and on the propagation of waves through a medium endowed with a periodic structure,” *The London, Edinburgh, and Dublin Philosophical Magazine and Journal of Science*, vol. 24, no. 147, pp. 145–159, 1887.
- [70] S. John *et al.*, “Strong localization of photons in certain disordered dielectric superlattices,” *Physical review letters*, vol. 58, no. 23, pp. 2486–2489, 1987.
- [71] E. Yablonovitch, “Inhibited spontaneous emission in solid-state physics and electronics,” *Physical review letters*, vol. 58, no. 20, p. 2059, 1987.
- [72] D. Joannopoulos, S. Johnson, and R. Meade, *Photonic Crystals: Molding the Flow of Light*. Princeton University Press, 2nd ed., 2008.
- [73] D. Taillaert, H. Chong, P. I. Borel, L. H. Frandsen, R. De La Rue, and R. Baets, “A compact two-dimensional grating coupler used as a polarization

- splitter,” *Photonics Technology Letters, IEEE*, vol. 15, no. 9, pp. 1249–1251, 2003.
- [74] J. H. Wülbern, M. Schmidt, M. Eich, U. Hübner, R. Boucher, F. Marlow, and W. Volksen, “Omnidirectional photonic band gap in polymer photonic crystal slabs,” *Applied Physics Letters*, vol. 91, no. 22, p. 221104, 2007.
- [75] J. Witzens, M. Lončar, and A. Scherer, “Self-collimation in planar photonic crystals,” *Selected Topics in Quantum Electronics, IEEE Journal of*, vol. 8, no. 6, pp. 1246–1257, 2002.
- [76] J. Hu and C. R. Menyuk, “Understanding leaky modes: slab waveguide revisited,” *Advances in Optics and Photonics*, vol. 1, no. 1, pp. 58–106, 2009.
- [77] A. Y. Petrov and M. Eich, “Zero dispersion at small group velocities in photonic crystal waveguides,” *Applied Physics Letters*, vol. 85, no. 21, pp. 4866–4868, 2004.
- [78] Y. Tanaka, T. Asano, R. Hatsuta, and S. Noda, “Investigation of point-defect cavity formed in two-dimensional photonic crystal slab with one-sided dielectric cladding,” *Applied physics letters*, vol. 88, no. 1, p. 011112, 2006.
- [79] S. Bong-Shik, S. Noda, T. Asano, and Y. Akahane, “Ultra-high-Q photonic double-heterostructure nanocavity,” *Nature Materials*, vol. 4, pp. 207–210, 2005.
- [80] Y. Taguchi, Y. Takahashi, Y. Sato, T. Asano, and S. Noda, “Statistical studies of photonic heterostructure nanocavities with an average Q factor of three million,” *Optics Express*, vol. 19, no. 12, pp. 11916–11921, 2011.
- [81] T. Weiland, “A discretization model for the solution of Maxwell’s equations for six-component fields,” *Archiv Elektronik und Uebertragungstechnik*, vol. 31, pp. 116–120, 1977.



- [82] R. Schuhmann and T. Weiland, “A stable interpolation technique for FDTD on non-orthogonal grids,” *International Journal of Numerical Modelling: Electronic Networks, Devices and Fields*, vol. 11, no. 6, pp. 299–306, 1998.
- [83] M. Weiland, “Discrete electromagnetism with the finite integration technique,” *Progress In Electromagnetics Research*, vol. 32, pp. 65–87, 2001.
- [84] M. Weiland, “RF & microwave simulators-from component to system design,” *Proceedings of the European Microwave Conference 2003*, vol. 33, pp. 591–596, 2003.
- [85] A. Yariv, “Critical coupling and its control in optical waveguide-ring resonator systems,” *IEEE Photonics Technology Letters*, vol. 14, no. 4, pp. 483–485, 2002.
- [86] M. Krause, “Finite-difference mode solver for curved waveguides with angled and curved dielectric interfaces,” *Journal of Lightwave Technology*, vol. 29, no. 5, pp. 691–699, 2011.
- [87] W. C. Chew, J. M. Jin, and E. Michielssen, “Complex coordinate stretching as a generalized absorbing boundary condition,” *Microwave and Optical Technology Letters*, vol. 15, no. 6, pp. 363–369, 1997.
- [88] S. Prorok, A. Y. Petrov, M. Eich, J. Luo, and A. K.-Y. Jen, “Trimming of high-Q-factor silicon ring resonators by electron beam bleaching,” *Optics Letters*, vol. 37, no. 15, pp. 3114–3116, 2012.
- [89] F. Xia, M. Rooks, L. Sekaric, and Y. Vlasov, “Ultra-compact high order ring resonator filters using submicron silicon photonic wires for on-chip optical interconnects,” *Optics Express*, vol. 15, no. 19, pp. 11934–11941, 2007.
- [90] S. Manipatruni, L. Chen, and M. Lipson, “Ultra high bandwidth WDM using silicon microring modulators,” *Optics Express*, vol. 18, no. 16, pp. 16858–16867, 2010.



- [91] H. Rong, A. Liu, R. Jones, O. Cohen, D. Hak, R. Nicolaescu, A. Fang, and M. Paniccia, “An all-silicon raman laser,” *Nature*, vol. 433, no. 7023, pp. 292–294, 2005.
- [92] W. A. Zortman, D. C. Trotter, and M. R. Watts, “Silicon photonics manufacturing,” *Optics Express*, vol. 18, no. 23, pp. 23598–23607, 2010.
- [93] B. Eggleton, G. Lenz, N. Litchinitser, D. Patterson, and R. Slusher, “Implications of fiber grating dispersion for WDM communication systems,” *Photonics Technology Letters, IEEE*, vol. 9, no. 10, pp. 1403–1405, 1997.
- [94] M. S. Nawrocka, T. Liu, X. Wang, and R. R. Panepucci, “Tunable silicon microring resonator with wide free spectral range,” *Applied Physics Letters*, vol. 89, no. 7, p. 71110, 2006.
- [95] A. Canciamilla, S. Grillanda, F. Morichetti, C. Ferrari, J. Hu, J. D. Musgraves, K. Richardson, A. Agarwal, L. C. Kimerling, and A. Melloni, “Photo-induced trimming of coupled ring-resonator filters and delay lines in  $\text{As}_2\text{S}_3$  chalcogenide glass,” *Optics Letters*, vol. 36, no. 20, pp. 4002–4004, 2011.
- [96] D. K. Sparacin, C. Yin Hong, L. C. Kimerling, J. Michel, J. P. Lock, and K. K. Gleason, “Trimming of microring resonators by photo-oxidation of a plasma-polymerized organosilane cladding material,” *Optics Letters*, vol. 30, no. 17, pp. 2251–2253, 2005.
- [97] M. Schmidt, G. Boettger, C. Liguda, M. Eich, W. Morgenroth, U. Huebner, and H. G. Meyer, “UV-trimming of two-dimensional photonic crystal structures,” *Journal of Nonlinear Optical Physics and Materials*, vol. 13, pp. 535–540, 2004.
- [98] H. Sun, A. Chen, B. C. Olbricht, J. A. Davies, P. A. Sullivan, Y. Liao, and L. R. Dalton, “Direct electron beam writing of electro-optic polymer microring resonators,” *Optics Express*, vol. 16, no. 9, pp. 6592–6599, 2008.



- [99] C. Grillet, C. Monat, C. Smith, M. Lee, S. Tomljenovic-Hanic, C. Karnutsch, and B. Eggleton, “Reconfigurable photonic crystal circuits,” *Laser and Photonics Reviews*, vol. 4, no. 2, pp. 192–204, 2010.
- [100] J. Vydra, H. Beisinghoff, T. Tschudi, and M. Eich, “Photodecay mechanisms in side chain nonlinear optical polymethacrylates,” *Applied Physics Letters*, vol. 69, no. 8, pp. 1035–1037, 1996.
- [101] J. Hampe, J. H. Wülbern, S. Prorok, A. Y. Petrov, and M. Eich, “Hybrid silicon-organic racetrack resonator designs for electro-optical modulation,” *Silicon Photonics and Photonic Integrated Circuits II*, vol. 7719, no. 11, pp. 1–10, 2010.
- [102] M. Gould, T. Baehr-Jones, R. Ding, S. Huang, J. Luo, A. K.-Y. Jen, J.-M. Fedeli, M. Fournier, and M. Hochberg, “Silicon-polymer hybrid slot waveguide ring-resonator modulator,” *Optics Express*, vol. 19, no. 5, pp. 3952–3961, 2011.
- [103] S. Prorok, A. Petrov, M. Eich, J. Luo, and A. K.-Y. Jen, “Configurable silicon photonic crystal waveguides,” *Applied Physics Letters*, vol. 103, no. 26, pp. 1–4, 2013.
- [104] Y. Eo, W. Eisenstadt, J. Y. Jeong, and O.-K. Kwon, “A new on-chip interconnect crosstalk model and experimental verification for CMOS VLSI circuit design,” *Electron Devices, IEEE Transactions on*, vol. 47, pp. 129–140, Jan 2000.
- [105] M. Asghari and A. V. Krishnamoorthy, “Silicon photonics: Energy-efficient communication,” *Nature Photonics*, vol. 5, no. 5, pp. 268–270, 2011.
- [106] A. Shinya, S. Mitsugi, E. Kuramochi, and M. Notomi, “Ultrasmall multi-channel resonant-tunneling filter using mode gap of width-tuned photonic-crystal waveguide,” *Optics Express*, vol. 13, no. 11, pp. 4202–4209, 2005.

- [107] J. Olmos, M. Tokushima, and K. Kitayama, “Photonic add-drop filter based on integrated photonic crystal structures,” *Selected Topics in Quantum Electronics, IEEE Journal of*, vol. 16, no. 1, pp. 332–337, 2010.
- [108] A. Faraon, D. Englund, D. Bulla, B. Luther-Davies, B. Eggleton, N. Stoltz, P. Petroff, and J. Vučković, “Local tuning of photonic crystal cavities using chalcogenide glasses,” *Applied Physics Letters*, vol. 92, no. 4, p. 043123, 2008.
- [109] U. Bog, C. L. C. Smith, M. W. Lee, S. Tomljenovic-Hanic, C. Grillet, C. Monat, L. O’Faolain, C. Karnutsch, T. F. Krauss, R. C. McPhedran, and B. J. Eggleton, “High-Q microfluidic cavities in silicon-based two-dimensional photonic crystal structures,” *Optics Letters*, vol. 33, no. 19, pp. 2206–2208, 2008.
- [110] T. Cai, R. Bose, G. S. Solomon, and E. Waks, “Controlled coupling of photonic crystal cavities using photochromic tuning,” *Applied Physics Letters*, vol. 102, no. 14, p. 141118, 2013.
- [111] C. Schomburg, M. Wark, Y. Rohlfig, G. Schulz-Ekloff, and D. Wöhrle, “Photochromism of spiropyran in molecular sieve voids: effects of host-guest interaction on isomer status, switching stability and reversibility,” *Journal of Materials Chemistry*, vol. 11, pp. 2014–2021, 2001.
- [112] T. Fujiwara, T. Toki, D. Tanaka, J. Kosugi, T. Susa, N. Sakasai, and A. Tokui, “Advanced CDU improvement for 22 nm and below,” *SPIE Proceedings*, vol. 7973, p. 797310, 2011.
- [113] M. W. Lee, C. Grillet, S. Tomljenovic-Hanic, E. C. Mägi, D. J. Moss, B. J. Eggleton, X. Gai, S. Madden, D.-Y. Choi, D. A. P. Bulla, and B. Luther-Davies, “Photowritten high-Q cavities in two-dimensional chalcogenide glass photonic crystals,” *Optics Letters*, vol. 34, no. 23, pp. 3671–3673, 2009.
- [114] M. Rattier, H. Benisty, C. J. M. Smith, A. Bernaud, D. Cassagne, C. Jouanin, T. Krauss, and C. Weisbuch, “Performance of waveguide-based two-dimensional photonic-crystal mirrors studied with Fabry-Perot



- resonators,” *Quantum Electronics, IEEE Journal of*, vol. 37, no. 2, pp. 237–243, 2001.
- [115] G.-H. Kim, Y.-H. Lee, A. Shinya, and M. Notomi, “Coupling of small, low-loss hexapole mode with photonic crystal slab waveguide mode,” *Optics Express*, vol. 12, no. 26, pp. 6624–6631, 2004.
- [116] M. Notomi, E. Kuramochi, and T. Tanabe, “Large-scale arrays of ultrahigh-Q coupled nanocavities,” *Nature Photonics*, vol. 2, no. 12, pp. 741–747, 2008.
- [117] S. Vignolini, F. Riboli, F. Intonti, D. Wiersma, L. Balet, L. Li, M. Francardi, A. Gerardino, A. Fiore, and M. Gurioli, “Mode hybridization in photonic crystal molecules,” *Applied Physics Letters*, vol. 97, no. 6, pp. 063101–063101–3, 2010.
- [118] S. Prorok, J. H. Wülbern, A. Y. Petrov, M. Eich, J. Luo, and A. K. Jen, “Photonic crystal cavity definition by electron beam bleaching of chromophore doped polymer cladding,” in *SPIE Photonics Europe*, pp. 842518–842518, International Society for Optics and Photonics, 2012.
- [119] J. H. Wülbern, A. Petrov, and M. Eich, “Electro-optical modulator in a polymerinfiltrated silicon slotted photonic crystal waveguide heterostructure resonator,” *Optics Express*, vol. 17, no. 1, pp. 304–313, 2009.
- [120] M. Qiu, “Band gap effects in asymmetric photonic crystal slabs,” *Physical Review B*, vol. 66, p. 033103, 2002.
- [121] J. M. Bustillo, G. K. Fedder, C. T.-C. Nguyen, and R. T. Howe, “Process technology for the modular integration of cmos and polysilicon microstructures,” *Microsystem Technologies*, vol. 1, no. 1, pp. 30–41, 1994.
- [122] P. Pal, K. Sato, M. A. Gosalvez, and M. Shikida, “Study of rounded concave and sharp edge convex corners undercutting in CMOS compatible anisotropic etchants,” *Journal of Micromechanics and Microengineering*, vol. 17, no. 11, p. 2299, 2007.



- [123] Y. Akahane, T. Asano, B.-S. Dong, and S. Noda, “High-Q photonic nanocavity in a two-dimensional photonic crystal,” *Nature*, vol. 425, no. 6961, pp. 944–947, 2005.
- [124] Z. Han, X. Checoury, L.-D. Haret, and P. Boucaud, “High quality factor in a two-dimensional photonic crystal cavity on silicon-on-insulator,” *Optics Letters*, vol. 36, no. 10, pp. 1749–1751, 2011.
- [125] D. Englund, I. Fushman, and J. Vučković, “General recipe for designing photonic crystal cavities,” *Optics Express*, vol. 13, no. 16, pp. 5961–5975, 2005.
- [126] M. W. Pruessner, T. H. Stievater, and W. S. Rabinovich, “Integrated waveguide Fabry-Perot microcavities with silicon/air bragg mirrors,” *Optics Letters*, vol. 32, no. 5, pp. 533–535, 2007.
- [127] P. Lalanne and J.-P. Hugonin, “Bloch-wave engineering for high-Q, small-V microcavities,” *Quantum Electronics, IEEE Journal of*, vol. 39, no. 11, pp. 1430–1438, 2003.
- [128] T. Baehr-Jones, M. Hochberg, C. Walker, and A. Scherer, “High-Q optical resonators in silicon-on-insulator-based slot waveguides,” *Applied Physics Letters*, vol. 86, no. 8, pp. 081101–081101–3, 2005.
- [129] P. Yeh, *Optical Waves in Layered Media*. John Wiley and Sons, 1988.
- [130] N. Ahuja, S. Lertrattanapanich, and N. Bose, “Properties determining choice of mother wavelet,” *Vision, Image and Signal Processing, IEEE Proceedings of*, vol. 152, no. 5, pp. 659–664, 2005.
- [131] J. Lu and J. Vučković, “Inverse design of nanophotonic structures using complementary convex optimization,” in *Conference on Lasers and Electro-Optics 2010*, p. CWB6, Optical Society of America, 2010.
- [132] J. Lu and J. Vučković, “Nanophotonic computational design,” *Optics Express*, vol. 21, no. 11, pp. 13351–13367, 2013.



- [133] M. Eichenfield, J. Chan, A. H. Safavi-Naeini, K. J. Vahala, and O. Painter, “Modeling dispersive coupling and losses of localized optical and mechanical modes in optomechanical crystals,” *Optics Express*, vol. 17, no. 22, pp. 20078–20098, 2009.
- [134] Q. Quan and M. Lončar, “Deterministic design of wavelength scale, ultra-high q photonic crystal nanobeam cavities,” *Optics Express*, vol. 19, no. 19, pp. 18529–18542, 2011.
- [135] B.-S. Song, S.-W. Jeon, and S. Noda, “Symmetrically glass-clad photonic crystal nanocavities with ultrahigh quality factors,” *Optics Letters*, vol. 36, no. 1, pp. 91–93, 2011.
- [136] F. Harris, “On the use of windows for harmonic analysis with the discrete fourier transform,” *Proceedings of the IEEE*, vol. 66, no. 1, pp. 51–83, 1978.
- [137] R. B. Blackman and J. W. Tukey, *The measurement of power spectra, from the point of view of communications engineering*. Dover Publications, 1958.
- [138] F. Zhang, Z. Geng, and W. Yuan, “The algorithm of interpolating windowed FFT for harmonic analysis of electric power system,” *Power Delivery, IEEE Transactions on*, vol. 16, no. 2, pp. 160–164, 2001.
- [139] H. Albrecht, “A family of cosine-sum windows for high-resolution measurements,” *Acoustics, Speech, and Signal Processing, 2001. Proceedings. IEEE International Conference on*, vol. 5, pp. 3081–3084 vol.5, 2001.
- [140] M. J. Potasek, G. P. Agrawal, and S. C. Pinault, “Analytic and numerical study of pulse broadening in nonlinear dispersive optical fibers,” *Journal of the Optical Society of America B*, vol. 3, no. 2, pp. 205–211, 1986.
- [141] H.-C. Liu and A. Yariv, “Designing coupled-resonator optical waveguides based on high-q tapered grating-defect resonators,” *Optics Express*, vol. 20, pp. 9249–9263, Apr 2012.

- [142] A. H. Nuttall, "Some windows with very good sidelobe behavior," *Acoustics, Speech and Signal Processing, IEEE Transactions on*, vol. 29, no. 1, pp. 84–91, 1981.
- [143] P. Lynch, "The Dolph-Chebyshev window: A simple optimal filter," *Acoustics, Speech and Signal Processing, IEEE Transactions on*, vol. 125, pp. 655–660, April 1997.
- [144] E. Mohajerani, A. Gilbert, and G. R. Mitchell, "Stability of NLO chromophores in doped polymer films during electric field poling," *Journal of Physics D: Applied Physics*, vol. 25, no. 9, p. 1304, 1992.
- [145] D. Derickson, *Fiber optic test and measurement*. Prentice-Hall, 1998.
- [146] S. Prorok, A. Petrov, M. Eich, J. Luo, and A. K.-Y. Jen, "Modification of a teng-man technique to measure both  $r_{33}$  and  $r_{13}$  electro-optic coefficients," *Applied Physics Letters*, vol. 105, no. 11, pp. –, 2014.
- [147] S. Prorok, M. Schulz, A. Petrov, M. Eich, J. Luo, and A. K. Jen, "Electrical and electro-optic characterization of nonlinear polymer thin films on silicon substrate," *SPIE Photonics Europe*, pp. 91371H–91371H, 2014.
- [148] S. Kim, K. Geary, H. Fetterman, C. Zhang, C. Wang, and W. H. Steier, "Photo-bleaching induced electro-optic polymer modulators with dual driving electrodes operating at  $1.55 \mu\text{m}$  wavelength," *Electronics Letters*, vol. 39, no. 18, pp. 1321–1322, 2003.
- [149] M. Sprave, R. Blum, and M. Eich, "High electric field conduction mechanisms in electrode poling of electro optic polymers," *Applied Physics Letters*, vol. 69, no. 20, pp. 2962–2964, 1996.
- [150] C. T. DeRose, Y. Enami, C. Loychik, R. Norwood, D. Mathine, M. Fallahi, N. Peyghambarian, J. Luo, A. K. Y. Jen, M. Kathaperumal, and M. Yamamoto, "Pockels coefficient enhancement of poled electro-optic polymers with a hybrid organic-inorganic sol-gel cladding layer," *Applied Physics Letters*, vol. 89, no. 13, pp. 131102–131102–3, 2006.



- [151] J. P. Drummond, S. J. Clarson, J. S. Zetts, F. K. Hopkins, and S. J. Caracci, “Enhanced electro-optic poling in guest-host systems using conductive polymer-based cladding layers,” *Applied Physics Letters*, vol. 74, no. 3, pp. 368–370, 1999.
- [152] Y. Jiang, Z. Cao, Q. Shen, X. Dou, Y. Chen, and Y. Ozaki, “Improved attenuated-total-reflection technique for measuring the electro-optic coefficients of nonlinear optical polymers,” *Journal of the Optical Society of America B*, vol. 17, no. 5, pp. 805–808, 2000.
- [153] C. Greenlee, A. Guilmo, A. Opadeyi, R. Himmelhuber, R. A. Norwood, M. Fallahi, J. Luo, S. Huang, X.-H. Zhou, A. K. Y. Jen, and N. Peyghambarian, “Mach-Zehnder interferometry method for decoupling electro-optic and piezoelectric effects in poled polymer films,” *Applied Physics Letters*, vol. 97, no. 4, pp. 041109–041109–3, 2010.
- [154] R. Norwood, M. Kuzyk, and R. A. Keosian, “Electro-optic tensor ratio determination of side-chain copolymers with electro-optic interferometry,” *Journal of Applied Physics*, vol. 75, no. 4, pp. 1869–1874, 1994.
- [155] W. Shi, Y. Ding, X. Mu, X. Yin, and C. Fang, “Electro-optic and electromechanical properties of poled polymer thin films,” *Applied Physics Letters*, vol. 79, no. 23, pp. 3749–3751, 2001.
- [156] D. H. Park and W. N. Herman, “Analysis of reflective Mach-Zehnder interferometry for electro-optic characterization of poled polymer films in multilayer structures,” *Optics Express*, vol. 20, no. 16, pp. 18254–18267, 2012.
- [157] C. Eldering, A. Knoesen, and S. T. Kowel, “Use of Fabry-Perot devices for the characterization of polymeric electro-optic films,” *Journal of Applied Physics*, vol. 69, no. 6, pp. 3676–3686, 1991.
- [158] P. Prêtre, L.-M. Wu, R. A. Hill, and A. Knoesen, “Characterization of electro-optic polymer films by use of decal-deposited reflection Fabry-Perot

- microcavities,” *Journal of the Optical Society of America B*, vol. 15, no. 1, pp. 379–392, 1998.
- [159] D. H. Park, J. Luo, A. K.-Y. Jen, and W. N. Herman, “Simplified reflection Fabry-Perot method for determination of electro-optic coefficients of poled polymer thin films,” *Polymers*, vol. 3, no. 3, pp. 1310–1324, 2011.
- [160] N. F. O’Brien, V. Dominic, and S. Caracci, “Electro-refraction and electro-absorption in poled polymer fabry-perot-etalons,” *Journal of Applied Physics*, vol. 79, no. 10, pp. 7493–7500, 1996.
- [161] D. H. Park, C. H. Lee, and W. N. Herman, “Analysis of multiple reflection effects in reflective measurements of electro-optic coefficients of poled polymers in multilayer structures,” *Optics Express*, vol. 14, no. 19, pp. 8866–8884, 2006.
- [162] E. D. Palik, *Handbook of optical constants of solids*, vol. 3. Academic press, 1998.
- [163] M. Bass, C. DeCusatis, J. Enoch, V. Lakshminarayanan, G. Li, C. MacDonald, V. Mahajan, and E. Van Stryland, *Handbook of Optics, Volume IV: Optical Properties of Materials, Nonlinear Optics, Quantum Optics*, vol. 4. McGraw Hill Professional, 2009.
- [164] R. L. Puurunen, “Surface chemistry of atomic layer deposition: A case study for the trimethylaluminum/water process,” *Journal of Applied Physics*, vol. 97, no. 12, p. 121301, 2005.
- [165] J. Luo, S. Huang, Z. Shi, B. M. Polishak, X.-H. Zhou, and A. K.-Y. Jen, “Tailored organic electro-optic materials and their hybrid systems for device applications,” *Chemistry of Materials*, vol. 23, no. 3, pp. 544–553, 2010.
- [166] J. I. Polanco, G. G. Roberts, and M. B. Myers, “AC and DC electrical conductivity in amorphous arsenic trisulphide films,” *Philosophical Magazine*, vol. 25, no. 1, pp. 117–130, 1972.



- [167] J. Edwards, K. Kawabe, G. Stevens, and R. Tredgold, “Space charge conduction and electrical behaviour of aluminium nitride single crystals,” *Solid State Communications*, vol. 3, no. 5, pp. 99 – 100, 1965.
- [168] S. Haas, A. F. Stassen, G. Schuck, K. P. Pernstich, D. J. Gundlach, B. Batlogg, U. Berens, and H.-J. Kirner, “High charge-carrier mobility and low trap density in a rubrene derivative,” *Physical Reviews B*, vol. 76, p. 115203, 2007.
- [169] W. Shockley, “The theory of p-n junctions in semiconductors and p-n junction transistors,” *Bell System Technical Journal*, vol. 28, no. 3, pp. 435–489, 1949.
- [170] H. A. Bethe, *Theory of the boundary layer of crystal rectifiers*. Radiation Laboratory, Massachusetts Institute of Technology, 1942.
- [171] W. Schottky, “Halbleitertheorie der sperrschicht,” *Naturwissenschaften*, vol. 26, no. 52, pp. 843–843, 1938.
- [172] V. Arkhipov, H. Von Seggern, and E. Emelianova, “Charge injection versus space-charge-limited current in organic light-emitting diodes,” *Applied Physics Letters*, vol. 83, no. 24, pp. 5074–5076, 2003.
- [173] G. Lengyel, “Schottky emission and conduction in some organic insulating materials,” *Journal of Applied Physics*, vol. 37, no. 2, pp. 807–810, 1966.
- [174] S. Sze, *Physics of Semiconductor devices*. John Wiley and Sons, 2 ed., 1981.
- [175] R. M. Hill, “Poole-Frenkel conduction in amorphous solids,” *Philosophical Magazine*, vol. 23, no. 181, pp. 59–86, 1971.
- [176] J. Frenkel, “On pre-breakdown phenomena in insulators and electronic semiconductors,” *Physical Reviews*, vol. 54, pp. 647–648, 1938.
- [177] J. Kolodzey, E. Chowdhury, T. Adam, G. Qui, I. Rau, J. Olowolafe, J. Suehle, and Y. Chen, “Electrical conduction and dielectric breakdown in aluminum

- oxide insulators on silicon,” *Electron Devices, IEEE Transactions on*, vol. 47, pp. 121–128, Jan 2000.
- [178] S. Santos and I. Salazar, “High electric field effect on hopping conduction in molecularly doped polymer systems,” *Polymer*, vol. 40, no. 15, pp. 4415–4418, 1999.
- [179] H. Kiess and W. Rehwald, “Electric conduction in amorphous polymers,” *Colloid and Polymer Science*, vol. 258, no. 3, pp. 241–251, 1980.
- [180] K. Mazur, “More data about dielectric and electret properties of poly(methyl methacrylate),” *Journal of Physics D: Applied Physics*, vol. 30, no. 9, p. 1383, 1997.
- [181] M. J. Sailor, F. L. Klavetter, R. H. Grubbs, and N. S. Lewis, “Electronic properties of junctions between silicon and organic conducting polymers,” *Nature*, vol. 346, no. 6280, pp. 155–157, 1990.
- [182] M. Green, F. King, and J. Shewchun, “Minority carrier MIS tunnel diodes and their application to electron- and photo-voltaic energy conversion: I. theory,” *Solid-State Electronics*, vol. 17, no. 6, pp. 551 – 561, 1974.
- [183] M. Morita, T. Ohmi, E. Hasegawa, M. Kawakami, and M. Ohwada, “Growth of native oxide on a silicon surface,” *Journal of Applied Physics*, vol. 68, no. 3, pp. 1272–1281, 1990.
- [184] S. Zheng, Q.-Q. Sun, W. Yang, P. Zhou, H.-L. Lu, and D. W. Zhang, “Modulation in current density of metal/n-SiC contact by inserting Al<sub>2</sub>O<sub>3</sub> interfacial layer,” *Nanoscale research letters*, vol. 8, no. 1, pp. 1–5, 2013.
- [185] P. J. Hotchkiss, S. C. Jones, S. A. Paniagua, A. Sharma, B. Kippelen, N. R. Armstrong, and S. R. Marder, “The modification of indium tin oxide with phosphonic acids: mechanism of binding, tuning of surface properties, and potential for use in organic electronic applications,” *Accounts of chemical research*, vol. 45, no. 3, pp. 337–346, 2011.



- [186] A. Sharma, A. Haldi, P. J. Hotchkiss, S. R. Marder, and B. Kippelen, “Effect of phosphonic acid surface modifiers on the work function of indium tin oxide and on the charge injection barrier into organic single-layer diodes,” *Journal of Applied Physics*, vol. 105, no. 7, p. 074511, 2009.
- [187] I. Costina and R. Franchy, “Band gap of amorphous and well-ordered  $\text{Al}_2\text{O}_3$  on  $\text{Ni}_3\text{Al}$  (100),” *Applied Physics Letters*, vol. 78, no. 26, pp. 4139–4141, 2001.
- [188] M. Y. Doghish and F. D. Ho, “A comprehensive analytical model for metal-insulator-semiconductor (MIS) devices,” *Electron Devices, IEEE Transactions on*, vol. 39, no. 12, pp. 2771–2780, 1992.
- [189] H. Katz, G. Scheller, T. Putvinski, M. Schilling, W. Wilson, and C. Chidsey, “Polar orientation of dyes in robust multilayers by zirconium phosphate-phosphonate interlayers,” *Science*, vol. 254, no. 5037, pp. 1485–1487, 1991.
- [190] N. Lisi, P. D. Lazzaro, and F. Flora, “Time-resolved divergence measurement of an excimer laser beam by the knife-edge technique,” *Optics Communications*, vol. 136, no. 3, pp. 247 – 252, 1997.



## List of Publications

J. H. Wülbern, S. Prorok, J. Hampe, A. Petrov, M. Eich, J. Luo, A. K.-Y. Jen, M. Jenett, and A. Jacob, "40 GHz electro-optic modulation in hybrid silicon-organic slotted photonic crystal waveguides," *Optics Letters*, vol. 35, no. 16, pp. 2753-2755, 2010.

J. Hampe, J. H. Wülbern, S. Prorok, A. Petrov, M. Eich, J. Luo, and A. K.-Y. Jen., "Hybrid silicon-organic racetrack resonator designs for electro-optical modulation," *Proc. SPIE*, vol. 7719, p. 771911, 2010.

S. Prorok, A. Petrov, M. Eich, J. Luo, and A. Jen., "Trimming of high-Q-factor silicon ring resonators by electron beam bleaching," *Optics Letters*, vol. 37, no. 15, pp. 3114–3116, 2012.

S. Prorok, J. H. Wülbern, A. Petrov, M. Eich, J. Luo, and A. K.-Y. Jen, "Photonic crystal cavity definition by electron beam bleaching of chromophore doped polymer cladding," *Proc. SPIE*, vol. 8425, p. 842518, 2012.

S. Prorok, A. Petrov, M. Eich, J. Luo, and A. K.-Y. Jen., "Configurable silicon photonic crystal waveguides," *Applied Physics Letters*, vol. 103, p. 261112, 2013.

S. Prorok, A. Petrov, M. Eich, J. Luo, and A. K.-Y. Jen., "Modification of a Teng-Man technique to measure both  $r_{33}$  and  $r_{13}$  electro-optic coefficients," *Applied Physics Letters*, vol. 105, p. 113302, 2014.

A. B. Evlyukhin, R. L. Eriksen, W. Cheng, J. Beermann, C. Reinhardt, A. Petrov, S. Prorok, M. Eich, B. N. Chichkov and S. I. Bozhevolnyi, "Optical spectroscopy of single Si nanocylinders with magnetic and electric resonances," *Scientific Reports*, vol. 4, p. 4126, 2014.



S. Prorok, M. Schulz, A. Petrov, M. Eich, J. Luo, and A. K.-Y. Jen, "Electrical and electro-optic characterization of nonlinear polymer thin films on silicon substrate," *Proc. SPIE*, vol. 9137, p. 91371H, 2014.

## Talks

S. Prorok, J. H. Wülbern, J. Hampe, A. Petrov, and M. Eich, "Broadband electro-optic modulation in silicon-organic photonic crystals," DPG Annual Meeting, Hannover, Germany, March 2010.

M. Eich, S. Prorok, J.H. Wülbern, J. Hampe, A. Petrov, M. Jenett, A. Jacob, J. Luo, A. K.-Y. Jen, "GHz-Electrooptic Modulation in Silicon-Organic Hybrid Nanophotonic Structures," IEEE Summer Topicals, Playa del Carmen, Mexico, July 2010.

M. Eich, S. Prorok, J.H. Wülbern, J. Hampe, A. Petrov, M. Jenett, A. Jacob, J. Luo, A. K.-Y. Jen, "GHz-Electrooptic Modulation in Silicon-Organic Hybrid Nanophotonic Structures," SPIE Optics+Photonics, San Diego, USA, August 2010.

S. Prorok, J. Hampe, M. Eich, "Electrooptically tunable nanophotonic structures," Tasp Workshop, Berlin, Germany, September 2011.

S. Prorok, A. Petrov, M. Eich, J. Luo, A. K.-Y. Jen, "Configurable silicon photonic crystals," Piers, Stockholm Sweden, August 2013.

S. Prorok, A. Petrov, M., J. Luo and A. K.-Y. Jen, "High Q silicon photonic crystal cavities for functional cladding materials," IEEE Photonics, Washington, USA, September 2013.



S. Prorok, A. Petrov, J. H. Wülbern, M. Eich, J. Luo and A. K.-Y. Jen, "Configurable silicon photonics with electron beam bleaching," Group IV Photonics, Seoul, Korea, September 2013.

A. Petrov, S. Prorok, M. Eich, J. Luo, A. J.-K. Jen, "Configurable Silicon Photonics by Bleaching of Polymer Cladding," Optics and Photonics Days, Turku, Finland, May 2014.



## Acknowledgements

Diese Dissertation ist das Ergebnis meiner fast fünfjährigen Forschung am Institut für Optische und Elektronische Materialien an der Technischen Universität Hamburg-Harburg. Mit Glück werden einige der hier präsentierten Ergebnisse die Grundlage für weitere Forschungsansätze bilden. Für mich persönlich jedoch stellt diese Dissertation noch etwas Anderes, viel Wichtigeres dar: Sie ist für mich Erinnerung an eine Zeit in der ich persönlich wachsen, meine Ideen verwirklichen und an meine Grenzen gehen konnte. Für diese schöne Zeit möchte ich mich hiermit bei allen beteiligten bedanken.

Mein Aufrichtiger Dank gilt Professor Manfred Eich, der mir das Vertrauen geschenkt und mich in sein Institut aufgenommen hat. Mein Respekt und meine Sympathien für ihn gehen weit über berufliche Interessen hinaus. Am meisten schätze ich bei ihm zwei Eigenschaften, die in dieser Form nur selten zusammen vorkommen: Wann immer man einen Rat braucht, ganz gleich zu welchem Thema wird man von Manfred Eich eine informierte Auskunft bekommen, nicht selten mit Literaturverweisen zu einschlägigen Publikationen. Aber er weiß auch, wann kein Rat vonnöten ist. Eine Eigenschaft, die ich ihm kaum hoch genug anrechnen kann.

Neben Professor Eich möchte auch den anderen Mitarbeitern des Instituts danken: Frau Gabriele Birjukov für ihre tatkräftige Unterstützung im Sekretariat, Frau Iris Bucher für ihre Hilfe bei Licht- und Elektronenmikroskopie, Herrn Professor Bauhofer für Parkinsons Gesetz, Herrn Stefan Schön für sein gutes Händchen mit der Leybold, Dr. Alexander Petrov für sein berühmtes *Nein* zur rechten Zeit und Herrn Michael Seiler für ungezählte Fachgespräche in Elektronikfragen.

Mein Dank gilt ferner meinen Kollegen Dr. Jan Hendrik Wülbern, Jan Hampe, Dr. Hooi Sing Lee, Dr. Michel Castellanos, Dr. Zied Fahem, Dr. Carolin Heintz, Dr. Wenjing Lee, Dr. Ali Erdem Eken, Sebastian Jakobs, Dirk Jalas, Dr. Robert Zierold, Matthias Mecklenburg, Timo Lipka, Simone Fohrmann, Slawa Lang, Dr. Pavel Dyachenko und Marvin Schulz für die gute Arbeitsatmosphäre, Hilfe bei Experimenten und so manchen guten Rat. Ein besonderer Dank gilt meinem



langjährigen Bürokollegen Dr. Ricardo Starbird für Einblicke in die Chemie die Einführung von Reinraumparties. Ich möchte mich ebenso bei meinen Studenten Faiz Ben Arabia, Somasundharam Muthumanickam, Ole Borzek, Johannes Hienen und Abdul Wahab Khan bedanken, die mir viel Arbeit abgenommen und ihren Teil zu dieser Arbeit beigesteuert haben.

Ich möchte mich an dieser Stelle auch bei meinen Eltern bedanken, für ihre Unterstützung, für ihre Zuversicht und für all das, was sie mir mit auf den Weg gaben und immer noch geben. Ich kann mir nicht vorstellen, dass ich es ohne sie so weit geschafft hätte. Der größte Dank gilt meiner Frau Cecilia für ihre Liebe, ihre Geduld und ihr Verständnis. Sie ist das Geschenk meines Lebens.



## Curriculum Vitae

Name	Stefan Prorok
Date of birth	18.08.1983
Place of birth	Hamburg (Germany)
Nationality	German

## Education

09/2011	INNOTECH Summer School for start-up entrepreneurs
10/2003–10/2009	Studies of Electrical Engineering at Hamburg University of Technology
01/2008–06/2008	Exchange semester at the University of Linköping, Sweden
07/1994–07/2003	High school diploma at Luisengymnasium Hamburg

## Professional experience

11/2009–02/2014	PhD student at Hamburg University of Technology
03/2007–07/2007	Programming instructor for the Office for Special Capability (Beratungsstelle für besondere Begabung, City of Hamburg)
01/2006–03/2007	Assistant for maintenance of IT infrastructure at the regional computing center at Hamburg University





